Periodic orbits in systems with backlash: Stability, classification & observability

Bart Besselink
Miami University

MIAMI UNIVERSITY

DEPARTMENT OF Mechanical & Manufacturing Engineering

TECHNICAL REPORT: MU-SEAS-MME-2007-001

Periodic orbits in systems with backlash: Stability, classification & observability

BART BESSELINK

ADVISOR: AMIT SHUKLA

School of Engineering & Applied Science

School of Engineering & Applied Science | Oxford, Ohio 45056 | 513-529-5928

Periodic orbits in systems with backlash: stability, classification & observability

Bart Besselink

DCT 2007.006

Traineeship report

Coach: A. Shukla

Supervisor: H. Nijmeijer

Technische Universiteit Eindhoven
Department of Mechanical Engineering
Dynamics and Control Group

Eindhoven, January 2007

This report is the result of my traineeship at Miami University in Oxford, Ohio.
August 31 – December 15, 2006

MIAMI UNIVERSITY
OXFORD OHIO

Contents

Summary

Backlash, clearance or dead zone is a common feature of many mechanical systems and can undermine the performance of the system, since it has a large influence on the dynamics and control of systems. It can be caused by intended clearance necessary for assembly and operation, but may also be the result of operational wear and tear. Systems with backlash form a subclass of discontinuous mechanical systems and can be modeled as piecewise linear systems. In this work, both stiffness and damping are modeled with piecewise characteristics.

A single and multiple degree-of-freedom model with backlash are analyzed for their harmonic periodic orbits as a function of excitation frequency and amplitude. The systems are modeled as tri-linear systems, with no stiffness in the backlash gap. This leads to a rigid body motion in this region. To calculate the flow of the piecewise linear systems, a simulation method is used that utilizes the knowledge of the analytical solutions for linear systems. This method also allows for analytical calculation of the fundamental solution matrix. This is beneficial for applying this simulation method in the multiple shooting method, which is used to calculate the periodic orbits.

First, both the single and multiple degree-of-freedom system are characterized by their response diagram for a fixed excitation amplitude. Here, the amplitude of both stable and unstable periodic orbits are calculated. The response diagram shows a combination of branches that is characteristic for a hardening oscillator, with multiple solutions in some frequency ranges.

The periodic orbits are characterized by their number of subspace boundary crossings in excitation frequency and amplitude plane. Next to the number of boundary crossings, the periodic orbits are characterized by the maximum absolute value of the Floquet multipliers. The Floquet multipliers jump when the number of subspace boundary crossings changes, so this characterization gives the same information. However, the classification by Floquet multipliers also distinguishes symmetric and asymmetric periodic orbits and therefore gives more information. These conclusions hold for both systems.

When a system with backlash is used in practice, often only the output is measured. Information on the other states, especially the backlash gap, may however be relevant for analysis and control. Therefore, an observer is designed for the multiple degree-of-freedom system. Simulations of the observer show that it converges to an error much smaller as was expected. Yet, the convergence rate is low. Further research is needed to analyze the discrepancy between theory and simulations and to increase the performance of the observer.

Samenvatting

Speling komt veel voor in mechanische systemen. Het heeft een grote invloed op de dynamica en regeltechniek van het systeem en vermindert de prestaties. Speling kan het gevolg zijn van marges die nodig zijn voor fabricage of gebruik, maar ook van slijtage. Systemen met speling vormen een deelgebied van discontinue mechanische systemen en kunnen worden gemodelleerd als stuksgewijs lineaire systemen. In dit verslag zijn zowel stijfheid als demping gemodelleerd met stuksgewijs lineaire eigenschappen.

De periodieke oplossingen van een systeem met één graad van vrijheid en een systeem met meerdere vrijheidsgraden worden geanalyseerd als functie van excitatiefrequentie en -amplitude. Deze systemen zijn gemodelleerd als stuksgewijs lineaire systemen in drie gebieden, waarbij er geen stijfheid is in het middelste gebied dat de speling representeert. Er is hierdoor een rigid body mode mogelijk in dit gebied. Om de oplossingen van het systeem te berekenen is gebruik gemaakt van een methode die is gebaseerd op de analytische oplossingen van een lineair systeem. Deze maakt het mogelijk de fundamental solution matrix analytisch te berekenen. Dit is een voordeel wanneer deze simulatiemethode wordt geïmplementeerd in de multiple shooting methode, die is gebruikt voor het berekenen van de periodieke oplossingen.

Voor beide systemen is het response diagram voor een vaste excitatieamplitude berekend. Hierin zijn zowel stabiele als instabiele periodieke banen verwerkt. Uit het response diagram blijkt dat beide systemen gedrag vertonen dat karakteristiek is voor een hardening oscillator.

De periodieke oplossingen zijn gekarakteriseerd door het aantal keer dat ze van deelgebied veranderen als functie van excitatiefrequentie en -amplitude. Naast het aantal veranderingen van deelgebied is de Floquet multiplier met de grootste absolute waarde geanalyseerd. Deze Floquet multiplier verandert plotseling wanneer de periodieke oplossing meer of minder gebieden bezoekt en geeft dus dezelfde classificatie. Daarnaast kunnen door middel van de Floquet multipliers ook symmetrische en asymmetrische periodieke oplossingen van elkaar onderscheiden worden. Dit geldt voor beide systemen.

Wanneer systemen met speling in de praktijk worden toegepast, wordt vaak alleen de uitgang gemeten. Informatie over de andere toestanden kan echter ook van belang zijn om het systeem te analyseren of regelen, waarbij vooral de speling belangrijk is. Er is daarom voor het systeem met meerdere vrijheidsgraden een observer gemaakt. Simulaties van deze observer laten zien dat de error veel kleiner is dan verwacht. De snelheid waarmee de observer convergeert is echter laag. Er is daarom meer werk nodig om het verschil tussen theorie en simulaties te analyseren en de prestaties te verbeteren.

Chapter 1

Introduction

1.1 Motivation

Backlash, dead zone or clearance is a common feature of many mechanical systems and can undermine the performance of the system. It can be caused by intended clearance necessary for assembly and operation, but may also be the result of operational wear and tear. Backlash has a large influence on the dynamics and control of systems as power transmissions, robotics and measurement systems. For instance, it can lead to rattle and chaotic motion in gear systems which causes damage and noise. Systems with backlash form a subclass of discontinuous mechanical systems and can be modeled as piecewise linear systems. Here, the stiffness has piecewise characteristics. In this work, the damping is also modeled with piecewise characteristics, which leads to a discontinuous system.

1.2 Literature review

The effect of backlash on dynamics has been investigated in literature. Next to backlash, bi-linear systems are studied as well. For instance, a bi-linear model is used to study the dynamics of compliant off-shore structures for subharmonic resonances and chaos [15]. The long term response of models with bi-linear stiffness and damping is studied for the existence and stability of boundary crossing periodic orbits in [11], which also investigates the phenomena that characterize the response. The most general n-periodic solutions and their stability are also studied for tri-linear systems with harmonic forcing [12]. Chaos in these systems is also analyzed experimentally, where the result are compared to theoretical solutions [16].

Gear systems form a subclass of systems with backlash and can be modeled as a tri-linear system with time-varying stiffness and damping. The effect of shaft stiffness is numerically studied for changing stiffness as well [10]. Similar systems without additional shaft are analyzed by using the harmonic balance method. This method is used to study the steady state forced response analytically for commensurate parametric and external forcing [1]. The same paper also uses experimental results to show the existence of subharmonic resonances. The harmonic balance method is adapted and used to study the sub- and super-harmonic responses, which are compared with experimental data [7]. Chaotic vibration for various non-linear stiffness characteristics in gear systems with backlash is numerically studied in [14].

Next to gear systems, the dynamics of an elastic beam that moves between stops is also a topic of research. Numerical methods are compared for a elastic beam which is clamped at one end and is limited in deflection on the other end in [4]. The dynamics of a piecewise linear beam is influenced by adding a dynamic vibration absorber to suppress the first harmonic resonance in [2].

A different approach to systems with backlash is to consider impact. The basic properties of an oscillator in a clearance with impact are analyzed using approximate analytic methods [5]. Next, chaotic motion of an intermittency type of the impact oscillator is considered in [13].

1.3 Objective

The objectives of this work are twofold. First, an overview of the different qualitative features of periodic orbits in systems with backlash will be created. This includes a classification of the periodic orbits by their number of subspace boundary crossings and corresponding Floquet multipliers, which gives new insights in the qualitative dynamics for systems with infinite stiffness ratio between the stopper stiffness and the stiffness in the backlash region. This classification will be done for a simple single degree-of-freedom model and a more realistic multiple degree-of-freedom model.

The second objective relates to the multiple degree-of-freedom model, for which an observer will be designed and tested by simulations. Hereto, the procedure as described in [6] is used and slightly extended.

1.4 Outline

The report is organized as follows. First, both a single and multiple degree-of-freedom system with backlash are presented in chapter 2. These systems are analyzed for their periodic responses, for which the analysis methodology is discussed in chapter 3. To calculate the flow of the piecewise linear systems, a simulation method based on analytical solutions is used. This method and its integration in the multiple shooting method are also presented in this chapter. The results of this analysis are presented in chapter 4. Next, the design of an observer is discussed in chapter 5. Finally, some conclusions and recommendations for further research are presented in chapter 6.

Chapter 2

Modeling of the system dynamics

Two systems with backlash are introduced in this chapter: a single degree-of-freedom (SDOF) and multiple degree-of-freedom (MDOF) system. Both systems will be analyzed for their periodic orbits. First, the single degree-of-freedom model will be introduced. Next, the multiple degree-of-freedom model is discussed.

2.1 Single degree-of-freedom model

The single degree-of-freedom (SDOF) system with backlash is presented schematically in figure 2.1 and consists of a mass which can move freely between two stoppers. The dynamics of the stoppers is assumed to be fast enough to ensure that they return to their original position between successive contacts and are therefore at rest when a contact occurs. This assumption is only valid when the damping force is small in comparison to the spring force. This holds for the system under consideration, so the dynamics of the stoppers does not have to be modeled and the equation of motion is given as:

$$m\ddot{x} + C(\dot{x}) + K(x) = F \tag{2.1}$$

$$\dot{\mathbf{x}} = \mathbf{f}(t, \mathbf{x}) \tag{2.2}$$

In (2.1), which can be rewritten to the standard form of (2.2), m is the mass of the system, F denotes the forcing. The nominal system parameters are shown in table 2.1. The restoring force $K(x)$ and the damping force $C(\dot{x})$ are dependent on the position of the mass. Using the state

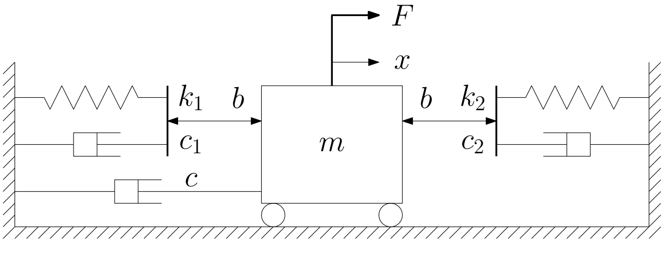

Figure 2.1: Single degree-of-freedom system with backlash

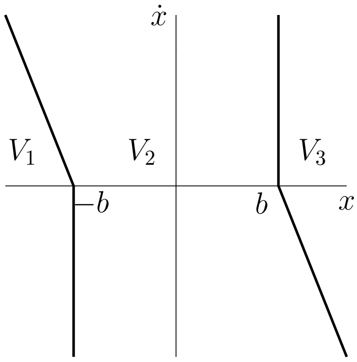

Figure 2.2: Subspaces of the SDOF system with backlash in figure 2.1

Table 2.1: Nominal parameters for the SDOF system

Parameter	Value	
m	1	kg
c	0.05	Ns/m
b	1	m
$k_1,\ k_2$	4	N/m
$c_1,\ c_2$	0.5	Ns/m
A	1	N

vector $\mathbf{x} = [x,\ \dot{x}]^{\mathrm{T}}$ this dependence can be described as:

$$K(x) = \begin{cases} 0 & ,\mathbf{x} \in V_2 \\ k_1(x+b) & ,\mathbf{x} \in V_1 \\ k_2(x-b) & ,\mathbf{x} \in V_3 \end{cases} \tag{2.3}$$

$$C(\dot{x}) = \begin{cases} c\dot{x} & ,\mathbf{x} \in V_2 \\ (c+c_1)\dot{x} & ,\mathbf{x} \in V_1 \\ (c+c_2)\dot{x} & ,\mathbf{x} \in V_3 \end{cases} \tag{2.4}$$

The state space is divided into three subspaces $V_i,\ i = \{1,2,3\}$ as is depicted in figure 2.2, based on contact or no-contact with the stoppers. As can be seen in this figure, each boundary consists of two parts. When the mass moves towards a stopper ($x\dot{x} > 0$) it will hit it when $|x| = b$, which explains the vertical parts of the boundary. However, the mass does not loose contact to the stopper when $|x| = b$, but when the contact force becomes zero. Therefore the slope of the non-vertical parts are prescribed by the ratio of the spring and damper constant of the stopper. This can mathematically be described as:

$$V_1 = \left\{\mathbf{x} \in \mathbb{R}^2 \,|\, x < -b,\ k_1(x+b) + c_1\dot{x} \le 0\right\} \tag{2.5}$$

$$V_3 = \left\{\mathbf{x} \in \mathbb{R}^2 \,|\, x > b,\ k_2(x-b) + c_2\dot{x} \ge 0\right\} \tag{2.6}$$

These equations give the conditions for contact with a stopper. If the mass is in contact with the left stopper the state is in subspace V_1 whereas V_3 denotes contact with the right stopper.

When the mass is not in contact with a stopper the state is in subspace V_2. This is the backlash region where no restoring force acts on the mass, only some damping force is present.

$$V_2 = \left\{\mathbf{x} \in \mathbb{R}^2 \,|\, \mathbf{x} \notin (V_1 \cup V_3)\right\} \tag{2.7}$$

The steady state forced response or periodic orbits of these systems are of interest as it dictates the long term dynamics and possible loss of stability for rotating machines such as geared systems.

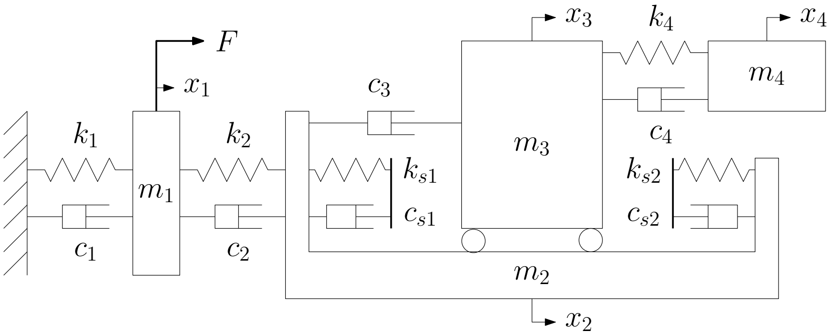

Figure 2.3: Multiple degree-of-freedom system with backlash

Often such systems operate at constant frequency where the forcing is given as:

$$F = A\sin(\omega t) \tag{2.8}$$

Using this forcing, the total equation is:

$$\dot{\mathbf{x}} = \begin{bmatrix} \dot{x} \\ -\frac{1}{m}\left(K(x) + C(\dot{x})\right) + \frac{1}{m}A\sin(\omega t) \end{bmatrix} \tag{2.9}$$

2.2 Multiple degree-of-freedom model

The multiple degree-of-freedom system (MDOF) with backlash is modeled similar to the single degree-of-freedom system and is depicted in figure 2.3. The MDOF system consists of four masses, labeled m_i. These masses are interconnected by linear springs k_i and dampers c_i. Between masses 2 and 3 however, a backlash gap (or clearance) with a width of $2b$ exists. Mass 3 can therefore freely move between the stoppers. Again, the dynamics of the stoppers is assumed to be fast enough to ensure only hits with stoppers in their original position. Therefore, the dynamics of the stoppers does not have to be modeled as is explained in section 2.1 and the equations of motion for the four masses are given by:

$$m_1\ddot{x}_1 + k_1x_1 + c_1\dot{x}_1 - k_2(x_2 - x_1) - c_2(\dot{x}_2 - \dot{x}_1) = F \tag{2.10}$$

$$m_2\ddot{x}_2 + k_2(x_2 - x_1) + c_2(\dot{x}_2 - \dot{x}_1) - K(x_2, x_3) - C(\dot{x}_2, \dot{x}_3) = 0 \tag{2.11}$$

$$m_3\ddot{x}_3 + K(x_2, x_3) + C(\dot{x}_2, \dot{x}_3) - k_4(x_4 - x_3) - c_4(\dot{x}_4 - \dot{x}_3) = 0 \tag{2.12}$$

$$m_4\ddot{x}_4 + k_4(x_4 - x_3) + c_4(\dot{x}_4 - \dot{x}_3) = 0 \tag{2.13}$$

The restoring force $K(x_2, x_3)$ and the damping force $C(\dot{x}_2, \dot{x}_3)$ between masses two and three are dependent on their relative position $x_3 - x_2$. Using the state vector
$\mathbf{x} = [x_1,\ \dot{x}_1,\ x_2,\ \dot{x}_2,\ x_3,\ \dot{x}_3,\ x_4,\ \dot{x}_4]^{\mathrm{T}}$, the forces are given by:

$$K(x_3, x_4) = \begin{cases} 0 & ,\mathbf{x} \in V_2 \\ k_{s1}(x_3 - x_2 + b) & ,\mathbf{x} \in V_1 \\ k_{s2}(x_3 - x_2 - b) & ,\mathbf{x} \in V_3 \end{cases} \tag{2.14}$$

$$C(x_3, x_4) = \begin{cases} c_3(\dot{x}_3 - \dot{x}_2) & ,\mathbf{x} \in V_2 \\ (c_3 + c_{s1})(\dot{x}_3 - \dot{x}_2) & ,\mathbf{x} \in V_1 \\ (c_3 + c_{s2})(\dot{x}_3 - \dot{x}_2) & ,\mathbf{x} \in V_3 \end{cases} \tag{2.15}$$

The restoring and damping force are dependent on the state of the system as is shown in figure 2.4. The state space is divided into three subspaces V_1, V_3 and V_2 that respectively represent contact with the left stopper, contact with the right stopper and no contact. These subspaces are equal to

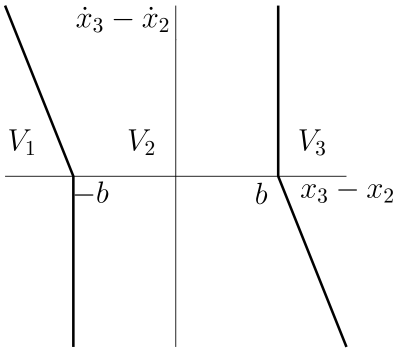

Figure 2.4: Subspaces of the MDOF system with backlash in figure 2.3

Table 2.2: Nominal parameters for the MDOF system

Parameter	Value	
$m_1,\ m_4$	0.5	kg
$m_2,\ m_3$	1	kg
$k_1,\ k_2,\ k_4$	0.2	N/m
$c_1,\ c_2,\ c_4$	0.02	Ns/m
c_3	0.05	Ns/m
$k_{s1},\ k_{s2}$	4	Ns/m
$c_{s1},\ c_{s2}$	0.05	Ns/m
b	1	m
A	1	N

those of the SDOF system in figure 2.2, only they are now dependent on the relative coordinate $x_3 - x_2$ instead of the absolute coordinate x for the SDOF system. This gives the condition for subspace V_1:

$$V_1 = \left\{\mathbf{x} \in \mathbb{R}^8 \mid x_3 - x_2 < -b,\ k_{s1}(x_3 - x_2 + b) + c_{s1}(\dot{x}_3 - \dot{x}_2) \leq 0\right\} \tag{2.16}$$

The condition for subspace V_3, which is active when there is contact with the right stopper, is similar.

$$V_3 = \left\{\mathbf{x} \in \mathbb{R}^8 \mid x_3 - x_2 > b,\ k_{s2}(x_3 - x_2 - b) + c_{s2}(\dot{x}_3 - \dot{x}_2) \geq 0\right\} \tag{2.17}$$

When there is no contact with a stopper, the system state is in subspace V_2. This is the backlash region where no restoring force acts on the masses.

$$V_2 = \left\{\mathbf{x} \in \mathbb{R}^8 \mid \mathbf{x} \notin (V_1 \cup V_3)\right\} \tag{2.18}$$

Using the periodic forcing as introduced in equation (2.8), the total system description is:

$$\dot{\mathbf{x}} = \begin{bmatrix} \dot{x}_1 \\ \frac{1}{m_1}\left(-k_1 x_1 - c_1 \dot{x}_1 + k_2(x_2 - x_1) + c_2(\dot{x}_2 - \dot{x}_1) + A\sin(\omega t)\right) \\ \dot{x}_2 \\ \frac{1}{m_2}\left(-k_2(x_2 - x_1) - c_2(\dot{x}_2 - \dot{x}_1) + K(x_2, x_3) + C(\dot{x}_2, \dot{x}_3)\right) \\ \dot{x}_3 \\ \frac{1}{m_3}\left(-K(x_2, x_3) - C(\dot{x}_2, \dot{x}_3) + k_4(x_4 - x_3) + c_4(\dot{x}_4 - \dot{x}_3)\right) \\ \dot{x}_4 \\ \frac{1}{m_4}\left(-k_4(x_4 - x_3) - c_4(\dot{x}_4 - \dot{x}_3)\right) \end{bmatrix} \tag{2.19}$$

The nominal parameters are given in table 2.2. The stopper parameters are equal to the parameters of the SDOF system to allow for comparison. The ratio of the different stiffnesses is loosely based on a gear transmission, where the stiffness of the driving shafts is in general less than the stiffness of the gears. The ratio of masses is based on a gear transmission as well.

Since the system is discontinuous, the Filippov solution concept is used. This concept is shortly described in appendix A.

Chapter 3

Analysis methodology

The methods used for analyzing the systems presented in chapter 2 will be discussed in this chapter. A review on the theory of periodic orbits and their stability is presented in appendix A. This includes monodromy matrices and Floquet multipliers. Since the systems are described by a differential equation with a discontinuous right-hand side, saltation matrices are reviewed as well.

In this chapter, a simulation method for piecewise-linear systems and its implementation in shooting methods is presented.

3.1 Simulation

The solution of the forced single degree-of-freedom and multiple degree-of-freedom system can be obtained by integrating (2.9) and (2.19) respectively. However, to obtain an accurate solutions at a change in subspace the tolerance must be low, causing a long simulation time. This simulation time can be reduced by using the knowledge of analytical solutions for linear systems. Both the SDOF and MDOF systems are piecewise linear and forced using a sine-function, so an analytical solution can be found in each subspace. Hereto, a general piecewise linear system is considered.

$$\dot{\mathbf{x}}(t) = \mathbf{A}_v(\mathbf{x}(t) - \Delta\mathbf{x}_v) + \mathbf{B}u(t) \tag{3.1}$$

Here, $\mathbf{A}_v$ denotes the system matrix in subspace v, the input matrix $\mathbf{B}$ is assumed to be equal for all subspaces. This is the case for the systems under consideration here, but the method can easily be extended for changing input matrices as well. The $\Delta\mathbf{x}_v$ term is due to the different equilibrium points for the different subspaces. Contact with the left stopper for the SDOF system is considered to explain this. The system description in this subspace (V_1) has $\mathbf{x}_e = [-b,\ 0]^{\mathrm{T}}$ as equilibrium point, because the spring is relaxed in this position. On the other hand, the system description for contact with the right stopper has $\mathbf{x}_e = [b,\ 0]^{\mathrm{T}}$ as equilibrium position. The global coordinate system is chosen to have $\mathbf{x} = \mathbf{0}$ in the middle between the stoppers, so an offset has to be introduced to describe the contact regions as standard linear equations. Therefore, the $\Delta\mathbf{x}_v$ term is introduced in (3.1). The same argument holds for the MDOF system.

The solution of (3.1) is well known:

$$\mathbf{x}(t) - \Delta\mathbf{x} = \mathbf{M}e^{\mathbf{\Lambda}t}\mathbf{M}^{-1}(\mathbf{x}_0 - \Delta\mathbf{x}) + \int\limits_0^t \mathbf{M}e^{\mathbf{\Lambda}(t-\tau)}\mathbf{M}^{-1}\mathbf{B}u(\tau)\,d\tau \tag{3.2}$$

Here, the Jordan decomposition $\mathbf{A}_v = \mathbf{M}_v\mathbf{\Lambda}_v\mathbf{M}_v^{-1}$ is used. The subscript v indicating the subspace will be omitted for ease of notation. The notation is further simplified by using $\hat{\mathbf{x}}(t) = \mathbf{x}(t) - \Delta\mathbf{x}$ and $\hat{\mathbf{B}} = \mathbf{M}^{-1}\mathbf{B}$:

$$\hat{\mathbf{x}}(t) = \mathbf{M}e^{\mathbf{\Lambda}t}\left(\mathbf{M}^{-1}\hat{\mathbf{x}}_0 + \mathbf{d}(t)\right), \quad \mathbf{d}(t) = \int\limits_0^t e^{-\mathbf{\Lambda}\tau}\hat{\mathbf{B}}u(\tau)\,d\tau \tag{3.3}$$

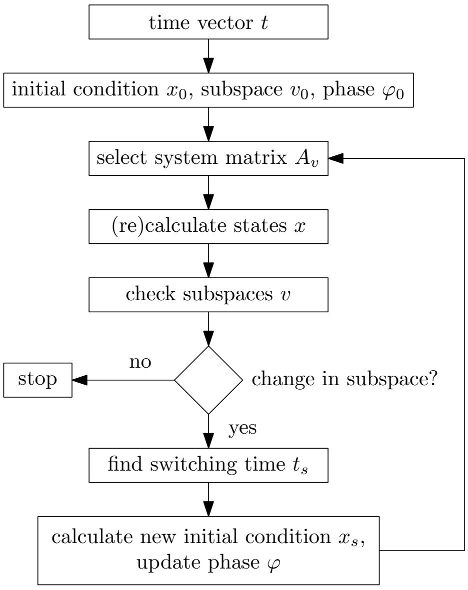

Figure 3.1: Flowchart for the simulation algorithm

It is assumed that the eigenvalues of $\mathbf{A}$ are distinct, so $e^{-\mathbf{\Lambda}\tau}$ is diagonal. This yields n decoupled equations in the integral, which can all be solved separately. The solution uses the complex notation of the periodic forcing, which is given as:

$$u(\tau) = A\sin(\omega\tau + \phi) = \frac{A}{2i}(e^{i(\omega\tau+\phi)} - e^{-i(\omega\tau+\phi)}) \tag{3.4}$$

Using this complex notation, the k-th entry in the vector $\mathbf{d}$, $\mathbf{d}_k$ is given by:

$$\mathbf{d}_k(t) = \frac{A\hat{\mathbf{B}}_k}{2i}\int_0^t e^{-(\lambda_k - i\omega)\tau}e^{i\phi} - e^{-(\lambda_k+i\omega)\tau}e^{-i\phi}\,d\tau, \quad k = 1,\ldots,n \tag{3.5}$$

Here, $\mathbf{B}_k$ is the k-th entry of vector $\mathbf{B}$, λ_k is the k-th eigenvalue. The solution of (3.5) is:

$$\mathbf{d}_k(t) = \frac{A\hat{\mathbf{B}}_k}{2i}\left(-\frac{(e^{-(\lambda_k-i\omega)t} - 1)e^{i\phi}}{\lambda_k - i\omega} + \frac{(e^{-(\lambda_k+i\omega)t} - 1)e^{-i\phi}}{\lambda_k + i\omega}\right) \tag{3.6}$$

Using this expression, equation (3.3) can now be calculated for any time t. This is used in the algorithm calculating the total solution of the piecewise linear system.

To calculate the solution of the piecewise linear system, a time vector t is created. For each instance t_k in this vector, the corresponding state $\mathbf{x}_k$ has to be calculated. Figure 3.2 shows the basics of the simulation algorithm. The flowchart for the simulation algorithm is depicted in figure 3.1

The algorithm starts by finding the subspace v_0 in which the initial condition $\mathbf{x}_0$ is located. This is done using conditions (2.5) to (2.7) for the SDOF system and conditions (2.16) to (2.18) for the MDOF system. When the initial subspace is know, the correct system description $\mathbf{A}_v$ and offset $\Delta\mathbf{x}_v$ are selected and the eigenvalue analysis is executed. This data is used in equation (3.3) to obtain the solution for all t_k in the time vector. In this calculation, the system matrices are not changed so an error is made when a different subspace is entered. This is depicted in figure 3.2, where the solid line is the result of this calculation. However, only the bold part (in the initial subspace) of this solution is correct, so the subspace boundary crossing has to be found.

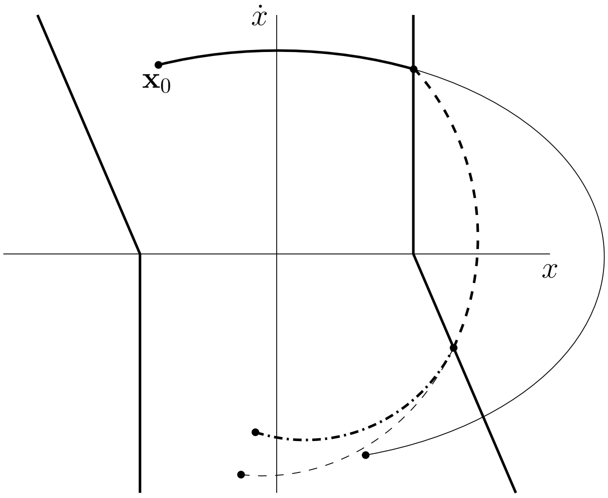

Figure 3.2: Fundamentals of the simulation method, with the final solution depicted in bold. The intermediate solutions are shown as thin lines.

The subspace boundary crossing is found by calculation the subspaces v_k for all states $\mathbf{x}_k$ at t_k. When all v_k are equal, the solution did not leave the initial subspace and the total solution is found. It is however more likely that not all v_k are equal. When v_{l+1} is the first point that differs from v_0, the change in subspace is known to occur between t_l and t_{l+1}. The switching time t_s and corresponding state $\mathbf{x}_s$ can then be found at arbitrary accuracy by calculating additional states and corresponding subspaces for $t_l < t < t_{l+1}$.

When the switching time t_s is found, an updated solution can be calculated for $k = l + 1, l + 2, \ldots$. Hereto, the new system matrices corresponding to the new subspace v_{l+1} are selected and the updated solution is calculated using $\mathbf{x}_s$ as initial condition. This global initial condition is transformed to the local initial condition using $\Delta\mathbf{x}_v$. In the update step, the solution starts at $t = 0$ again, so the phase angle ϕ of the forcing has to be modified to ensure a smooth forcing function over the entire solution. This update is given as:

$$\phi = \phi + \omega t_s \tag{3.7}$$

The updated part is schematically depicted as the dashed line in figure 3.2, where the bold part is again the correct solution. The procedure as described above is repeated to find the new subspace boundary crossing and update the incorrect part, yielding the dash-dotted part. In general, this procedure is repeated until the correct states are calculated for all time t_k.

It should be noticed that the time step, $\delta t = t_{k+1} - t_k$, has to be chosen small enough to ensure that subspaces are not crossed without calculating any data point in it. When this happens, the change in subspace will not be noticed, resulting in an incorrect solution. Since an analytical solution can be calculated for a large number of points instantaneously, choosing a sufficiently small δt does not lead to an excessive increase in calculation time.

The simulation method as described above has the advantage that it calculates the subspace boundary crossing times. This information can be used to calculate the fundamental solution matrix for any calculated orbit without the need for additional simulation. In general, n additional simulations for different initial perturbations have to be done to find the fundamental solution matrix. By using the simulation algorithm for piecewise linear system however, the fundamental solution matrix can be calculated directly. The shooting algorithm, which will be discussed in the next section, relies on this fundamental solution matrix to obtain updated estimates for the periodic orbit.

To obtain the fundamental solution matrix for a piecewise linear system, a linear system is discussed first. Therefore, the standard description in equation (3.1) is repeated for local coordinates. The fundamental solution matrix is independent on the input matrix $\mathbf{B}$, but this term is shown for completeness.

$$\dot{\hat{\mathbf{x}}}(t) = \mathbf{A}\hat{\mathbf{x}}(t) + \mathbf{B}u(t) \tag{3.8}$$

The evolution of a perturbation is given by the Jacobian ($\partial\mathbf{f}/\partial\mathbf{x}$) of the dynamics, as presented in equation (A.11). For linear systems, the Jacobian is simply the system matrix $\mathbf{A}$. The Jacobian also gives a differential equation for the fundamental solution matrix, as was shown in equation (A.13) and is repeated here. Since the Jacobian is constant and therefore independent of the initial condition on the periodic solution, this argument can be dropped.

$$\dot{\mathbf{\Phi}}(t, t_0) = \mathbf{A}\mathbf{\Phi}(t_0, t_0), \quad \mathbf{\Phi}(t_0, t_0) = \mathbf{I}_n \tag{3.9}$$

This equation is linear, so it only depends on the time span $t - t_0$. The solution of this linear differential equation is:

$$\mathbf{\Phi}(t, t_0) = e^{\mathbf{A}(t-t_0)}\mathbf{\Phi}(t_0, t_0) = e^{\mathbf{A}(t-t_0)} \tag{3.10}$$

The fundamental solution matrices in the linear subspaces can be calculated using (3.10) with the corresponding $\mathbf{A}$ matrix. The effect of a subspace boundary crossing on a perturbation is described by a saltation matrices. These saltation matrices are used to connect the linear subspaces using the transition property in (A.16) resulting in the fundamental solution matrix for the entire orbit.

To illustrate this, the orbit (the bold line) in figure 3.2 is considered. It is assumed to start at initial condition $\mathbf{x}_0$ at t_0 in subspace 2. The periodic orbit is in subspace 3 for $t_{s1} < t < t_{s2}$, where t_{si} denote the boundary crossing times. The end time is labeled T. The fundamental solution matrix for this orbit can be separated using the transition property (A.16).

$$\mathbf{\Phi}(T, t_0, \mathbf{x}_0) = \mathbf{\Phi}(T, t_{s2+})\mathbf{\Phi}(t_{s2+}, t_{s2-})\mathbf{\Phi}(t_{s2-}, t_{s1+})\mathbf{\Phi}(t_{s1+}, t_{s1-})\mathbf{\Phi}(t_{s1-}, t_0) \tag{3.11}$$

By using the definition of the saltation matrices in (A.31) and the fundamental solution matrices for linear systems in (3.10) the total fundamental solution matrix can be calculated by:

$$\mathbf{\Phi}(T, t_0, \mathbf{x}_0) = e^{\mathbf{A}_2(T-t_{s2})}\mathbf{S}_{23}e^{\mathbf{A}_3(t_{s2}-t_{s1})}\mathbf{S}_{32}e^{\mathbf{A}_2(t_{s1}-t_0)} \tag{3.12}$$

Here, $\mathbf{S}_{ij}$ denotes the saltation matrix for entering subspace i while leaving subspace j. The saltation matrices for both the SDOF and MDOF system can be found in appendix C.

3.2 Multiple shooting

Different methods are available to find periodic orbits. In this report, the (single) shooting and multiple shooting method are discussed. Both methods use the Newton-Rhapson algorithm to find a zero of a multi-dimensional function. The Newton-Rhapson algorithm and the (single) shooting method are discussed in appendix A.6.

A disadvantage of the (single) shooting method is that is uses one initial point, which makes the method vulnerable for bad initial guesses. The multiple shooting method uses a number of points along the periodic solution, which makes it more robust. These N shooting points are equally spaced in time with constant time step $h = T/N$, so $t_k = t_0 + kh$, and are stored in the vector $\mathbf{X} = [\mathbf{x}_1, \dots \mathbf{x}_k, \dots \mathbf{x}_N]^{\mathrm{T}}$. The segment connecting point $\mathbf{x}_{k-1}$ to the next point $\mathbf{x}_k$ is given by:

$$\mathbf{x}_k = \varphi_h(t_{k-1}, \mathbf{x}_{k-1}) \tag{3.13}$$

Here, $\varphi_h(t_{k-1}, \mathbf{x}_{k-1})$ denotes the solution of $\dot{\mathbf{x}}(t) = \mathbf{f}(\mathbf{x}(t), t)$ at time t_k starting at initial condition $\mathbf{x}_{k-1}$ (at t_{k-1}). This solution is evaluated using the analytical procedure described above. It can

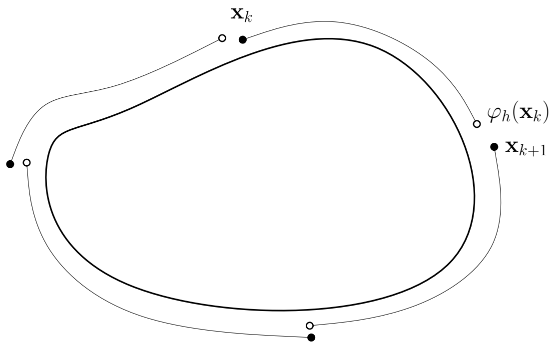

Figure 3.3: The multiple shooting method

be seen in figure 3.3 that a periodic solution is found if all segments connect, so when (3.13) holds for all segments. Therefore, a zero of the following function is to be calculated:

$$\mathbf{H}(\mathbf{X}) = \begin{bmatrix} -\mathbf{x}_1 + \varphi_h(t_N, \mathbf{x}_N) \\ \vdots \\ -\mathbf{x}_k + \varphi_h(t_{k-1}, \mathbf{x}_{k-1}) \\ \vdots \\ -\mathbf{x}_N + \varphi_h(t_{N-1}, \mathbf{x}_{N-1}) \end{bmatrix} \tag{3.14}$$

The Newton-Raphson algorithm is used iteratively to obtain an updated estimate of the periodic solution.

$$\frac{\partial \mathbf{H}}{\partial \mathbf{X}} \Delta \mathbf{X} = -\mathbf{H}(\mathbf{X}) \tag{3.15}$$

Here, the partial derivative is given by:

$$\frac{\partial \mathbf{H}}{\partial \mathbf{X}} = \begin{bmatrix} -I & 0 & \dots & 0 & \Phi_h(t_N, \mathbf{x}_N) \\ \Phi_h(t_1, \mathbf{x}_1) & -I & \dots & 0 & 0 \\ \vdots & \vdots & & \vdots & \vdots \\ 0 & 0 & \dots & \Phi_h(t_{N-1}, \mathbf{x}_{N-1}) & -I \end{bmatrix} \tag{3.16}$$

Here, $\Phi_h(t_1, \mathbf{x}_1)$ denotes the fundamental solution matrix at time $t_1 + h$ for a solution with initial condition x_1 at t_1. When the set of equations (3.15) is solved, the next iterate can be calculated:

$$\mathbf{X}^{(i+1)} = \mathbf{X}^{(i)} + \Delta \mathbf{X}^{(i)} \tag{3.17}$$

When the multiple shooting method is applied to the SDOF system with backlash in figure 2.1 (and described in (2.9)), a problem arises for periodic solutions that are entirely in the backlash gap (and do not hit the stoppers). Since the absence of a restoring force in this region, a small perturbation in the position $\delta x(t_0)$ of the mass will neither grow or decay, the entire periodic orbit will just be shifted in position. The velocity will not be affected. This knowledge gives some insight in the monodromy matrix for this situation. Therefore, the perturbation $\Delta \mathbf{x}(t_a) = [\delta x(t_a)\ 0]^{\mathrm{T}}$ is considered. The monodromy matrix maps this perturbation $\Delta \mathbf{x}(t_a)$ to $\Delta \mathbf{x}(t_a + T)$, which is equal to the initial perturbation.

$$\begin{bmatrix} \delta x(t_a + T) \\ 0 \end{bmatrix} = \Phi_T \begin{bmatrix} \delta x(t_a) \\ 0 \end{bmatrix} \tag{3.18}$$

By inspecting this equation, it can be seen that the first column of the monodromy matrix is $e_1 = [1\ 0]^{\mathrm{T}}$. This holds for all t_a. As an example, this column is substituted in (3.16) for a multiple shooting algorithm using three points ($N = 3$). Then, columns 1, 3 and 5 of $\partial\mathbf{H}/\partial\mathbf{X}$ are respectively:

$$\begin{bmatrix} -1 \\ 0 \\ 1 \\ 0 \\ 0 \\ 0 \end{bmatrix}, \quad \begin{bmatrix} 0 \\ 0 \\ -1 \\ 0 \\ 1 \\ 0 \end{bmatrix}, \quad \begin{bmatrix} 1 \\ 0 \\ 0 \\ 0 \\ -1 \\ 0 \end{bmatrix}$$

It is clear that these columns are not linearly independent, so $\partial\mathbf{H}/\partial\mathbf{X}$ will not have full rank and (3.15) can not be solved. This is a result of the rigid body motion possible in the backlash region. Thus, a rigid body constraint can be added to make the above matrix, $\partial\mathbf{H}/\partial\mathbf{X}$, full rank. This equation sums the updates in the states x off all N points and forces it to be equal to the negative mean of those states. For $N = 3$, this equation is:

$$\begin{bmatrix} 1 & 0 & 1 & 0 & 1 & 0 \end{bmatrix} \Delta\mathbf{X}^{(i)} = -\left(\mathbf{X}_1^{(i)} + \mathbf{X}_3^{(i)} + \mathbf{X}_5^{(i)}\right)/3 \tag{3.19}$$

Here, $\mathbf{X}_1$ denotes the first entry in the vector $\mathbf{X}$, which is the position coordinate of the first shooting point. Similarly, $\mathbf{X}_3$ and $\mathbf{X}_5$ denote the position coordinates of the other shooting points. This equation basically makes sure that the periodic solution is (roughly) located in the center between the two stoppers and does not influence the periodic solution itself. By adding this rigid body constraint, the total number of equations is one larger than the number of variables and thus a least squares solution can be calculated.

Since this extra equation is not needed when the periodic solution comes in contact with the stoppers, it is only used when the condition number of $\partial\mathbf{H}/\partial\mathbf{X}$ is very high. Next, it should be noticed that this problem does not exist for $N = 1$, which basically is the single shooting algorithm. A similar problem occurs for the MDOF system with backlash (figure 2.3) and the same strategy can be used to find the periodic orbits in the backlash region.

Chapter 4

Results

The methods discussed in chapter 3 are used to calculate and classify periodic orbits for both the single and multiple degree-of-freedom model. These results are presented in this chapter. First, the result for the single degree-of-freedom model are presented and discussed. Next, the results for the multiple degree-of-freedom model are presented in a similar way.

4.1 Single degree-of-freedom model

The dynamics of the singe degree-of-freedom system (figure 2.1) as described by (2.9) is characterized by the response diagram in figure 4.1. This figure shows the amplitude of the periodic solution for a range of forcing frequencies ω for nominal excitation amplitude, $A = 1$ N. Stable branches are indicated by solid lines, while unstable branches are shown in dashed lines. The branches are calculated using the multiple shooting algorithm in combination with sequential continuation as described in this paper. It is clear that multiple solutions exist near the primary peak. This combination of branches in figure 4.1 is characteristic of a hardening oscillator.

4.1.1 Periodic response

Next, some periodic orbits on the response curve in figure 4.1 are highlighted to discuss the characteristics of periodic orbits exhibited by this system. For frequencies $\omega > 1$ rad/s, for some initial conditions, the mass can move in the region between the stoppers without hitting them. Examples of such an orbit are given in figure 4.3. Since the subspace boundaries are not crossed by these periodic solutions, the dynamics are purely linear. In this subspace, no restoring force is present. The periodic orbit is therefore not unique; it can be shifted in position. This however does not affect the nature of the periodic solution and the amplitude will not change by shifting the solution. Because of the absence of a restoring force, one Floquet multiplier is equal to one, as is shown in table 4.1. The Floquet multipliers are not affected by a shift of the periodic solution in the backlash region.

Table 4.1: Floquet multipliers for the labeled periodic orbits in figure 4.1

Label	Floquet multipliers	
A	1.0000	0.7990
B	1.4210	0.1482
C	0.6086	0.3085
D	-0.2249 - 0.2261i	-0.2249 + 0.2261i
E	-0.0986 - 0.0120i	-0.0986 + 0.0120i
F	0.0001	0.0

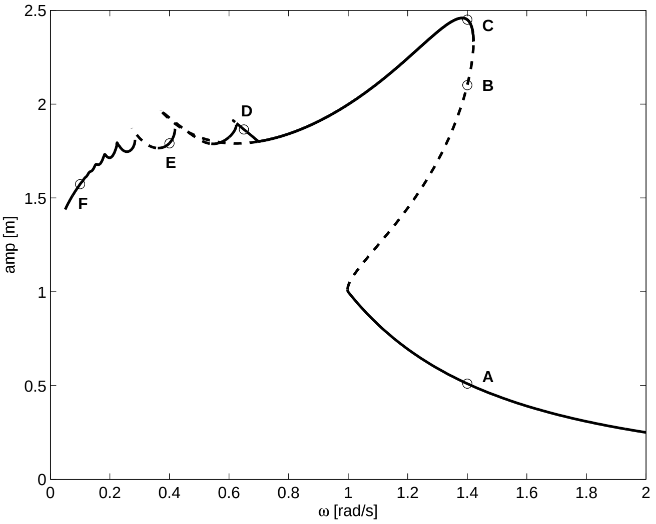

Figure 4.1: Response diagram of the SDOF system (2.9) for $A = 1$

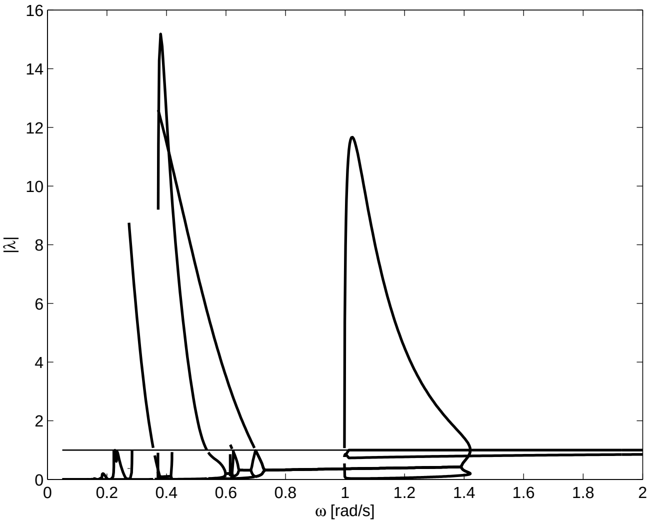

Figure 4.2: Floquet multipliers for the periodic orbits in figure 4.1

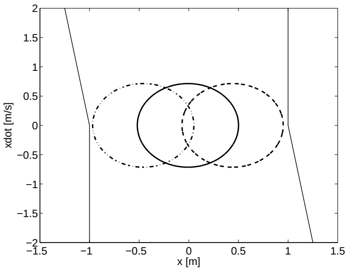

Figure 4.3: Periodic orbits at label A in figure 4.1 ($\omega = 1.4$ rad/s)

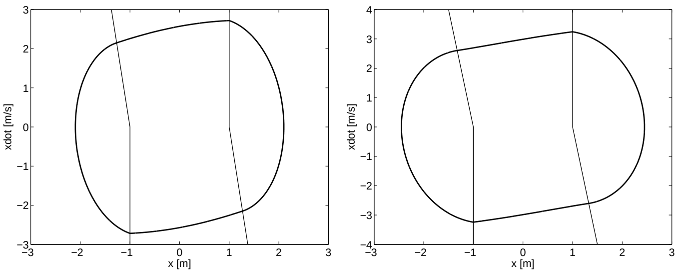

Figure 4.4: Periodic orbits at labels B (left) and C (right) in figure 4.1 ($\omega = 1.4$ rad/s)

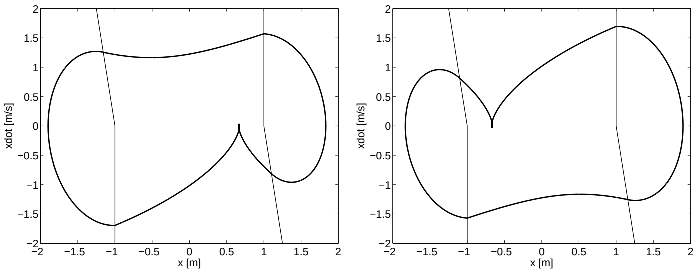

Figure 4.5: Periodic orbits at label D in figure 4.1 ($\omega = 0.65$ rad/s)

The distance between the stoppers is $2b$, so this linear solution will exist for amplitudes up to one, which is around $\omega = 1$ rad/s. However, in the frequency range of $(1,\ 1.42)$ rad/s, the backlash system has multiple solutions for the same excitation frequency, of which orbits A, B and C are an example. For $\omega = 1.4$ rad/s, the solution at C is shown in figure 4.4. In this case the stoppers are engaged and the solution visits all subspaces. The two stable branches containing A and C are connected by an unstable branch. Orbit B in figure 4.4 is an example of an unstable periodic orbit on this branch. This unstable orbit also visits all subspaces, but has a smaller amplitude than the stable solution.

When the top branch is tracked for decreasing excitation frequency, it loses stability at $\omega = 0.7$ rad/s. However, a branch of asymmetrical periodic orbits originates at the same point. The asymmetrical periodic orbit at point D is depicted in figure 4.5. Since both stoppers have the same parameters, the dynamic equations are symmetric around $[x,\ \dot{x}]^{\mathrm{T}} = \mathbf{0}$. Therefore, a mirrored version of the orbit at point D can also be found.

For decreasing excitation frequency, the number of boundary crossings increases and hence can be used to classify the periodic orbits. Figure 4.6 shows examples of multiple boundary crossings. Each time the number of boundary crossings changes a *corner collision* bifurcation [3] takes place. In corner collision bifurcations the periodic solution just touches the subspace boundary at the discontinuity in the boundary prior to crossing the boundary for some change in parameter. In this system this is exhibited in the parameter space of excitation amplitude and frequency. The response diagram may be incomplete for this low-frequency region, but the focus of this paper is on the main branch.

Figure 4.2 shows the magnitude of the Floquet multipliers corresponding to the response diagram in figure 4.1. The branch where the response amplitude is smaller than one shows a Floquet multiplier equal to one, which is caused by the absence of a restoring force. At the point where this branch crosses the boundary to become an unstable orbit a *discontinuous fold bifurcation* [9] occurs. Characteristic for this bifurcation is the jump of Floquet multipliers through the unit circle as can be observed in figure 4.1. The point at $\omega = 0.7$ rad/s where the stable symmetrical branch

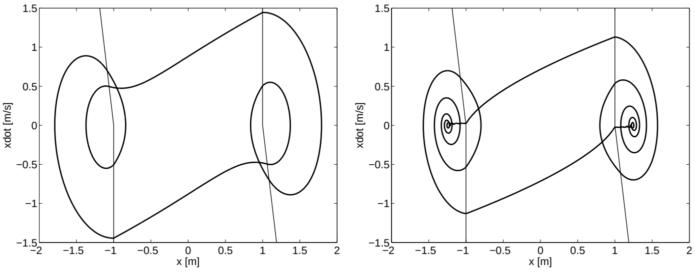

Figure 4.6: Periodic orbits at labels E (left, $\omega = 0.4$ rad/s) and F (right, $\omega = 0.1$ rad/s) in figure 4.1

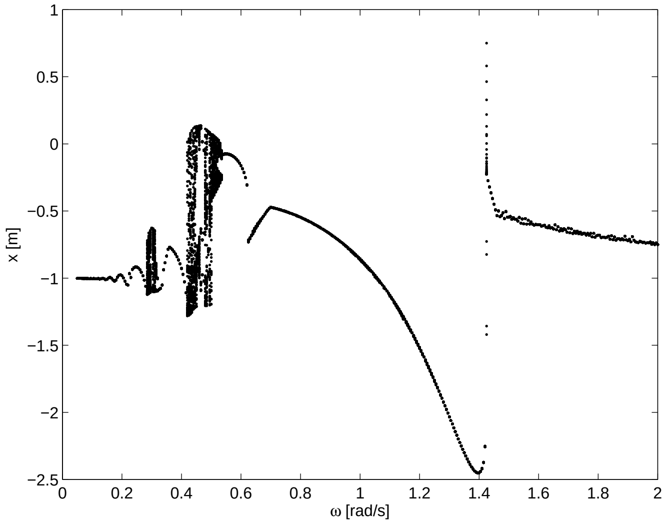

Figure 4.7: Bifurcation diagram of the SDOF system (2.9)

splits into an unstable symmetrical and stable asymmetrical branch can be clearly recognized. It has to be noted that for a range of frequencies between 0.42 and 0.54 rad/s no stable solution exists. This can also be concluded from figure 4.7, which shows a bifurcation diagram for a forcing amplitude $A = 1$ N. This figure suggests chaotic of quasi-periodic behavior in this frequency range.

4.1.2 Boundary Classification

The dynamics of the system can be characterized by counting the number of boundary crossings of a periodic orbit. A boundary crossing is counted every time the periodic solution changes subspace. This is done for different forcing frequencies and amplitudes, yielding figures 4.8 and 4.11. The periodic solutions are found by using the multiple shooting algorithm. The initial condition for the shooting algorithm is obtained via simulation so that the initial response is died out. For figure 4.8, the initial condition for the simulation is calculated using the linear system description in subspace V_2 to ensure that the solution stays in the center between the stoppers. This will result in solutions in the lower branch of figure 4.1. On the contrary, the initial condition (for the simulation) for figure 4.11 is chosen to be in a region where there is contact with a stopper, therefore increasing the probability of finding the solutions on the top branch of figure 4.1.

Based on the linear equations in subspace V_2, the dashed line, (see figures 4.8 and 4.11), where the amplitude of the periodic response is equal to one can be calculated analytically. In this case the periodic solution just touches (but does not cross) the boundary. This is referred to as a *corner*

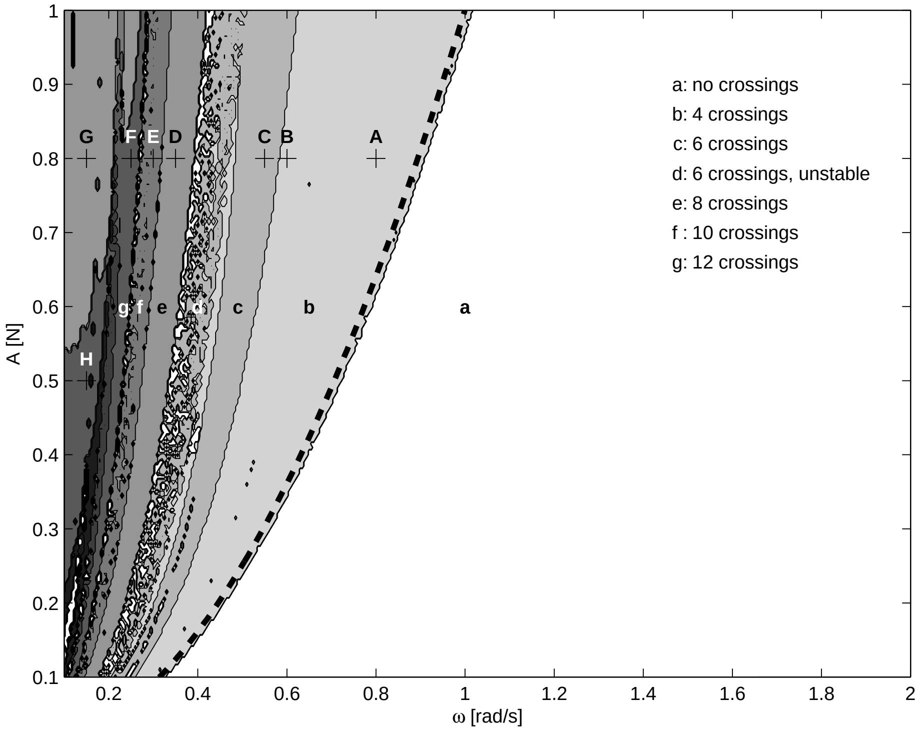

Figure 4.8: Classification of periodic orbits in $(A,\ \omega)$ space: boundary crossings

collision boundary [3].

The basic trend in figure 4.8 is that the number of crossings increases for decreasing frequency. For low frequencies, the direction of the force stays the same for a longer time span. Here, the dynamics of the system in contact with the stoppers is faster than the change in forcing direction. The graph also shows an analytically calculated boundary in a bold dashed line. Since the system description is linear in the region between the stoppers (V_2), the amplitude of the periodic response can be calculated analytically. This results in the boundary that indicates the region where the mass first hits the stoppers. The analytically calculated boundary matches the numerically calculated boundary very well. The small discrepancy is likely to be caused by the simulated solution not to be exactly in the center between the stoppers.

The non-periodic region, with excitation frequencies between 0.42 and 0.54 rad/s for $A = 1$ N, that was shown in figure 4.7 can also be observed in figure 4.8. No stable solutions exist in this region labeled d in the figure.

For all periodic orbits that are classified by their number of boundary crossings the Floquet multipliers are calculated. The Floquet multiplier with the maximum absolute value is depicted in figure 4.9. Black and white denote an absolute value of zero and one respectively. All (unstable) Floquet multipliers with an absolute value higher than one are set to one for clarity. This figure also clearly shows the boundaries. This can be explained by considering the monodromy matrices. Each time a switching boundary, in the phase plane, is crossed the monodromy matrix exhibits a discontinuity or jump. This jump (which is described by a saltation matrix) also affects the Floquet multipliers, so a change in number of boundary crossings will also cause a sudden change in Floquet multipliers.

This number of boundary crossing is not the only qualitative difference in the periodic solutions. figure 4.9, when compared to figure 4.8 shows an extra boundary between labels A and B. This suggests a change in the characteristics of the periodic orbit, although the number of crossings does

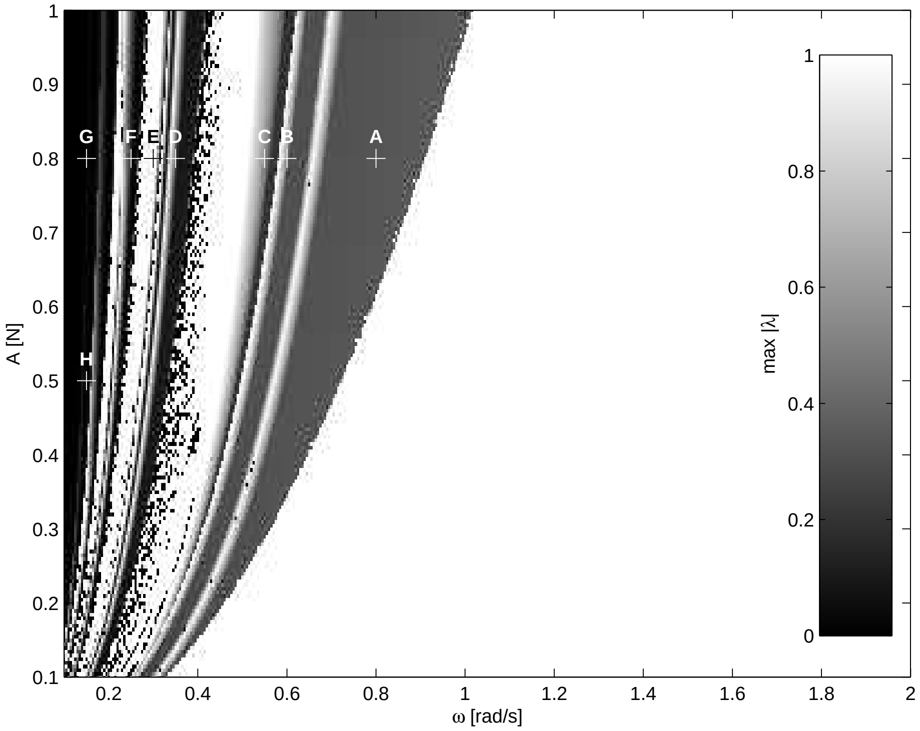

Figure 4.9: Classification of periodic orbits in $(A,\ \omega)$ space: Floquet multipliers

not change. This idea is verified in figure 4.10 (a) to (c), which shows the periodic orbits at labels A, B and C. The periodic orbit changes from being symmetric at A to asymmetric at B, without a change in the number of boundary crossings. Both the symmetric and asymmetric periodic orbits were already shown in figures 4.4 and 4.5, when the response diagram was discussed. The asymmetrical periodic orbit at point C does show extra boundary crossings. This change can be noticed in both figure 4.8 and 4.9.

Figure 4.10 (d) to (f) show the periodic orbits at points D, E and F, which show an increase in the number of crossings as the forcing frequency decreases. The periodic orbit at point E is again asymmetric. This could also have been concluded from the number of crossings. The number of boundary crossings for this periodic orbit is ten, which means the stoppers are hit five times in a period. Since five is odd, the periodic orbit has to be asymmetrical. It has to be noticed that a number of boundary crossings which is a multiple of four does not mean that the periodic orbit is symmetrical, as can be observed by considering the periodic orbit at point B in figure 4.10 (b).

For low excitation frequency ($\omega < 0.2$ rad/s), the amplitude of the forcing appears to have a larger influence on the number of crossings. Figure 4.10 (g) and (h) shows this influence for $\omega = 0.15$ rad/s. The periodic orbit at G shows higher harmonics that are entirely in subspace V_1 or V_3, so contact with a stopper is not lost. For a lower forcing amplitude, the force is too small to maintain this dynamics and contact with the stopper will be lost, causing an increase in the number of boundary crossings. Periodic orbit H in figure 4.10 (h) is an example.

Since figures 4.8 and 4.9 are created using an initial condition to force the periodic orbit to be in the center between the stoppers, a section on the top branch which overlaps the linear branch of the response diagram (figure 4.1) is not found. Figures 4.8 and 4.9 are therefore recreated using a different initial condition to enforce the possibility of finding periodic orbits on that section of the top branch of the response diagram. The result is depicted in figures 4.11 and 4.12, where the latter again shows the maximum absolute value of the Floquet multipliers.

The analytically calculated corner collision boundary is not dependent on the initial conditions.

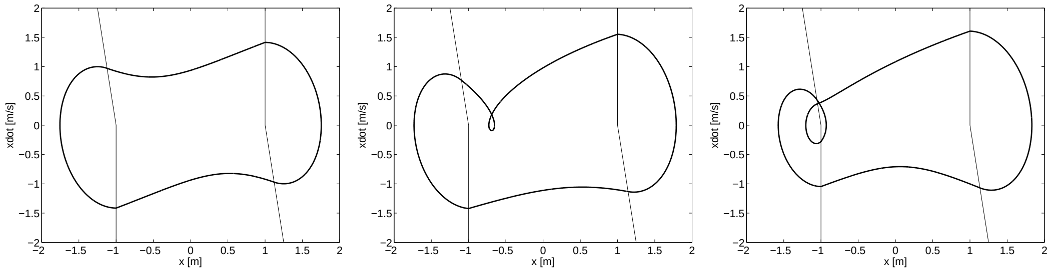

(a) Orbit A at $\omega = 0.8$ rad/s (b) Orbit B at $\omega = 0.6$ rad/s (c) Orbit C at $\omega = 0.55$ rad/s

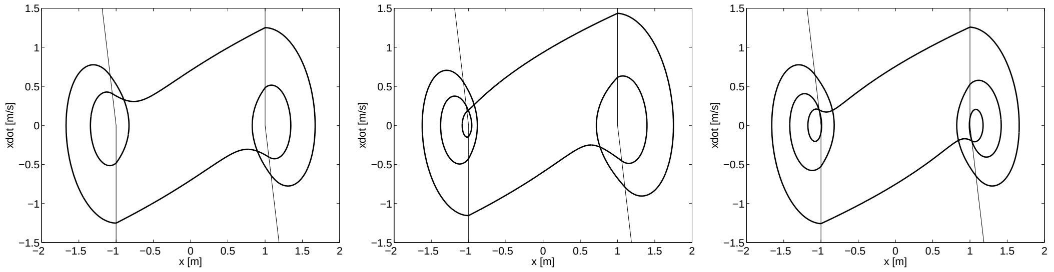

(d) Orbit D at $\omega = 0.35$ rad/s (e) Orbit E at $\omega = 0.3$ rad/s (f) Orbit F at $\omega = 0.25$ rad/s

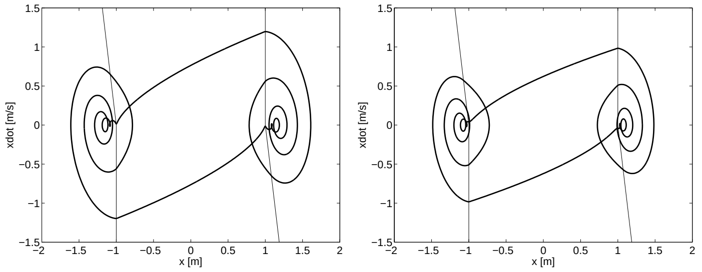

(g) Orbit G at $A = 0.8$ N (h) Orbit H at $A = 0.5$ N

Figure 4.10: Periodic orbits at the labels in figure 4.8

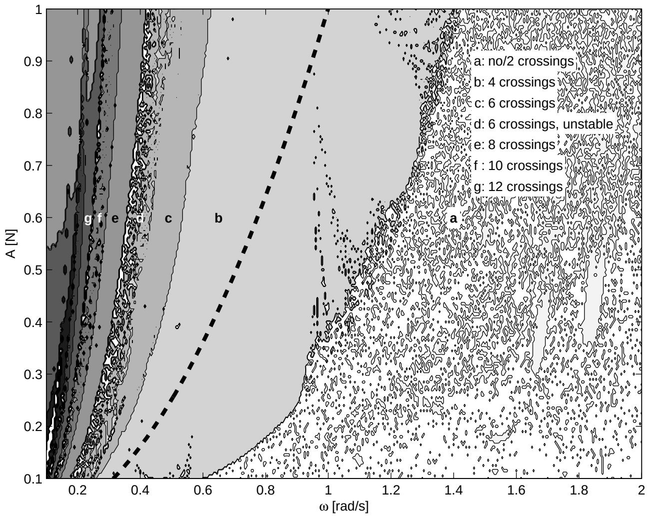

Figure 4.11: Classification of periodic orbits in $(A,\ \omega)$ space: boundary crossings – $\mathbf{x}_0 = [3,\ 0]^{\mathrm{T}}$

Further, the solutions and their characteristics are identical when the response exhibits more than four boundary crossings. This was expected, because the solution always hits the stoppers in this region. The diagram is different at the right side of the corner collision boundary. The region where the periodic solutions cross the boundaries four times is increased. A vague definition of the boundary can be seen where this region ends. On the right side of that boundary two situations occur: first, there are periodic orbits in V_2 that do not cross any boundary, as was observed earlier in relation to the rigid body motion and second, periodic orbits with two boundary crossings are found. This means that only one stopper is touched; figure 4.12 suggests that these periodic orbits are stable. Depending on the initial condition of the multiple shooting algorithm, which is obtained by simulation, either this solution or the non-touching solution is found, resulting in figures 4.11 and 4.12.

4.2 Multiple degree-of-freedom model

For the multiple degree-of-freedom model in figure 2.3, the analysis as is done for the single degree-of-freedom system is repeated. This results in the response diagram in figure 4.13. Again, the amplitude of the periodic response relative to the backlash gap (in relative coordinate $x_3 - x_2$) is depicted for different excitation frequencies ω at excitation amplitude $A = 1$ N. Stable solutions are depicted in solid lines, unstable periodic orbits are shown in dashed lines.

4.2.1 Periodic response

The response diagram for the MDOF system in figure 4.13 shows similar characteristics to that of the SDOF system in figure 4.1. The fold bifurcation is clearly present, giving similar stable branches connected by an unstable one as for the SDOF case at around $\omega = 1.2$ rad/s. When the amplitude of the periodic response is smaller than one, it moves between the stoppers without touching them. As for the SDOF system, these periodic orbits are not unique and can be shifted. However, for the MDOF system both masses 3 and 4 have to be shifted simultaneously to find these shifted periodic orbits.

The MDOF system also shows both symmetric and asymmetric solutions. When the (symmetric) top branch originating at the fold bifurcation is tracked for decreasing frequency, it loses stability at around $\omega = 0.98$ rad/s. At the same point an asymmetric and stable solution origi-

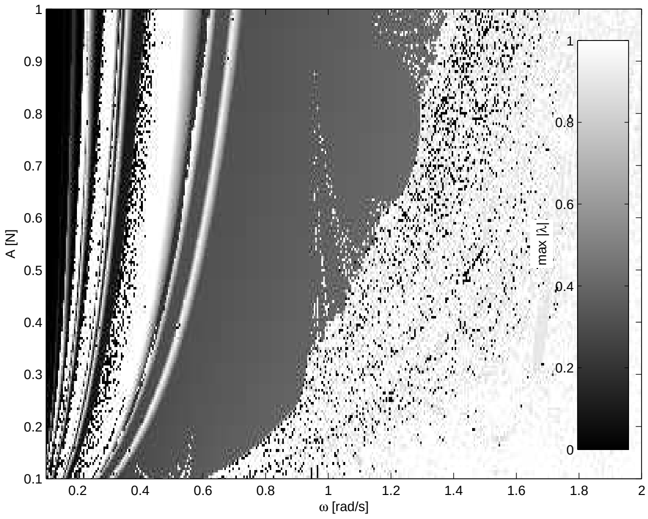

Figure 4.12: Classification of periodic orbits in $(A,\ \omega)$ space: Floquet multipliers – $\mathbf{x}_0 = [3,\ 0]^{\mathrm{T}}$

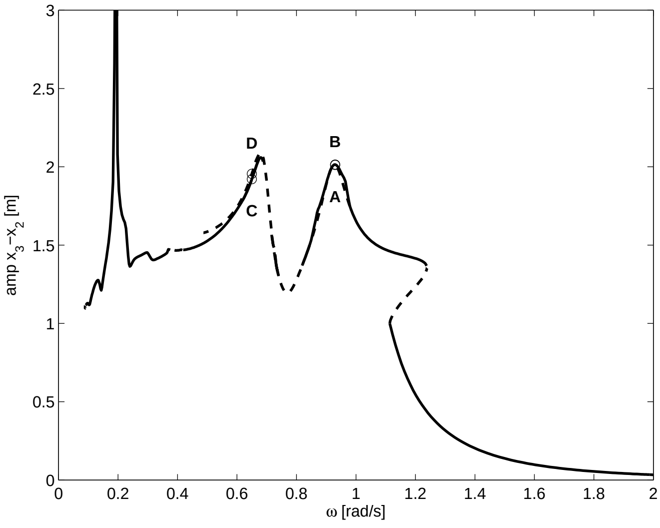

Figure 4.13: Response diagram of system (2.19) for forcing amplitude $A = 1$ N

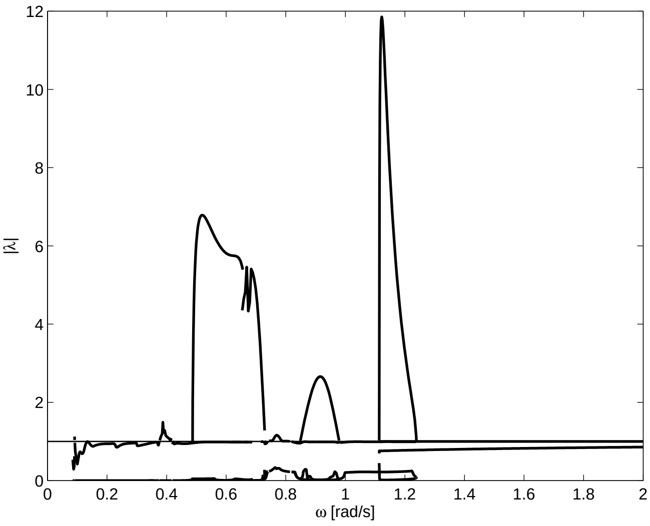

Figure 4.14: Floquet multipliers of the periodic orbits in figure 4.13

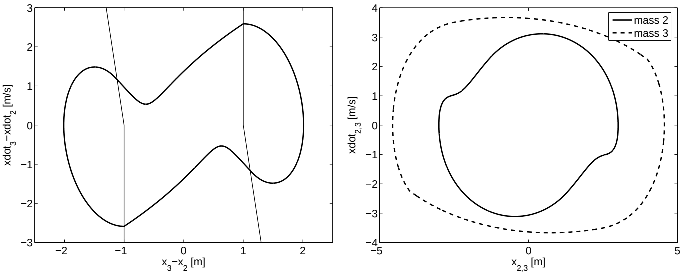

Figure 4.15: Periodic orbit at label A in figure 4.13 ($\omega = 0.93$ rad/s)

nates. Examples are shown in figures 4.15 and 4.16 which depict the unstable and stable periodic orbits respectively. The periodic orbit relative to the backlash gap is depicted in the left graphs, the right graphs show the orbits of masses 2 and 3, between which the backlash gap exists. The orbits of masses 2 and 3 also clearly show the symmetry and asymmetry. As for the SDOF system, mirrored (around $\mathbf{x} = \mathbf{0}$) versions of the asymmetrical periodic orbits can be found, because both stoppers are equal.

A similar situation is found in the other resonance peak of the response diagram in figure 4.13 around $\omega = 0.68$ rad/s. The periodic orbits at labels C and D are depicted in figure 4.17 and again show a symmetric (C) and asymmetric (D) solution. However, symmetry is not the only difference; there is also a difference in number of subspace boundary crossings, which will be explained in more detail in the next section.

4.2.2 Boundary Classification

The dynamics of the MDOF system is characterized by the number of boundary crossings of a periodic orbit. These periodic orbits are found in the same way as for the SDOF system, which yields figure 4.18. The dashed line denotes combinations of forcing frequency and amplitude where the amplitude of the periodic orbit (in $x_3 - x_2$) is b, calculated for the linear dynamics in the backlash region. As a result, periodic solutions that do not touch the stoppers can occur at the right side of that boundary. These periodic orbits are also found in the lower branch in

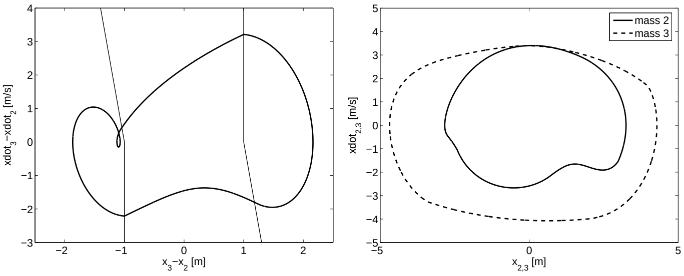

Figure 4.16: Periodic orbit at label B in figure 4.13 ($\omega = 0.93$ rad/s)

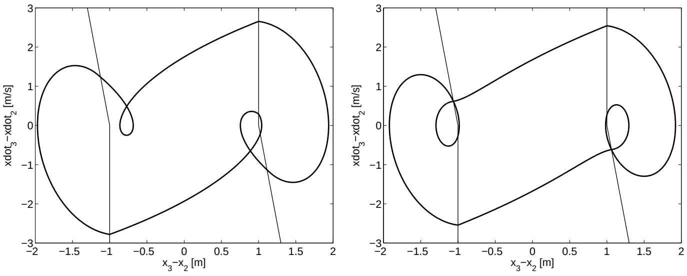

Figure 4.17: Periodic orbits at labels C (left) and D (right) in figure 4.13 ($\omega = 0.65$ rad/s)

the response diagram figure 4.13. However, figure 4.18 is created using an initial condition in a contact region, enforcing the possibility of finding solutions on the top branch of figure 4.13.

In the region with four boundary crossings, a V-shaped region of periodic orbits with six crossings can be found in figure 4.18. The periodic orbits at labels A and C are in this region, orbit B is in the region between these labels. Orbits A, B and C correspond to a forcing frequency of $\omega = 0.99$, 0.90, 0.85 rad/s respectively at a forcing amplitude $A = 1.5$ N. They are depicted in figure 4.20 and show a higher harmonic around or on the boundary. For excitation frequencies slightly higher than the frequency at label A ($\omega = 0.99$ rad/s), this higher harmonic is entirely in the backlash region. When the excitation frequency is decreased, the amplitude of the response increases, as can be seen in the response diagram in figure 4.13. This increase in amplitude causes the higher harmonic to be pushed over the boundary, resulting in a small region with six crossings (orbit A in figure 4.20). For even lower frequencies, the amplitude of the response decreases again, giving a similar effect as can be concluded from orbit C. Periodic orbit B shows the situation where the entire higher harmonic is in contact with a stopper, as is the case for the high response amplitude.

The same effect can be observed for lower frequencies, as is depicted in figure 4.21 for frequencies $\omega = 0.55$, 0.40, 0.25 rad/s at an excitation amplitude $A = 2$ N. This situation corresponds with the region containing the left two resonance peaks in the response diagram in figure 4.13. When the amplitude of the periodic response is high, the higher harmonics are totally in the contact regions as can be observed for orbits D and F. For the part of the response diagram with the lower amplitude between the two resonance peaks however, the higher harmonic also crosses the boundary, causing a higher number of boundary crossings. This can be observed in orbit E at the center graph in figure 4.21.

As explained before, the number of boundary crossings gives some information on the location of the higher harmonics. However, for high forcing amplitudes the loop caused by the higher harmonics reduces to a "bump", as can be seen in the right graph of figure 4.22. The graphs in this figure are created for forcing frequencies $\omega = 0.55$, 0.40 rad/s and amplitude $A = 2.8$ N. It can be seen that for decreasing frequency this "bump" crosses the subspace boundary before turning

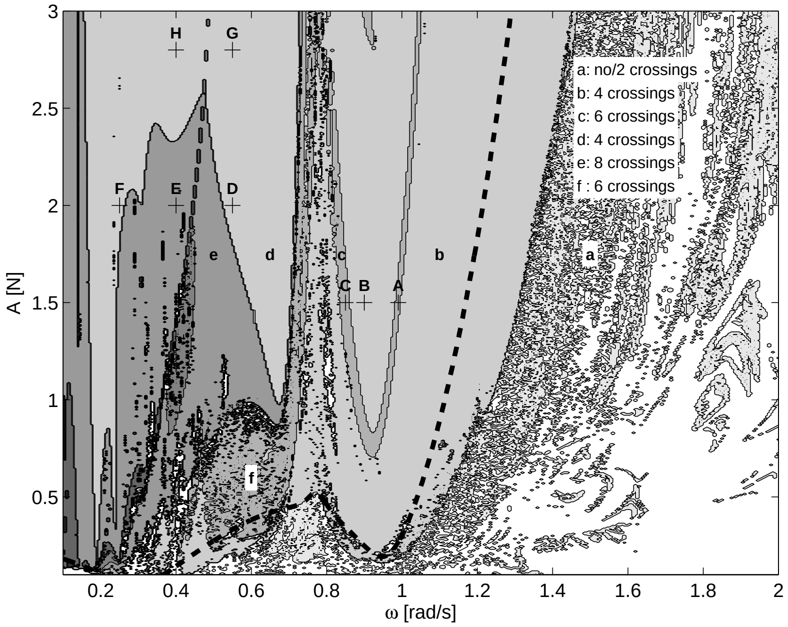

Figure 4.18: Classification of periodic orbits in $(A,\ \omega)$ space: boundary crossings

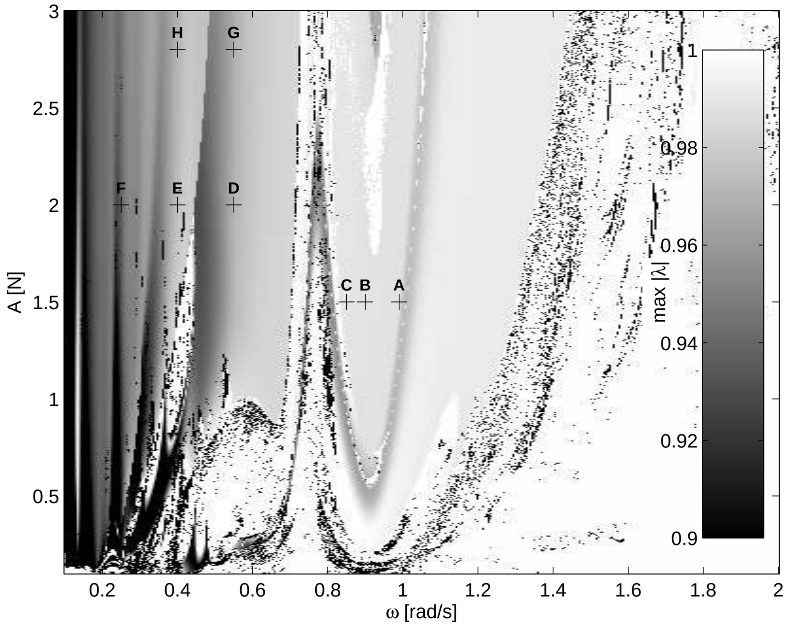

Figure 4.19: Classification of periodic orbits in $(A,\ \omega)$ space: Floquet multipliers

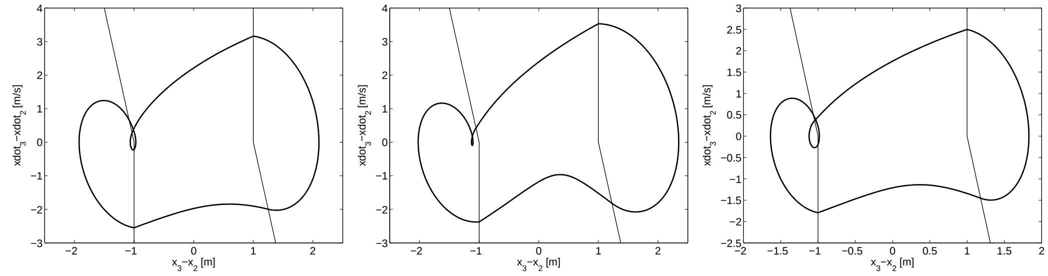

Figure 4.20: Periodic orbits at labels A, B and C in figure 4.18 respectively

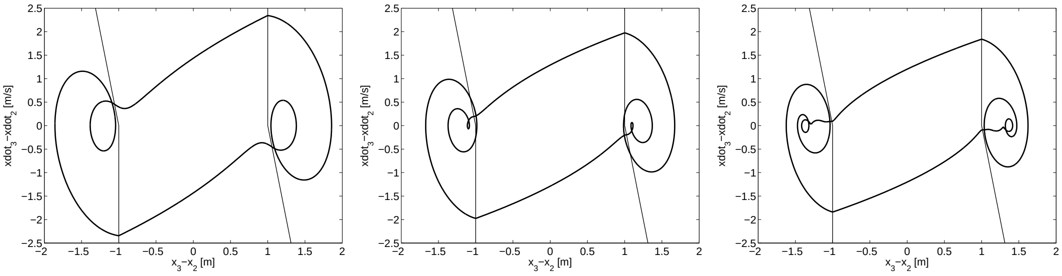

Figure 4.21: Periodic orbits at labels D, E and F in figure 4.18 respectively

into a small loop in orbit G in the left graph of figure 4.22. Since it turns into a loop after the boundary crossing, this crossing can not be detected by considering figure 4.18, which shows the number of boundary crossings. The crossing can however be detected by considering the Floquet multipliers; a jump between labels G and H can be seen in figure 4.19.

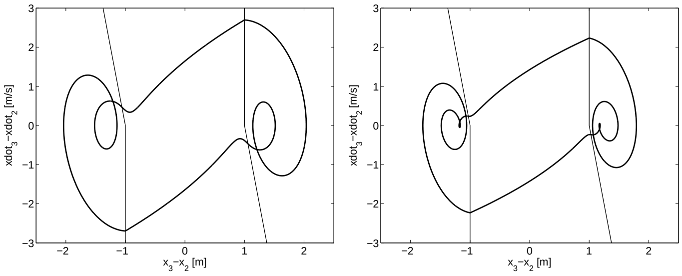

Figure 4.22: Periodic orbits at labels G and H in figure 4.18 respectively

Chapter 5

Observer design

In this chapter, the multiple degree-of-freedom system in figure 2.3 is considered. This model is loosely based on a gear transmission where backlash exists between two gears, modeled as masses 2 and 3. Masses 1 and 4 represent the motor and load masses or inertias respectively.

In practice, often only measurements of the output of the system are available and the total state is not known. However, it might be beneficial to have knowledge of the entire state, of which the backlash gap is of most interest. This information might be used to analyze or control the system. The design of the observer is based on [6].

5.1 Design

To design an observer, the system is written in a format that is similar to the piecewise linear system description in (3.1) in section 3.1. The difference is however that the offset of the global coordinate system is incorporated in a constant vector $\mathbf{a}_i$, which can be constructed by $\mathbf{a}_i = -\mathbf{A}_i \Delta \mathbf{x}_i$. This leads to:

$$\dot{\mathbf{x}} = \mathbf{A}_i \mathbf{x} + \mathbf{a}_i + \mathbf{B}u \tag{5.1}$$

Here, $i \in \{1,\ 2,\ 3\}$ denotes the subspace in which the description is valid. The matrices are given in appendix B.2. The output y is the position of the load, so the output matrix $\mathbf{C}$ is constant for all subspaces.

$$y = \mathbf{C}\mathbf{x}, \quad \mathbf{C} = \begin{bmatrix} 0 & 0 & 0 & 0 & 0 & 0 & 1 & 0 \end{bmatrix} \tag{5.2}$$

The observer is a copy of the system with output injection. The state of the observer is denoted by $\hat{\mathbf{x}}$, the subspace in which it operates by $j \in \{1,\ 2,\ 3\}$.

$$\dot{\hat{\mathbf{x}}} = \mathbf{A}_j \hat{\mathbf{x}} + \mathbf{a}_j + \mathbf{B}u + \mathbf{L}_j (y - \hat{y}) \tag{5.3}$$

$$\hat{y} = \mathbf{C}\hat{\mathbf{x}} \tag{5.4}$$

When the estimation error $\mathbf{e}$ is defined as $\mathbf{e} = \mathbf{x} - \hat{\mathbf{x}}$, the error dynamics are given by:

$$\begin{array}{ll} \dot{\mathbf{e}} = (\mathbf{A}_j - \mathbf{L}_j \mathbf{C})\mathbf{e}, & i = j \\ \dot{\mathbf{e}} = (\mathbf{A}_j - \mathbf{L}_j \mathbf{C})\mathbf{e} + (\mathbf{A}_i - \mathbf{A}_j)\mathbf{x} + (\mathbf{a}_i - \mathbf{a}_j), & i \neq j \end{array} \tag{5.5}$$

In total, there are nine error equations, depending on the system subspace i and the observer subspace j.

The error system (5.5) can be stabilized by searching for a (quadratic) Lyapunov function:

$$V(\mathbf{e}) = \mathbf{e}^{\mathrm{T}} \mathbf{P} \mathbf{e}, \quad \mathbf{P} = \mathbf{P}^{\mathrm{T}} > 0 \tag{5.6}$$

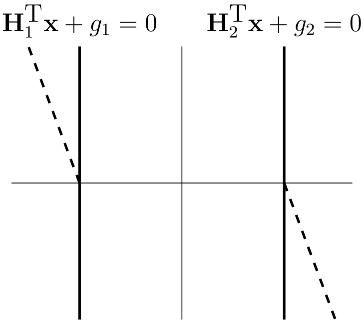

Figure 5.1: Simplified subspace boundaries for relaxation of the LMIs

Differentiation of the Lyapunov function yields:

$$\begin{aligned}
\dot{V} &= \mathbf{e}^{\mathrm{T}}\left((\mathbf{A}_j - \mathbf{L}_j\mathbf{C})^{\mathrm{T}}\mathbf{P} + \mathbf{P}(\mathbf{A}_j - \mathbf{L}_j\mathbf{C})\right)\mathbf{e}, && i = j \\
\dot{V} &= \mathbf{e}^{\mathrm{T}}\left((\mathbf{A}_j - \mathbf{L}_j\mathbf{C})^{\mathrm{T}}\mathbf{P} + \mathbf{P}(\mathbf{A}_j - \mathbf{L}_j\mathbf{C})\right)\mathbf{e} \\
&\quad + \mathbf{e}^{\mathrm{T}}\mathbf{P}(\mathbf{A}_i - \mathbf{A}_j)\mathbf{x} + \mathbf{x}^{\mathrm{T}}(\mathbf{A}_i - \mathbf{A}_j)^{\mathrm{T}}\mathbf{P}\mathbf{e} \\
&\quad + \mathbf{e}^{\mathrm{T}}\mathbf{P}(\mathbf{a}_i - \mathbf{a}_j) + (\mathbf{a}_i - \mathbf{a}_j)^{\mathrm{T}}\mathbf{P}\mathbf{e}, && i \neq j
\end{aligned} \tag{5.7}$$

The latter equation (for $i \neq j$) can be rewritten as:

$$\dot{V} = \begin{bmatrix} \mathbf{e} \\ \mathbf{x} \\ 1 \end{bmatrix}^{\mathrm{T}} \begin{bmatrix} (\mathbf{A}_j - \mathbf{L}_j\mathbf{C})^{\mathrm{T}}\mathbf{P} + \mathbf{P}(\mathbf{A}_j - \mathbf{L}_j\mathbf{C}) & \mathbf{P}(\mathbf{A}_i - \mathbf{A}_j) & \mathbf{P}(\mathbf{a}_i - \mathbf{a}_j) \\ (\mathbf{A}_i - \mathbf{A}_j)^{\mathrm{T}}\mathbf{P} & \mathbf{0} & \mathbf{0} \\ (\mathbf{a}_i - \mathbf{a}_j)^{\mathrm{T}}\mathbf{P} & \mathbf{0} & 0 \end{bmatrix} \begin{bmatrix} \mathbf{e} \\ \mathbf{x} \\ 1 \end{bmatrix} \tag{5.8}$$

To have stability of the error equations and therefore a converging observer the differentiated Lyapunov functions $\dot{V}$ has to be negative definite. This condition can be stated in *linear matrix inequalities* (LMIs) by using the notation in equation (5.8) (for $i \neq j$). When $i = j$, the expression in equation (5.7) can be used. This leads to a total of ten LMIs: three for the situations where both the system and observer are in the same subspace ($i = j$), six when they are not ($i \neq j$) and the condition for the matrix $\mathbf{P}$, which has to be positive definite. However, a feasible solution for this set of equations does not exist because of the zero-terms on the diagonal.

To get a set of feasible equations, the inequalities have to be relaxed. This is done by adding information on the different subspaces of the system. The inequalities that describe the conditions when the system and observer are not in the same subspace, only have to hold in the corresponding subspaces. By including this information, the inequalities become less conservative and the changes of finding a feasible solutions increase.

Both subspace boundaries consist of two parts as is discussed before and can be observed by the dashed line in figure 5.1. To simplify the problem, these boundaries are approximated by single linear boundaries, which are depicted as solid lines in figure 5.1. These linear boundaries can be written in the form:

$$\mathbf{H}_i^{\mathrm{T}}\mathbf{x} + g_i = 0 \tag{5.9}$$

Both boundaries only depend on the relative displacement between x_2 and x_3 and $\mathbf{H}_1$ and $\mathbf{H}_2$ are therefore equal. Only the position of the boundaries differs, as can be observed in the constants g_1 and g_2.

$$\mathbf{H}_1 = \mathbf{H}_2 = \begin{bmatrix} 0 & 0 & -1 & 0 & 1 & 0 & 0 & 0 \end{bmatrix}^{\mathrm{T}}, \; g_1 = b, \; g_2 = -b \tag{5.10}$$

Using these numbers, subspace one is characterized by $\mathbf{H}_1^{\mathrm{T}}\mathbf{x} + g_1 \leq 0$, while subspace two is defined by $\mathbf{H}_2^{\mathrm{T}}\mathbf{x} + g_2 \geq 0$.

To illustrate the relaxation of the inequalities using the boundaries, an example is considered. The system is assumed to be in contact with the left stopper (subspace one, $i = 1$), the observer is assumed to be in the backlash region ($j = 2$). First, the condition for the system is considered:

$$\mathbf{H}_1^{\mathrm{T}}\mathbf{x} + g_1 \leq 0 \tag{5.11}$$

This can be rewritten in matrix form, where the column vector $[\mathbf{e}^{\mathrm{T}},\ \mathbf{x}^{\mathrm{T}},\ 1]^{\mathrm{T}}$ is used to implement the boundary condition into the conditions for the Lyapunov function.

$$\begin{bmatrix} \mathbf{e} \\ \mathbf{x} \\ 1 \end{bmatrix}^{\mathrm{T}} \begin{bmatrix} \mathbf{0} & \mathbf{0} & \mathbf{0} \\ \mathbf{0} & \mathbf{0} & 0.5\mathbf{H}_1 \\ \mathbf{0} & 0.5\mathbf{H}_1^{\mathrm{T}} & g_1 \end{bmatrix} \begin{bmatrix} \mathbf{e} \\ \mathbf{x} \\ 1 \end{bmatrix} \leq 0 \tag{5.12}$$

For the observer, the following conditions hold (with $\hat{\mathbf{x}} = \mathbf{x} - \mathbf{e}$):

$$\mathbf{H}_1^{\mathrm{T}}\hat{\mathbf{x}} + g_1 = \mathbf{H}_1^{\mathrm{T}}(\mathbf{x} - \mathbf{e}) + g_1 \geq 0 \tag{5.13}$$

$$\mathbf{H}_2^{\mathrm{T}}\hat{\mathbf{x}} + g_2 = \mathbf{H}_2^{\mathrm{T}}(\mathbf{x} - \mathbf{e}) + g_2 \leq 0 \tag{5.14}$$

These are also rewritten using a quadratic matrix form:

$$\begin{bmatrix} \mathbf{e} \\ \mathbf{x} \\ 1 \end{bmatrix}^{\mathrm{T}} \begin{bmatrix} \mathbf{0} & \mathbf{0} & 0.5\mathbf{H}_1 \\ \mathbf{0} & \mathbf{0} & -0.5\mathbf{H}_1 \\ 0.5\mathbf{H}_1^{\mathrm{T}} & -0.5\mathbf{H}_1^{\mathrm{T}} & -g_1 \end{bmatrix} \begin{bmatrix} \mathbf{e} \\ \mathbf{x} \\ 1 \end{bmatrix} \leq 0 \tag{5.15}$$

$$\begin{bmatrix} \mathbf{e} \\ \mathbf{x} \\ 1 \end{bmatrix}^{\mathrm{T}} \begin{bmatrix} \mathbf{0} & \mathbf{0} & -0.5\mathbf{H}_2 \\ \mathbf{0} & \mathbf{0} & 0.5\mathbf{H}_2 \\ -0.5\mathbf{H}_2^{\mathrm{T}} & 0.5\mathbf{H}_2^{\mathrm{T}} & g_2 \end{bmatrix} \begin{bmatrix} \mathbf{e} \\ \mathbf{x} \\ 1 \end{bmatrix} \leq 0 \tag{5.16}$$

Condition (5.8) (for $i = 1$, $j = 2$) only has to hold when the system and observer are in the corresponding subspace, so when (5.12), (5.15) and (5.16) hold. These four conditions can be converted into a single condition by using the $\mathcal{S}$-procedure, which is explained in appendix E. Using the $\mathcal{S}$-procedure, the condition becomes:

$$\begin{bmatrix} \begin{array}{c}(\mathbf{A}_2 - \mathbf{L}_2\mathbf{C})^{\mathrm{T}}\mathbf{P} \\ +\mathbf{P}(\mathbf{A}_2 - \mathbf{L}_2\mathbf{C})\end{array} & \mathbf{P}(\mathbf{A}_1 - \mathbf{A}_2) & \begin{array}{c}\mathbf{P}(\mathbf{a}_1 - \mathbf{a}_2) \\ +0.5(-\lambda_{122}\mathbf{H}_1 + \lambda_{123}\mathbf{H}_2)\end{array} \\ (\mathbf{A}_1 - \mathbf{A}_2)^{\mathrm{T}}\mathbf{P} & \mathbf{0} & \begin{array}{c}0.5(-\lambda_{121}\mathbf{H}_1 \\ +\lambda_{122}\mathbf{H}_1 - \lambda_{123}\mathbf{H}_2)\end{array} \\ \begin{array}{c}(\mathbf{a}_1 - \mathbf{a}_2)^{\mathrm{T}}\mathbf{P} \\ +0.5(-\lambda_{122}\mathbf{H}_1^{\mathrm{T}} + \lambda_{123}\mathbf{H}_2^{\mathrm{T}})\end{array} & \begin{array}{c}0.5(-\lambda_{121}\mathbf{H}_1^{\mathrm{T}} \\ +\lambda_{122}\mathbf{H}_1^{\mathrm{T}} - \lambda_{123}\mathbf{H}_2^{\mathrm{T}})\end{array} & -\lambda_{121}g_1 + \lambda_{122}g_1 - \lambda_{123}g_2 \end{bmatrix} < 0 \tag{5.17}$$

This condition must hold for $\mathbf{P} = \mathbf{P}^{\mathrm{T}} > 0$ and $\lambda_{12k} > 0$ to find a feasible solution. All conditions that must hold when the system and observer are not in the same subspace can be created in a similar way. It has to be noted that these linear matrix inequalities are not linear in the parameters $\{\mathbf{P},\ \mathbf{L}_j, \lambda_{ijk}\}$ but they are in $\{\mathbf{P},\ \mathbf{PL}_j, \lambda_{ijk}\}$. For the cases when the system and observer are in the same subspace, the boundary conditions do not have to be added.

The conditions as derived before can only be used when the system is continuous. Since the dampers in the stoppers of the MDOF system with backlash cause this system to be discontinuous, the conditions have to be adapted. Because of the discontinuity, convergence of the error can no longer be proven. However, boundedness of the error can be shown by considering the quadratic constraint ($\varepsilon > 0$):

$$||\mathbf{e}||^2 \geq \varepsilon^2 ||\mathbf{x}||^2 \tag{5.18}$$

Here, $||\cdot||$ denotes the 2-norm. Next, $\mathbf{x}$ is assumed to be eventually bounded by x_{max}. This means that for all $\delta > 0$, there exists a $T_0 > 0$ such that:

$$||\mathbf{x}|| \leq x_{max} + \delta, \quad \forall t > T_0 \tag{5.19}$$

This is equivalent to:

$$\limsup_{t\to\infty} ||\mathbf{x}|| \leq x_{max} \tag{5.20}$$

Next, the maximum value of the Lyapunov function V is defined in a set which is the inverse of condition (5.18) including some small overlap:

$$V^{\delta}_{max} = \sup_{||\mathbf{e}|| \leq \varepsilon x_{max}+\delta} V \tag{5.21}$$

Using this maximum value, a set S_δ can be defined by:

$$S_\delta = \left\{ \mathbf{e} \mid V(\mathbf{e}) < V^{\delta}_{max} \right\} \tag{5.22}$$

If a solution to the LMIs can be found by adding constraint (5.18), it means that $\dot{V} < 0$ when this constraint holds. Since the set S_δ is defined by using the inverse of (5.18) and some overlap, the statement $\dot{V} < 0$ for $\mathbf{e} \notin S_\delta$ also holds. This implies that S_δ is invariant and attractive. Therefore, the error reduces until it arrives in the set S_δ.

When the linear matrix inequalities are solved, the bounds on $\mathbf{P}$ can be calculated.

$$\gamma_1 \mathbf{I} \leq \mathbf{P} \leq \gamma_2 \mathbf{I} \tag{5.23}$$

Using this in combination with the definition of V^{δ}_{max} gives an upper bound for V^{δ}_{max}.

$$V^{\delta}_{max} \leq \gamma_2 (\varepsilon x_{max} + \delta)^2 \tag{5.24}$$

The definition of the Lyapunov function in (5.6) gives:

$$\gamma_1 ||\mathbf{e}||^2 \leq V(\mathbf{e}) \tag{5.25}$$

Combining these bounds gives a bound on $||\mathbf{e}||$. For all $\delta > 0$, there exists a $T_0 > 0$ such that:

$$||\mathbf{e}|| \leq \sqrt{\frac{\gamma_2}{\gamma_1}} (\varepsilon x_{max} + \delta), \quad \forall t > T_0 \tag{5.26}$$

Using $e_{max} = \limsup_{t\to\infty} ||\mathbf{e}||$, this condition can be rewritten to:

$$e_{max} \leq \sqrt{\frac{\gamma_2}{\gamma_1}} \varepsilon x_{max} \tag{5.27}$$

Now it is proven that the addition of the constraint (5.18) leads to an error that is upper bounded by (5.27). Constraint (5.18) is therefore added to the linear matrix inequalities (of which (5.17) is an example), again using the $\mathcal{S}$-procedure. For this example, the new inequality is (with $\mu_{ij} > 0$):

$$\begin{bmatrix} \begin{array}{c} (\mathbf{A}_2 - \mathbf{L}_2\mathbf{C})^{\mathrm{T}}\mathbf{P} \\ +\mathbf{P}(\mathbf{A}_2 - \mathbf{L}_2\mathbf{C}) + \mu_{12}\mathbf{I} \end{array} & \mathbf{P}(\mathbf{A}_1 - \mathbf{A}_2) & \begin{array}{c} \mathbf{P}(\mathbf{a}_1 - \mathbf{a}_2) \\ +0.5(-\lambda_{122}\mathbf{H}_1 + \lambda_{123}\mathbf{H}_2) \end{array} \\ (\mathbf{A}_1 - \mathbf{A}_2)^{\mathrm{T}}\mathbf{P} & -\mu_{12}\varepsilon^2\mathbf{I} & \begin{array}{c} 0.5(-\lambda_{121}\mathbf{H}_1 \\ +\lambda_{122}\mathbf{H}_1 - \lambda_{123}\mathbf{H}_2) \end{array} \\ \begin{array}{c} (\mathbf{a}_1 - \mathbf{a}_2)^{\mathrm{T}}\mathbf{P} \\ +0.5(-\lambda_{122}\mathbf{H}_1^{\mathrm{T}} + \lambda_{123}\mathbf{H}_2^{\mathrm{T}}) \end{array} & \begin{array}{c} 0.5(-\lambda_{121}\mathbf{H}_1^{\mathrm{T}} \\ +\lambda_{122}\mathbf{H}_1^{\mathrm{T}} - \lambda_{123}\mathbf{H}_2^{\mathrm{T}}) \end{array} & -\lambda_{121}g_1 + \lambda_{122}g_1 - \lambda_{123}g_2 \end{bmatrix} < 0 \tag{5.28}$$

The inequalities for all different combinations of system and observer subspace can be created similarly. It has to be noted that the conditions for $(i = j)$ are already implied by these conditions, since they are equal to the upper-left terms in the inequality. Therefore, the inequalities given in (5.7) (for $i = j$) are redundant. All inequalities can be found in appendix D.

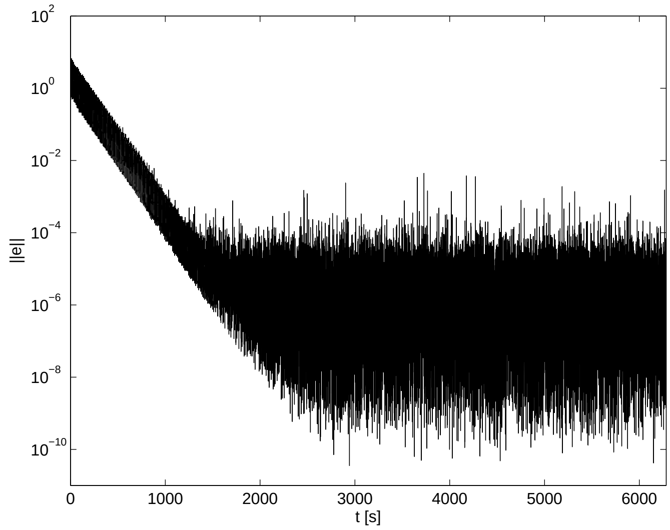

Figure 5.2: Observer error $||e||$ for $\varepsilon = 0.65$

In order to prove a small estimation error, $\sqrt{\gamma_2/\gamma_1}\varepsilon$ in (5.27) should be small. To simplify the problem, the inequality $\mathbf{P} > 0$ is replaced by:

$$\mathbf{P} > \mathbf{I} \tag{5.29}$$

This inequality implies that $\gamma_1 = 1$ and does not change the feasibility of the set of LMIs, because the other variables (λ_{ijk}, μ_{ij}) can be scaled accordingly. The problem is now reduced to minimizing $\sqrt{\gamma_2}\varepsilon$. However, by implementing the additional constraint (5.18), the set of inequalities is not linear anymore because of the $\mu_{12}\varepsilon^2$ term. Therefore, ε is chosen before minimizing γ_2 under the LMI constraints.

5.2 Results

First, the minimum value of ε for which a feasible solution exists is obtained iteratively. The result is $\varepsilon = 0.65$, which leads to $\sqrt{\gamma_2}\varepsilon = 1.49 \cdot 10^4$. It is clear that this value has no physical relevance; the errorbound should only be a fraction of x_{max} to have a good observer. The observer gains can be found in appendix F.

The simulation result for this observer is shown in figures 5.2 and 5.3. The simulation is done using the a forcing frequency of 1 rad/s and an amplitude of 1 N; the initial conditions are $\mathbf{x}_0 = [0, 0, 0, 0, 2, 0, 2, 0]^{\mathrm{T}}$ for the system and $\hat{\mathbf{x}}_0 = \mathbf{0}$ for the observer. This gives a solution that is bounded by $x_{max} = 108$. Although the boundaries are approximated in the relaxation of the LMIs, for simulation the real system is used. Figure 5.2 shows the 2-norm of the error $\mathbf{x} - \hat{\mathbf{x}}$ in logarithmic scale. It clearly shows that the errorbound e_{max} is much smaller than was expected theoretically. This can also be concluded from figure 5.3, which shows the relative coordinate in the backlash region $x_3 - x_2$ for both the system and observer and the corresponding error. The observer matches the system closely and can therefore be used to estimate the active subspaces of the system.

On the other hand, figure 5.2 shows that the observer only converges very slow. It takes about 2500 s (about 400 periods) to converge, which is not fast enough for practical applications.

Although the observation error is much smaller than expected, the factor $\sqrt{\gamma_2}\varepsilon$ is reduced by changing ε. For $\varepsilon = 9.5$, the optimum is found to be $\sqrt{\gamma_2}\varepsilon = 1.44 \cdot 10^3$. This is still too high for any practical relevance, but is an improvement of about a factor 10 when compared to the

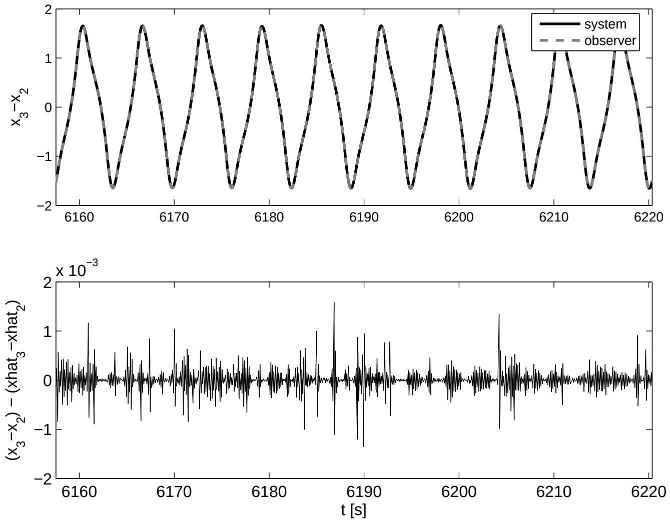

Figure 5.3: Observer error in backlash coordinate $x_3 - x_2$ for $\varepsilon = 0.65$

result for $\varepsilon = 0.65$. A drawback of this new design is that the matrices $\mathbf{A}_1 - \mathbf{L}_i\mathbf{C}$ that (partially) describe the error dynamics have eigenvalues at about $-7 \cdot 10^4$. This causes simulations to be very time-consuming. This is the reason that this observer is only simulated for 10 periods, as is depicted in figures 5.4 and 5.5. For this simulation, the initial condition is the final result of the simulation for the observer with $\varepsilon = 0.65$.

As can be seen in figure 5.4 and table 5.1, the norm of the error is smaller for the observer with $\varepsilon = 9.5$. Again, this result is far better then was expected by the value of $\sqrt{\gamma_2}\varepsilon$. Figure 5.5 and table 5.1 show however, that the error in the relative coordinate $x_3 - x_2$ is larger for $\varepsilon = 9.5$, except for some extreme values. It is difficult to draw some conclusions on the performance of this observer because of the limited simulation data.

Table 5.1: Observer errors (with $e_b = (x_3 - x_2) - (\hat{x}_3 - \hat{x}_2)$)

ε	$\frac{1}{T}\int_0^T \|\|\mathbf{e}(\tau)\|\| \mathrm{d}\tau$	$\frac{1}{T}\int_0^T e_b(\tau)^2 \mathrm{d}\tau$
0.65	$4.94 \cdot 10^{-6}$	$7.00 \cdot 10^{-8}$
9.5	$9.14 \cdot 10^{-7}$	$3.51 \cdot 10^{-7}$
Figure	5.4	5.5

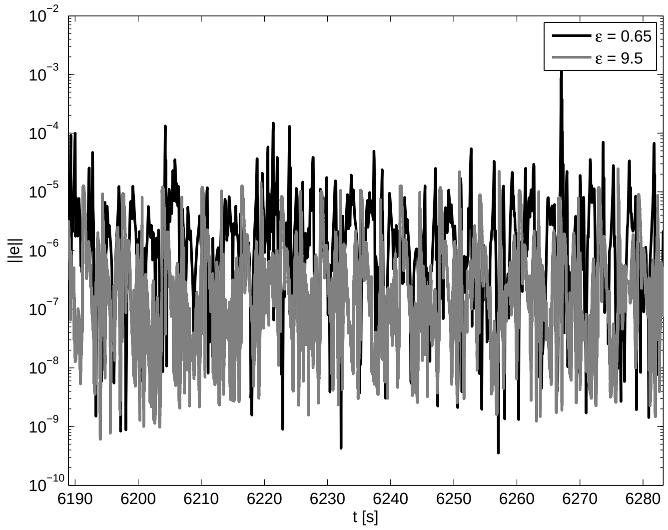

Figure 5.4: Observer error $||e||$ for both observers

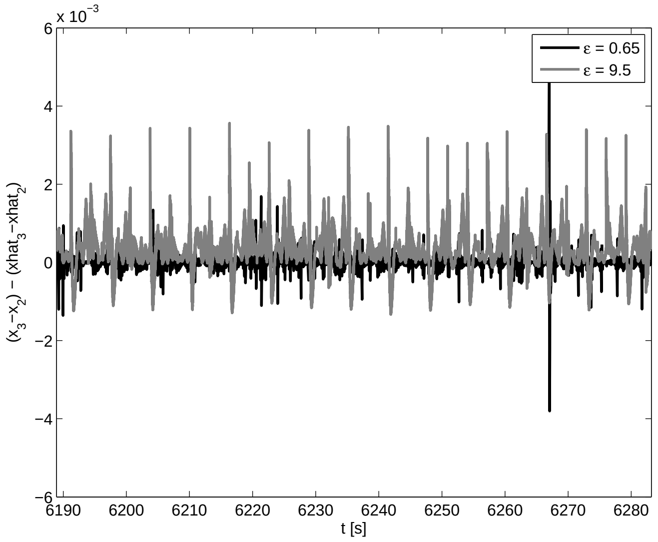

Figure 5.5: Observer error in backlash coordinate $x_3 - x_2$ for both observers

Chapter 6

Conclusions & Recommendations

6.1 Conclusions

In this report, a single degree-of-freedom and multiple degree-of-freedom system with backlash are studied for their responses under periodic excitation. Characteristic phenomena as stability and symmetry are discussed for these periodic orbits. Further, the responses are classified by their number of subspace boundary crossings and Floquet multipliers in the parameter space of forcing frequency and amplitude. It is shown that the Floquet multipliers undergo a sudden change when the number of subspace boundary crossings of a periodic orbit changes. Therefore, they give the same classification. Next, the Floquet multipliers indicate some additional characteristics, like symmetry.

The systems with backlash are modeled as piecewise linear systems. A simulation method to calculate the flow of such systems under periodic excitation by using analytical solutions in the linear subspaces is presented. This method also calculates the subspace boundary crossing times, which allows for analytical calculation of the fundamental solution matrix for an orbit. Hereto, saltation matrices as well as fundamental solution matrices for linear systems are used. The simulation method is integrated in the multiple shooting algorithm, which is used to estimate periodic orbits.

For the multiple degree-of-freedom system an observer is designed. This observer is created by solving a set of linear matrix inequalities that result from the error equations in combination with a single Lyapunov function. These linear matrix inequalities are relaxed by using approximations of the subspace boundaries and are shown to give an errorbound for discontinuous systems. However, the errorbound is too high to have any practical relevance. Yet, simulation results show a small error, but the observer converges only slowly.

6.2 Recommendations

The recommendations result from both the work done on the classification of periodic orbits and observer design. The recommendation regarding the classification of periodic orbits for a system with backlash are:

- The classification of periodic orbits might be carried out for systems with backlash with periodically varying stopper stiffness and damping, which is characteristic for gear systems. Some preliminary analysis is done for this case, but this did not show a dramatic change in the results.
- The effect of changing parameters as mass, stiffness and damping on both the response diagram and boundary classification might be investigated.
- The periodic orbits are classified by the Floquet multiplier with the largest modulus. However, the changes in other Floquet multipliers might also be of interest.

The analysis of the designed observer leads to the following recommendations:

- The observer analysis shows a significant difference in the theoretically calculated errorbound and simulation results. The cause of this discrepancy is unknown and requires further research.
- The performance of the observer is not that good and might be improved. This mainly relates to the convergence rate.

Bibliography

[1] G.W. Blankenship and A. Kahraman. Steady state forced response of a mechanical oscillator with combined parametric excitation and clearance type non-linearity. *Journal of Sound and Vibration*, 185(5):743–765, 1995.

[2] J.H. Bonsel, R.H.B. Fey, and H. Nijmeijer. Application of a dynamic vibration absorber to a piecewise linear beam system. *Nonlinear Dynamics*, 37:227–243, 2004.

[3] M. di Bernardo, C.J. Budd, and A.R. Champneys. Grazing and border-collision in piecewise-smooth systems: a unified analytical framework. *Physical Review Letters*, 86(12), 2001.

[4] Y. Dumont. Simulations of beam vibrations between stops: comparison of several numerical approaches. In *Proceedings of ENOC*, August 2005.

[5] A. Fidlin. On the strongly nonlinear behavior of an oscillator in a clearance. In *Proceedings of ENOC*, pages 389–397, August 2005.

[6] A.Lj. Juloski, W.P.M.H. Heemels, and S. Weiland. Observer design for a class of piece-wise affine systems. In *Proceedings of the 41st IEEE Conference on Decision and Control*, 2002.

[7] T.C. Kim, T.E. Rook, and R. Singh. Super- and sub-harmonic response calculations for a torsional system with clearance non-linearity using harmonic balance method. *Journal of Sound and Vibration*, 281(2–3):965–993, 2005.

[8] R.I. Leine and H. Nijmeijer. *Dynamics and bifurcations of non-smooth mechanical systems*, volume 18 of *Lecture Notes in Applied and Computational Mechanics*. Springer, 2004.

[9] R.I. Leine and D.H. van Campen. Discontinuous bifurcation of periodic solutions. *Mathematical and computer modelling*, 36:259–273, 2002.

[10] G. Litak and M.I. Friswell. Vibration in gear systems. *Chaos, Solitons and Fractals*, 16:795–800, 2003.

[11] S. Natsiavas. On the dynamics of oscillators with bi-linear damping and stiffness. *International Journal of Non-Linear Mechanics*, 25(5):535–554, 1990.

[12] S. Natsiavas. Stability and bifurcation analysis for oscillators with motion limiting constraints. *Journal of Sound and Vibration*, 141(1):97–102, 1990.

[13] F. Peterka, T. Kotera, and S. Čipera. Explanation of appearance and characteristics of intermittency chaos of the impact oscillator. *Chaos, Solitons and Fractals*, 19:1251–1259, 2004.

[14] K. Szabelski, G. Litak, J Warmiński, and G. Spuz-Szpos. Chaotic vibrations of the parametric system with backlash and non-linear elasticity. In *Proceedings of EUROMECH, 2nd European Nonlinear Oscillation Conference*, 1996.

[15] J.M.T. Thompson. Complex dynamics of compliant off-shore structures. *Proceedings of the Royal Society of London. Series A, Mathematical and Physical Sciences*, 387(1793):407–427, 1983.

[16] M. Wiercigroch, V.W.T. Sin, and K. Li. Measurement of chaotic vibration in a symmetrically piecewise linear oscillator. *Chaos, Solitons and Fractals*, 9(1/2):209–220, 1998.

Appendix A

Analysis methodology

A.1 Filippov's solution concept

An n-dimensional discontinuous dynamical system is considered.

$$\dot{\mathbf{x}} = \mathbf{f}(t, \mathbf{x}(t)) = \begin{cases} \mathbf{f}_-(t, \mathbf{x}(t)), & \mathbf{x} \in V_- \\ \mathbf{f}_+(t, \mathbf{x}(t)), & \mathbf{x} \in V_+ \end{cases} \tag{A.1}$$

This system, with initial condition $\mathbf{x}(0) = \mathbf{x}_0$, only has two subspaces, whereas the backlash systems under consideration have three. However, the theory as discussed here can easily be extended to the situation with more subspaces. Here, the subspaces V_- and V_+ are separated by a switching boundary Σ, which is defined by the scalar switching function $h(\mathbf{x})$.

$$V_- = \{\mathbf{x} \in \mathbb{R}^n \mid h(\mathbf{x}) < 0\} \tag{A.2}$$

$$\Sigma = \{\mathbf{x} \in \mathbb{R}^n \mid h(\mathbf{x}) = 0\} \tag{A.3}$$

$$V_+ = \{\mathbf{x} \in \mathbb{R}^n \mid h(\mathbf{x}) > 0\} \tag{A.4}$$

The right hand side of (A.1) is assumed to be continuous and smooth on V_- and V_+, but is discontinuous on Σ. It is not required that $\mathbf{f}_-(t, \mathbf{x}(t))$ and $\mathbf{f}_+(t, \mathbf{x}(t))$ agree on Σ. The system (A.1) is not defined on Σ, but this can be overcome by the set-valued extension $\mathbf{F}(t, \mathbf{x})$.

$$\dot{\mathbf{x}} \in \mathbf{F}(t, \mathbf{x}(t)) = \begin{cases} \mathbf{f}_-(t, \mathbf{x}(t)), & \mathbf{x} \in V_- \\ \overline{\mathrm{co}}\{\mathbf{f}_-(t, \mathbf{x}(t)), \mathbf{f}_+(t, \mathbf{x}(t))\}, & \mathbf{x} \in \Sigma \\ \mathbf{f}_+(t, \mathbf{x}(t)), & \mathbf{x} \in V_+ \end{cases} \tag{A.5}$$

Here, $\overline{\mathrm{co}}\{\mathbf{f}_-, \mathbf{f}_+\}$ is defined as:

$$\overline{\mathrm{co}}\{\mathbf{f}_-, \mathbf{f}_+\} = \{(1-q)\mathbf{f}_- + q\mathbf{f}_+, \ \forall q \in [0, 1]\} \tag{A.6}$$

The discontinuous system (A.1) is know extended to a differential inclusion (A.5), which is known as *Filippov's convex method* [8].

Now, a *solution in the sense of Filippov* can be defined. An absolute continuous function $\mathbf{x}(t) : [0, \tau] \to \mathbb{R}^n$ is a solution of the discontinuous differential equation $\dot{\mathbf{x}} = \mathbf{f}(t, \mathbf{x})$ (A.1) in the sense of Filippov if for almost all $t \in [0, \tau]$ it holds that $\dot{\mathbf{x}}(t) \in \mathbf{F}(t, \mathbf{x}(t))$.

A.2 Periodic orbits & stability

An n-dimensional non-autonomous nonlinear dynamical system is considered.

$$\dot{\mathbf{x}}(t) = \mathbf{f}(t, \mathbf{x}(t)), \quad \mathbf{x}(t_0) = \mathbf{x}_0 \tag{A.7}$$

The solution of the non-autonomous system after a time lapse t_d starting at t_0 with initial condition $\mathbf{x}_0$ is denoted by $\varphi_{t_d}(t_0, \mathbf{x}_0) \equiv \varphi(t_0+t_d, t_0, \mathbf{x}_0)$. A time-periodic non-autonomous system is defined by the additional property:

$$\mathbf{f}(t, \mathbf{x}) = \mathbf{f}(t+T, \mathbf{x}), \quad \forall \mathbf{x} \in \mathbb{R}^n, \ \forall t \tag{A.8}$$

Here, $T > 0$ is the minimal period time of the system. A periodic orbit is denoted by $\varphi^p(t_0 + T, t_0, \mathbf{x}_0)$ and is defined by:

$$\varphi^p(t_0 + kT, t_0, \mathbf{x}_0) = \mathbf{x}_0, \quad k = 0, 1, 2, \ldots \tag{A.9}$$

Here, $T > 0$ is the minimal period time of the periodic solution. When a non-autonomous system has a periodic solution as defined by (A.9), it holds that $\dot{\mathbf{x}}(t+T) = \dot{\mathbf{x}}(t)$ which implies property (A.8). As a result, if a non-autonomous system has a periodic solution of period T, the system is time-periodic of the same period T (or a fraction thereof).

To analyze the stability of a periodic solution the trajectory $\mathbf{x}^p(t) = \varphi(t, t_0, \mathbf{x}_0)$, which is a periodic solution of the non-autonomous system (A.7), is considered. The stability properties can be determined by linearizing the system around this trajectory. Therefore, a perturbed solution $\mathbf{x}(t) = \mathbf{x}^p(t) + \Delta\mathbf{x}(t)$ is considered. Equation (A.7) must be satisfied:

$$\begin{aligned} \dot{\mathbf{x}}^p(t) + \Delta\dot{\mathbf{x}}(t) &= \mathbf{f}(t, \mathbf{x}^p(t) + \Delta\mathbf{x}(t)) \\ &= \mathbf{f}(t, \mathbf{x}^p(t)) + \left.\frac{\partial \mathbf{f}(t, \mathbf{x})}{\partial \mathbf{x}}\right|_{\mathbf{x}^p(t)} \Delta\mathbf{x}(t) + H.O.T. \end{aligned} \tag{A.10}$$

Here, $H.O.T.$ denote the higher-order terms. Because $\dot{\mathbf{x}}^p(t) = \mathbf{f}(t, \mathbf{x}^p(t))$, the equation reduces to:

$$\Delta\dot{\mathbf{x}}(t) = \left.\frac{\partial \mathbf{f}(t, \mathbf{x})}{\partial \mathbf{x}}\right|_{\mathbf{x}^p(t)} \Delta\mathbf{x}(t) + H.O.T. \tag{A.11}$$

This equation describes how a small perturbation on the periodic solution evolves over time. When only infinitely small perturbations are considered, the higher-order terms vanish and a linear (but in general time-varying) differential equation remains.

A.3 Fundamental solution matrix

The solutions of (A.11) for initial conditions $\phi_i(t_0, t_0, \mathbf{x}^p(t_0)) = \mathbf{e}_i$ are considered. Here, $\mathbf{e}_i$ is a unit column vector with zeros at every row except the i-th row. The solutions $\phi_i(t, t_0, \mathbf{x}^p(t_0))$ are obtained and stored in the *fundamental solution matrix* $\mathbf{\Phi}(t, t_0, \mathbf{x}^p(t_0))$ [8].

$$\mathbf{\Phi}(t, t_0, \mathbf{x}^p(t_0)) = [\phi_1(t, t_0, \mathbf{x}^p(t_0)), \ldots, \phi_n(t, t_0, \mathbf{x}^p(t_0))] \tag{A.12}$$

All columns of the fundamental solution matrix are solutions of the differential equation (A.11), so this also holds for the entire matrix:

$$\dot{\mathbf{\Phi}}(t, t_0, \mathbf{x}^p(t_0)) = \left.\frac{\partial \mathbf{f}(t, \mathbf{x})}{\partial \mathbf{x}}\right|_{\mathbf{x}^p(t)} \mathbf{\Phi}(t_0, t_0, \mathbf{x}^p(t_0)), \quad \mathbf{\Phi}(t_0, t_0, \mathbf{x}^p(t_0)) = \mathbf{I}_n \tag{A.13}$$

Here, $\mathbf{I}_n$ is the $n \times n$ unity matrix. Since (A.11) is linear, the superposition principle holds. Next, $\mathbf{\Phi}(t, t_0, \mathbf{x}^p(t_0))$ contains the fundamental solutions and can therefore be used to map any initial perturbation $\Delta\mathbf{x}(t_0)$ at t_0 to the perturbation $\Delta\mathbf{x}(t)$ at time t.

$$\Delta\mathbf{x}(t) = \mathbf{\Phi}(t, t_0, \mathbf{x}^p(t_0))\Delta\mathbf{x}(t_0) \tag{A.14}$$

Using this relation, the *transition property* can be derived (with $t_0 \leq t_1 \leq t_2$).

$$\begin{aligned} \Delta\mathbf{x}(t_1) &= \mathbf{\Phi}(t_1, t_0, \mathbf{x}^p(t_0))\Delta\mathbf{x}(t_0) \\ \Delta\mathbf{x}(t_2) &= \mathbf{\Phi}(t_2, t_1, \mathbf{x}^p(t_1))\Delta\mathbf{x}(t_1) \end{aligned}$$

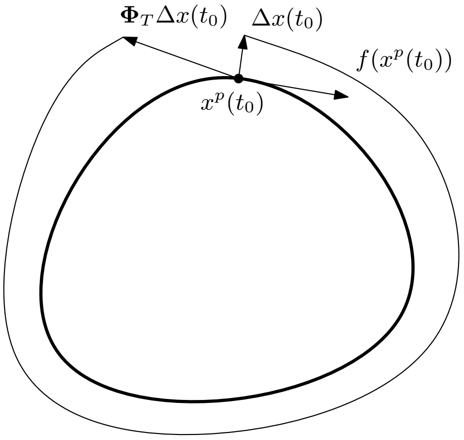

Figure A.1: Periodic solution and monodromy matrix

Now, by substitution of $\Delta \mathbf{x}(t_1)$ in the second equation it follows:

$$\begin{aligned}\Delta \mathbf{x}(t_2) &= \mathbf{\Phi}(t_2, t_1, \mathbf{x}^p(t_1))\mathbf{\Phi}(t_1, t_0, \mathbf{x}^p(t_0))\Delta \mathbf{x}(t_0) \\ &= \mathbf{\Phi}(t_2, t_0, \mathbf{x}^p(t_0))\Delta \mathbf{x}(t_0) \qquad \text{(A.15)}\end{aligned}$$

The transition property can now easily be derived:

$$\mathbf{\Phi}(t_2, t_0, \mathbf{x}^p(t_0)) = \mathbf{\Phi}(t_2, t_1, \mathbf{x}^p(t_1))\mathbf{\Phi}(t_1, t_0, \mathbf{x}^p(t_0)) \qquad \text{(A.16)}$$

For autonomous systems, $\partial \mathbf{f}(t, \mathbf{x})/\partial \mathbf{x}$ is independent of t. Therefore, the fundamental solution matrix can be shifted in time, because it only depends on the time span.

$$\mathbf{\Phi}(t, t_0, \mathbf{x}_0)) = \mathbf{\Phi}(t + \Delta t, t_0 + \Delta t, \mathbf{x}_0) \quad \forall \mathbf{x}_0 \in \mathbb{R}^n,\ \forall \Delta t \qquad \text{(A.17)}$$

The initial condition $\mathbf{x}_0$ is not necessarily on the periodic solution. For non-autonomous systems, a similar condition holds when the fundamental solution is along a periodic orbit $\mathbf{x}^p(t)$ and the time shift is exactly the period time T.

$$\mathbf{\Phi}(t, t_0, \mathbf{x}_0^p) = \mathbf{\Phi}(t + T, t_0 + T, \mathbf{x}_0^p) \qquad \text{(A.18)}$$

A.4 Monodromy matrix & Floquet multipliers

A special fundamental solution matrix is the matrix that maps a perturbation at t_0 to the perturbation at $t_0 + T$, where T is the minimal period time of the periodic solution. This fundamental solution matrix is called the *monodromy matrix*.

$$\mathbf{\Phi}_T = \mathbf{\Phi}(t_0 + T, t_0, \mathbf{x}^p(t_0)) \qquad \text{(A.19)}$$

The effect of the monodromy matrix is shown schematically in figure A.1. For the periodic solutions that are considered here, the monodromy matrix has an important property (for $k = 0, 1, 2, \ldots$):

$$\mathbf{\Phi}(t_0 + T, t_0, \mathbf{x}^p(t_0)) = \mathbf{\Phi}(t_0 + (k+1)T, t_0 + kT, \mathbf{x}^p(t_0 + kT)) \qquad \text{(A.20)}$$

This holds both for autonomous and non-autonomous systems. The monodromy matrix plays an important role in analyzing the fundamental solution matrix for time spans larger than T. For instance:

$$\begin{aligned}&\mathbf{\Phi}(t + 2T, t_0, \mathbf{x}^p(t_0)) = \\ &\mathbf{\Phi}(t + 2T, t_0 + 2T, \mathbf{x}^p(t_0 + 2T))\mathbf{\Phi}(t_0 + 2T, t_0 + T, \mathbf{x}^p(t_0 + T))\mathbf{\Phi}(t_0 + T, t_0, \mathbf{x}^p(t_0)) \qquad \text{(A.21)}\end{aligned}$$

The transition property (A.16) is used here. When using (A.18) and (A.20), this equation simplifies to:

$$\mathbf{\Phi}(t+2T, t_0, \mathbf{x}^p(t_0)) = \mathbf{\Phi}(t, t_0, \mathbf{x}^p(t_0))(\mathbf{\Phi}_T)^2 \tag{A.22}$$

Or, more general:

$$\mathbf{\Phi}(t+kT, t_0, \mathbf{x}^p(t_0)) = \mathbf{\Phi}(t, t_0, \mathbf{x}^p(t_0))(\mathbf{\Phi}_T)^k \quad k = 0, 1, 2, \ldots \tag{A.23}$$

It is clear that the long-term behavior of the fundamental solution matrix is determined by the monodromy matrix. To characterize this long-term behavior, the eigenvalue decomposition of the monodromy matrix is calculated.

$$\mathbf{\Phi}_T = \mathbf{M}\mathbf{\Lambda}\mathbf{M}^{-1} \tag{A.24}$$

The matrix $\mathbf{\Lambda}$ is diagonal and contains the eigenvalues λ_i $(i = 1, 2, \ldots, n)$ of the monodromy matrix, $\mathbf{M}$ contains the corresponding eigencolumns $\mathbf{m}_i$. In general, the eigenvalues λ_i can be complex. Repetitive multiplication of the monodromy matrix gives:

$$(\mathbf{\Phi}_T)^k = \mathbf{M}\mathbf{\Lambda}^k\mathbf{M}^{-1} \tag{A.25}$$

The long-term behavior of the fundamental solution matrix is clearly determined by the eigenvalues of the monodromy matrix. These eigenvalues are called *Floquet multipliers* or *characteristic multipliers.* A Floquet multiplier λ_i gives the growth in direction $\mathbf{m}_i$; if $|\lambda_i| < 1$ a perturbation in direction $\mathbf{m}_i$ decays. On the other hand, a perturbation in direction $\mathbf{m}_i$ grows if $|\lambda_i| > 1$.

The monodromy matrix is dependent on the initial condition (on the periodic orbit) $\mathbf{x}^p(t_0)$. The Floquet multiplier however are independent of this initial condition which can be shown by considering two matrices $\mathbf{C} = \mathbf{AB}$ and $\mathbf{D} = \mathbf{BA}$. The eigenvalues $(\lambda_{\mathbf{C}i})$ and eigenvectors $(\mathbf{u}_{\mathbf{C}i})$ of $\mathbf{C}$ are defined by:

$$\lambda_{\mathbf{C}i}\mathbf{u}_{\mathbf{C}i} = \mathbf{AB}\mathbf{u}_{\mathbf{C}i} \tag{A.26}$$

By premultiplying by $\mathbf{B}$ it can be concluded that $(\lambda_{\mathbf{C}i})$ is also an eigenvalue of $\mathbf{D}$ with eigenvector $u_{\mathbf{D}i} = \mathbf{B}\mathbf{u}_{\mathbf{C}i}$.

$$\lambda_{\mathbf{C}i}\mathbf{B}\mathbf{u}_{\mathbf{C}i} = \mathbf{BAB}\mathbf{u}_{Ci} \tag{A.27}$$

This result can also be applied to monodromy matrices. The monodromy matrices $\mathbf{\Phi}_a = \mathbf{\Phi}(t_a + T, t_a, \mathbf{x}^p(t_a))$ and $\mathbf{\Phi}_b = \mathbf{\Phi}(t_b + T, t_b, \mathbf{x}^p(t_b))$ are considered. Both matrices describe the same periodic solution, but with different initial condition: $\mathbf{x}^p(t_a)) \neq \mathbf{x}^p(t_b))$ and $t_b > t_a$. The matrices can be split using the transition property (A.16).

$$\begin{aligned} \mathbf{\Phi}_a &= \mathbf{\Phi}(t_a + T, t_b, \mathbf{x}^p(t_b))\mathbf{\Phi}(t_b, t_a, \mathbf{x}^p(t_a)) \\ \mathbf{\Phi}_b &= \mathbf{\Phi}(t_b + T, t_a + T, \mathbf{x}^p(t_a + T))\mathbf{\Phi}(t_a + T, t_b, \mathbf{x}^p(t_b)) \end{aligned}$$

Using property (A.18) and the result for eigenvalues in this paragraph, it follows that $\mathbf{\Phi}_a$ and $\mathbf{\Phi}_b$ have the same eigenvalues. Floquet multipliers are therefore independent of the initial condition on a periodic solution.

A.5 Saltation matrix

Discontinuous systems exhibit discontinuities in the fundamental solution matrix and this matrix can therefore not be calculated using (A.13). A solution $\mathbf{x}(t)$ starting in subspace V_- is considered. At time t_p this solution crosses the hyperplane Σ to enter subspace V_+. The hyperplane Σ is the switching boundary that separates subspaces V_- and V_+. For t_p the solution is on this hyperplane:

$$\mathbf{x}(t_p) \in \Sigma \tag{A.28}$$

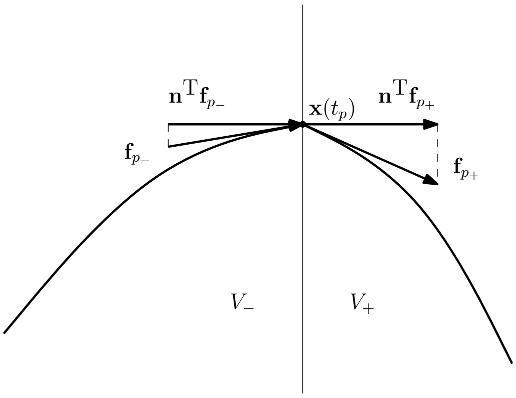

Figure A.2: Projection of derivatives

In order for the solution to cross the boundary, it is assumed that the projections of the vectorfield in both subspaces on the normal $\mathbf{n}$ have the same sign. This condition is shown in figure A.2. Here, $\mathbf{f}_{p_-}$ and $\mathbf{f}_{p_+}$ are the derivatives at the switching boundary in subspace V_- and V_+ respectively.

$$\mathbf{n}^{\mathrm{T}}\mathbf{f}_{p_-}\mathbf{n}^{\mathrm{T}}\mathbf{f}_{p_+} > 0 \tag{A.29}$$

The solution is assumed to start in subspace V_-, so $\mathbf{x}(t_0) = \mathbf{x}_0 \in V_-$. The solution crosses the switching boundary at t_p, so for $t_0 \leq t \leq t_p$ the solution is entirely in subspace V_- and is therefore continuous. For this interval, the fundamental solution matrix can be calculated by integrating (A.13), yielding the fundamental solution matrix just before the jump $\mathbf{\Phi}(t_{p_-}, t_0, \mathbf{x_0})$. This matrix maps an infinitesimal perturbation on the orbit starting at $\mathbf{x}_0$ at t_0 to the corresponding perturbation at t_{p_-}.

$$\mathbf{\Phi}(t_{p_-}, t_0, \mathbf{x_0}) = \lim_{t \uparrow t_p} \mathbf{\Phi}(t, t_0, \mathbf{x_0}) \tag{A.30}$$

The jump can be described by a matrix $\mathbf{S}$, which is called the *saltation matrix* [8]. This matrix maps a perturbation at t_{p_-} just before the jump to the perturbation just after the jump (at t_{p_+}). The saltation matrix can therefore be regarded as a fundamental solution matrix from t_{p_-} to t_{p_+}.

$$\mathbf{S} = \mathbf{\Phi}(t_{p_+}, t_{p_-}, \mathbf{x}(t_{p_-})) \tag{A.31}$$

The transition property (A.16) also holds for the saltation matrix:

$$\mathbf{\Phi}(t_{p_+}, t_0, \mathbf{x_0}) = \mathbf{S}\mathbf{\Phi}(t_{p_-}, t_0, \mathbf{x_0}) \tag{A.32}$$

When the solution is in subspace V_+ for $t_p < t < t_q$, the fundamental solution matrix for this time span can again be calculated using equation (A.13).

$$\mathbf{\Phi}(t_q, t_0, \mathbf{x}_0) = \mathbf{\Phi}(t_q, t_{p_+}, \mathbf{x}(t_{p_+}))\mathbf{S}\mathbf{\Phi}(t_{p_-}, t_0, \mathbf{x_0}) \tag{A.33}$$

When the fundamental solution matrix for $t > t_p$ is known, $\mathbf{\Phi}(t_{p_+}, t_0, \mathbf{x_0})$ can be expressed as:

$$\mathbf{\Phi}(t_{p_+}, t_0, \mathbf{x_0}) = \lim_{t \downarrow t_p} \mathbf{\Phi}(t, t_0, \mathbf{x_0}) \tag{A.34}$$

The function of the saltation matrix is explained in the first part of this section. To obtain this saltation matrix, the nonlinear dynamical system will be inspected in the neighborhood of the switching boundary. This situation is shown in figure A.3.

In figure A.3, the undisturbed ($\mathbf{x}(t)$) and disturbed ($\overline{\mathbf{x}}(t)$) solutions are shown. Because of the perturbation, both solutions do not cross the switching boundary at the same time. The

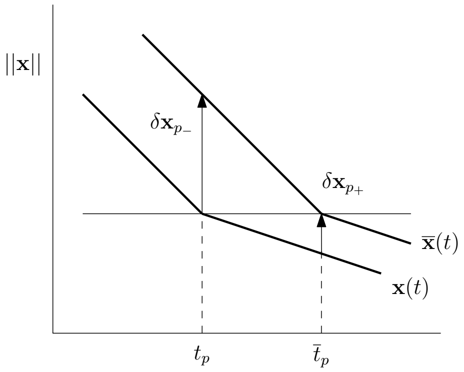

Figure A.3: Disturbed and undisturbed solution

times the undisturbed and disturbed solutions cross are denoted by t_p and $\overline{t}_p$ respectively. The perturbations at both crossing times are given by:

$$\delta\mathbf{x}_{p_-} = \overline{\mathbf{x}}(t_p) - \mathbf{x}(t_p) \tag{A.35}$$

$$\delta\mathbf{x}_{p_+} = \overline{\mathbf{x}}(\overline{t}_p) - \mathbf{x}(\overline{t}_p) \tag{A.36}$$

The solutions at $\overline{t}_p$ can be related to those at t_p by using a first-order Taylor series expansion.

$$\mathbf{x}(\overline{t}_p) \approx \mathbf{x}(t_p) + \mathbf{f}_{p_+}\delta t \tag{A.37}$$

$$\overline{\mathbf{x}}(\overline{t}_p) \approx \mathbf{x}(t_p) + \delta\mathbf{x}_{p_-} + \mathbf{f}_{p_-}\delta t \tag{A.38}$$

In these equations, $\delta t = \overline{t}_p - t_p$ and the following abbreviations are used:

$$\mathbf{f}_{p_+} = \mathbf{f}(t_{p_+}, \mathbf{x}(t_{p_+})) \tag{A.39}$$

$$\mathbf{f}_{p_-} = \mathbf{f}(t_{p_-}, \mathbf{x}(t_{p_-})) \tag{A.40}$$

Inserting (A.37) and (A.38) in (A.36) yields:

$$\begin{aligned} \delta\mathbf{x}_{p_+} &= \overline{\mathbf{x}}(\overline{t}_p) - \mathbf{x}(\overline{t}_p) \\ &\approx \mathbf{x}(t_p) + \delta\mathbf{x}_{p_-} + \mathbf{f}_{p_-}\delta t - (\mathbf{x}(t_p) + \mathbf{f}_{p_+}\delta t) \\ &\approx \delta\mathbf{x}_{p_-} + \mathbf{f}_{p_-}\delta t - \mathbf{f}_{p_+}\delta t \end{aligned} \tag{A.41}$$

The switching boundary is given by the hyperspace Σ, but can also be described by a switching boundary function $h(\mathbf{x})$.

$$h(\mathbf{x}) = 0 \Leftrightarrow \mathbf{x} \in \Sigma \tag{A.42}$$

The disturbed solution crosses the boundary at $\overline{t}_p$. Using a Taylor series approximation of first-order of the switching boundary function yields:

$$\begin{aligned} 0 &= h(\overline{\mathbf{x}}(\overline{t}_p)) \\ &\approx h(\mathbf{x}(t_p) + \delta\mathbf{x}_{p_-} + \mathbf{f}_{p_-}) \\ &\approx h(\mathbf{x}(t_p)) + \mathbf{n}^{\mathrm{T}}(\delta\mathbf{x}_{p_-} + \mathbf{f}_{p_-}) \\ &\approx \mathbf{n}^{\mathrm{T}}(\delta\mathbf{x}_{p_-} + \mathbf{f}_{p_-}) \end{aligned} \tag{A.43}$$

The normal $\mathbf{n}$ is defined as $\mathbf{n}(\mathbf{x}) = \nabla h(\mathbf{x})$ and the property $h(\mathbf{x}(t_p)) = 0$ is used. With this result, the variation δt can be expressed as function of $\delta\mathbf{x}_{p_-}$.

$$\mathbf{n}^{\mathrm{T}}\mathbf{f}_{p_-}\delta t = -\mathbf{n}^{\mathrm{T}}\delta\mathbf{x}_{p_-} \tag{A.44}$$

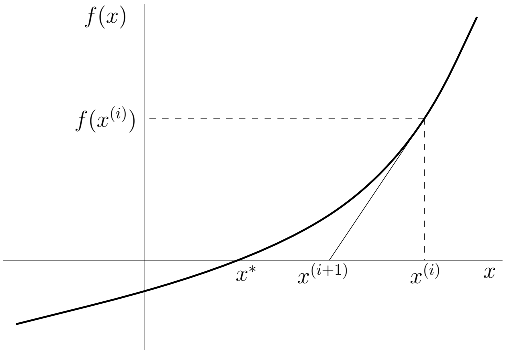

Figure A.4: The Newton-Raphson algorithm

A combination of (A.41) and (A.44) gives the variation $\delta\mathbf{x}_{p_+}$ in terms of $\delta\mathbf{x}_{p_-}$.

$$\delta\mathbf{x}_{p_+} = \delta\mathbf{x}_{p_-} + (\mathbf{f}_{p_+} - \mathbf{f}_{p_-})\frac{\mathbf{n}^{\mathrm{T}}\delta\mathbf{x}_{p_-}}{\mathbf{n}^{\mathrm{T}}\mathbf{f}_{p_-}} \tag{A.45}$$

Since the saltation matrix relates $\delta\mathbf{x}_{p_+}$ to $\delta\mathbf{x}_{p_-}$ as $\delta\mathbf{x}_{p_+} = \mathbf{S}\delta\mathbf{x}_{p_-}$ it can now easily be derived.

$$\mathbf{S} = \mathbf{I} + \frac{(\mathbf{f}_{p_+} - \mathbf{f}_{p_-})\mathbf{n}^{\mathrm{T}}}{\mathbf{n}^{\mathrm{T}}\mathbf{f}_{p_-}} \tag{A.46}$$

The saltation matrices are calculated for both the SDOF and MDOF system and can be found in appendix C.

A.6 Shooting

A.6.1 Newton-Rhapson algorithm

Figure A.4 shows nonlinear scalar function $f(x)$ with a zero point at x^*. To find this zero point, an initial guess $x^{(0)}$ is needed. Using the function value and the local tangent an updated guess can be calculated. This is done by extrapolating the local tangent to the x-axis, as is shown in figure A.4. When $x^{(i)}$ is the result of iteration i, the next iterate $x^{(i+1)}$ can be calculated with:

$$x^{(i+1)} = x^{(i)} - \frac{f(x^{(i)})}{f'(x^{(i)})} \tag{A.47}$$

The Newton-Raphson algorithm does not converge for all functions or might converge to another zero of the function. However, when the initial guess is close to the solution, the procedure is likely to converge. The Newton-Raphson algorithm can also be applied to find a zero of a multi-dimensional function. In every iteration, an update $\Delta\mathbf{x} = \mathbf{x}^{(i+1)} - \mathbf{x}^{(i)}$ can be calculated.

$$\frac{\partial\mathbf{f}(\mathbf{x}^{(i)})}{\partial\mathbf{x}}\Delta\mathbf{x} = -\mathbf{f}(\mathbf{x}^{(i)}) \tag{A.48}$$

A.6.2 Single shooting

The (single) shooting method for non-autonomous systems solves a two-point boundary value problem (BVP) in order to find periodic solutions. The problem can be stated as:

$$\mathbf{H}(\mathbf{x}_0, T) = \varphi_T(t_0, \mathbf{x}_0) - \mathbf{x}_0 = 0 \tag{A.49}$$

Here, T is the period time of the periodic solution and $\mathbf{x}_0$ is a state on the periodic solution. State $\varphi_T(\mathbf{x}_0)$ is the state at time $t_0 + T$, when started on $\mathbf{x}_0$ at $t = t_0$. The period time T of the periodic solution is known at forehand, because the autonomous system is time-periodic. Since only first-order periodic orbits are considered, the period time can be expressed as a function of the excitation frequency ω: $T = 2\pi/\omega$. The zero of $\mathbf{H}(\mathbf{x}_0, T)$ is calculated using the Newton-Raphson algorithm.

$$\frac{\partial \mathbf{H}}{\partial \mathbf{x}_0} \Delta \mathbf{x}_0 = -H(\mathbf{x}_0, T) \tag{A.50}$$

Evaluating the partial derivative gives:

$$(\mathbf{\Phi}_T(t_0, \mathbf{x}_0) - \mathbf{I})\Delta \mathbf{x}_0 = \mathbf{x}_0 - \varphi_T(t_0, \mathbf{x}_0) \tag{A.51}$$

Solving (A.51) gives an updated estimate for the point $\mathbf{x}_0$ on the periodic orbit. This iteration is repeated until some convergence criterion is reached.

$$\mathbf{x}_0^{(i+1)} = \mathbf{x}_0^{(i)} + \Delta \mathbf{x}_0^{(i)} \tag{A.52}$$

Appendix B

System matrices

Both the single degree-of-freedom model and the multiple degree-of-freedom model are written as standard linear equations in the different subspaces. Equation (3.1) is repeated here:

$$\mathbf{x}(t) = \mathbf{A}_v(\mathbf{x}(t) - \Delta\mathbf{x}_v) + \mathbf{B}u(t) \tag{B.1}$$

Here, the matrix $\mathbf{A}_v$ and the vector $\Delta\mathbf{x}_v$ are dependent on the subspace in which the system operates. The subscript v indicates the matrices belonging to subspace V_v. The input matrix $\mathbf{B}$ is constant and does not change with subspace.

B.1 Single degree-of-freedom system

For the SDOF system, the matrices are obtained by evaluating equation (2.9) for the parameter values in the different subspaces. Matrices $\mathbf{A}_1$ and $\Delta\mathbf{x}_1$ give the system description for contact with the left stopper.

$$\mathbf{A}_1 = \begin{bmatrix} 0 & 1 \\ -\frac{k_1}{m} & -\frac{c+c_1}{m} \end{bmatrix}, \quad \Delta\mathbf{x}_1 = \begin{bmatrix} -b \\ 0 \end{bmatrix} \tag{B.2}$$

The system description in the backlash gap is given by $\mathbf{A}_2$ and $\Delta\mathbf{x}_2$. By observation of $\mathbf{A}_2$ it is clear that the dynamics are independent on the displacement coordinate x, which explains the rigid body motion as described in the report.

$$\mathbf{A}_2 = \begin{bmatrix} 0 & 1 \\ 0 & -\frac{c}{m} \end{bmatrix}, \quad \Delta\mathbf{x}_2 = \begin{bmatrix} 0 \\ 0 \end{bmatrix} \tag{B.3}$$

The matrices $\mathbf{A}_3$ and $\Delta\mathbf{x}_3$ are similar to $\mathbf{A}_1$ and $\Delta\mathbf{x}_1$ and describe contact with the right stopper. For the nominal parameters in table 2.1 $\mathbf{A}_1$ and $\mathbf{A}_3$ are equal, only the offset $\Delta\mathbf{x}_3$ differs from $\Delta\mathbf{x}_1$.

$$\mathbf{A}_3 = \begin{bmatrix} 0 & 1 \\ -\frac{k_2}{m} & -\frac{c+c_2}{m} \end{bmatrix}, \quad \Delta\mathbf{x}_3 = \begin{bmatrix} b \\ 0 \end{bmatrix} \tag{B.4}$$

The input matrix is given by:

$$\mathbf{B} = \begin{bmatrix} 0 \\ \frac{1}{m} \end{bmatrix} \tag{B.5}$$

B.2 Multiple degree-of-freedom system

The matrices for the MDOF system are obtained by evaluating equation (2.19). Again, $\mathbf{A}_1$ and $\mathbf{A}_3$ describe the dynamics for contact with the right and left stopper respectively and are equal for the nominal parameters in table 2.2.

$$\mathbf{A}_1 = \begin{bmatrix} 0 & 1 & 0 & 0 & 0 & 0 & 0 & 0 \\ -\frac{k_1+k_2}{m_1} & -\frac{c_1+c_2}{m_1} & \frac{k_2}{m_1} & \frac{c_2}{m_1} & 0 & 0 & 0 & 0 \\ 0 & 0 & 0 & 1 & 0 & 0 & 0 & 0 \\ -\frac{k_2}{m_2} & -\frac{c_2}{m_2} & -\frac{k_2+k_{s1}}{m_2} & -\frac{c_2+c_3+c_{s1}}{m_2} & \frac{k_{s1}}{m_2} & \frac{c_3+c_{s1}}{m_2} & 0 & 0 \\ 0 & 0 & 0 & 0 & 0 & 1 & 0 & 0 \\ 0 & 0 & \frac{k_{s1}}{m_3} & \frac{c_3+c_{s1}}{m_3} & -\frac{k_4+k_{s1}}{m_3} & -\frac{c_3+c_4+c_{s1}}{m_3} & \frac{k_4}{m_3} & \frac{c_4}{m_3} \\ 0 & 0 & 0 & 0 & 0 & 0 & 0 & 1 \\ 0 & 0 & 0 & 0 & \frac{k_4}{m_4} & \frac{c_4}{m_4} & -\frac{k_4}{m_4} & -\frac{c_4}{m_4} \end{bmatrix} \tag{B.6}$$

$$\Delta\mathbf{x}_1 = \begin{bmatrix} 0 & 0 & 0 & 0 & -b & 0 & -b & 0 \end{bmatrix}^{\mathrm{T}} \tag{B.7}$$

$$\mathbf{A}_2 = \begin{bmatrix} 0 & 1 & 0 & 0 & 0 & 0 & 0 & 0 \\ -\frac{k_1+k_2}{m_1} & -\frac{c_1+c_2}{m_1} & \frac{k_2}{m_1} & \frac{c_2}{m_1} & 0 & 0 & 0 & 0 \\ 0 & 0 & 0 & 1 & 0 & 0 & 0 & 0 \\ -\frac{k_2}{m_2} & -\frac{c_2}{m_2} & -\frac{k_2}{m_2} & -\frac{c_2+c_3}{m_2} & 0 & \frac{c_3}{m_2} & 0 & 0 \\ 0 & 0 & 0 & 0 & 0 & 1 & 0 & 0 \\ 0 & 0 & \frac{k_{s1}}{m_3} & \frac{c_3}{m_3} & -\frac{k_4}{m_3} & -\frac{c_3+c_4}{m_3} & \frac{k_4}{m_3} & \frac{c_4}{m_3} \\ 0 & 0 & 0 & 0 & 0 & 0 & 0 & 1 \\ 0 & 0 & 0 & 0 & \frac{k_4}{m_4} & \frac{c_4}{m_4} & -\frac{k_4}{m_4} & -\frac{c_4}{m_4} \end{bmatrix} \tag{B.8}$$

$$\Delta\mathbf{x}_2 = \mathbf{0} \tag{B.9}$$

$$\mathbf{A}_3 = \begin{bmatrix} 0 & 1 & 0 & 0 & 0 & 0 & 0 & 0 \\ -\frac{k_1+k_2}{m_1} & -\frac{c_1+c_2}{m_1} & \frac{k_2}{m_1} & \frac{c_2}{m_1} & 0 & 0 & 0 & 0 \\ 0 & 0 & 0 & 1 & 0 & 0 & 0 & 0 \\ -\frac{k_2}{m_2} & -\frac{c_2}{m_2} & -\frac{k_2+k_{s2}}{m_2} & -\frac{c_2+c_3+c_{s2}}{m_2} & \frac{k_{s2}}{m_2} & \frac{c_3+c_{s2}}{m_2} & 0 & 0 \\ 0 & 0 & 0 & 0 & 0 & 1 & 0 & 0 \\ 0 & 0 & \frac{k_{s2}}{m_3} & \frac{c_3+c_{s2}}{m_3} & -\frac{k_4+k_{s2}}{m_3} & -\frac{c_3+c_4+c_{s2}}{m_3} & \frac{k_4}{m_3} & \frac{c_4}{m_3} \\ 0 & 0 & 0 & 0 & 0 & 0 & 0 & 1 \\ 0 & 0 & 0 & 0 & \frac{k_4}{m_4} & \frac{c_4}{m_4} & -\frac{k_4}{m_4} & -\frac{c_4}{m_4} \end{bmatrix} \tag{B.10}$$

$$\Delta\mathbf{x}_3 = \begin{bmatrix} 0 & 0 & 0 & 0 & b & 0 & b & 0 \end{bmatrix}^{\mathrm{T}} \tag{B.11}$$

The system is excited at mass 1, leading to the constant input matrix:

$$\mathbf{B} = \begin{bmatrix} 0 & \frac{1}{m_1} & 0 & 0 & 0 & 0 & 0 & 0 \end{bmatrix}^{\mathrm{T}} \tag{B.12}$$

Appendix C

Saltation matrices

The saltation matrices are calculated for both the single degree-of-freedom and multiple degree-of-freedom system using the definition in equation (A.46). The saltation matrix $\mathbf{S}_{ij}$ describes the change in a perturbation as it crosses the boundary between subspaces V_i and V_j, where the orbit leaves subspace V_j to enter subspace V_i.

C.1 Single degree-of-freedom system

$$\mathbf{S}_{12} = \begin{bmatrix} 1 & 0 \\ -\frac{c_1}{m} & 1 \end{bmatrix} \tag{C.1}$$

$$\mathbf{S}_{21} = \mathbf{I} \tag{C.2}$$

$$\mathbf{S}_{23} = \mathbf{I} \tag{C.3}$$

$$\mathbf{S}_{32} = \begin{bmatrix} 1 & 0 \\ -\frac{c_2}{m} & 1 \end{bmatrix} \tag{C.4}$$

The saltation matrices show that the fundamental solution matrix only jumps when contact with a stopper is engaged. This is due to the damping force in the stoppers, which gives a discontinuity in the total force on the mass. Since contact with the stoppers is lost when the contact force is zero, leaving a stopper does not result in a jump in the fundamental solution matrix. This also holds for the multiple degree-of-freedom system in the next section.

C.2 Multiple degree-of-freedom system

$$\mathbf{S}_{12} = \begin{bmatrix} 1 & 0 & 0 & 0 & 0 & 0 & 0 & 0 \\ 0 & 1 & 0 & 0 & 0 & 0 & 0 & 0 \\ 0 & 0 & 1 & 0 & 0 & 0 & 0 & 0 \\ 0 & 0 & -\frac{c_{s1}}{m_2} & 1 & \frac{c_{s1}}{m_2} & 0 & 0 & 0 \\ 0 & 0 & 0 & 0 & 1 & 0 & 0 & 0 \\ 0 & 0 & \frac{c_{s1}}{m_3} & 0 & -\frac{c_{s1}}{m_3} & 1 & 0 & 0 \\ 0 & 0 & 0 & 0 & 0 & 0 & 1 & 0 \\ 0 & 0 & 0 & 0 & 0 & 0 & 0 & 1 \end{bmatrix} \tag{C.5}$$

$$\mathbf{S}_{21} = \mathbf{I} \tag{C.6}$$

$$\mathbf{S}_{23} = \mathbf{I} \tag{C.7}$$

$$\mathbf{S}_{32} = \begin{bmatrix} 1 & 0 & 0 & 0 & 0 & 0 & 0 & 0 \\ 0 & 1 & 0 & 0 & 0 & 0 & 0 & 0 \\ 0 & 0 & 1 & 0 & 0 & 0 & 0 & 0 \\ 0 & 0 & -\frac{c_{s2}}{m_2} & 1 & \frac{c_{s2}}{m_2} & 0 & 0 & 0 \\ 0 & 0 & 0 & 0 & 1 & 0 & 0 & 0 \\ 0 & 0 & \frac{c_{s2}}{m_3} & 0 & -\frac{c_{s2}}{m_3} & 1 & 0 & 0 \\ 0 & 0 & 0 & 0 & 0 & 0 & 1 & 0 \\ 0 & 0 & 0 & 0 & 0 & 0 & 0 & 1 \end{bmatrix} \tag{C.8}$$

Appendix D

LMIs for observer design

These are the linear matrix inequalities that have to be solved to obtain a stable observer as is described in chapter 5.

System in subspace 1, observer in subspace 2 ($i = 1$, $j = 2$).

$$\begin{bmatrix} \begin{array}{c}(\mathbf{A}_2 - \mathbf{L}_2\mathbf{C})^{\mathrm{T}}\mathbf{P} \\ +\mathbf{P}(\mathbf{A}_2 - \mathbf{L}_2\mathbf{C}) + \mu_{12}\mathbf{I}\end{array} & \mathbf{P}(\mathbf{A}_1 - \mathbf{A}_2) & \begin{array}{c}\mathbf{P}(\mathbf{a}_1 - \mathbf{a}_2) \\ +0.5(-\lambda_{122}\mathbf{H}_1 + \lambda_{123}\mathbf{H}_2)\end{array} \\ (\mathbf{A}_1 - \mathbf{A}_2)^{\mathrm{T}}\mathbf{P} & -\mu_{12}\varepsilon^2\mathbf{I} & \begin{array}{c}0.5(-\lambda_{121}\mathbf{H}_1 \\ +\lambda_{122}\mathbf{H}_1 - \lambda_{123}\mathbf{H}_2)\end{array} \\ \begin{array}{c}(\mathbf{a}_1 - \mathbf{a}_2)^{\mathrm{T}}\mathbf{P} \\ +0.5(-\lambda_{122}\mathbf{H}_1^{\mathrm{T}} + \lambda_{123}\mathbf{H}_2^{\mathrm{T}})\end{array} & \begin{array}{c}0.5(-\lambda_{121}\mathbf{H}_1^{\mathrm{T}} \\ +\lambda_{122}\mathbf{H}_1^{\mathrm{T}} - \lambda_{123}\mathbf{H}_2^{\mathrm{T}})\end{array} & -\lambda_{121}g_1 + \lambda_{122}g_1 - \lambda_{123}g_2 \end{bmatrix} < 0$$

System in subspace 2, observer in subspace 1 ($i = 2$, $j = 1$).

$$\begin{bmatrix} \begin{array}{c}(\mathbf{A}_1 - \mathbf{L}_1\mathbf{C})^{\mathrm{T}}\mathbf{P} \\ +\mathbf{P}(\mathbf{A}_1 - \mathbf{L}_1\mathbf{C}) + \mu_{21}\mathbf{I}\end{array} & \mathbf{P}(\mathbf{A}_2 - \mathbf{A}_1) & \begin{array}{c}\mathbf{P}(\mathbf{a}_2 - \mathbf{a}_1) \\ +0.5\lambda_{213}\mathbf{H}_1\end{array} \\ (\mathbf{A}_2 - \mathbf{A}_1)^{\mathrm{T}}\mathbf{P} & -\mu_{21}\varepsilon^2\mathbf{I} & \begin{array}{c}0.5(\lambda_{211}\mathbf{H}_1 \\ -\lambda_{212}\mathbf{H}_2 - \lambda_{213}\mathbf{H}_1)\end{array} \\ \begin{array}{c}(\mathbf{a}_2 - \mathbf{a}_1)^{\mathrm{T}}\mathbf{P} \\ +0.5\lambda_{213}\mathbf{H}_1^{\mathrm{T}}\end{array} & \begin{array}{c}0.5(\lambda_{211}\mathbf{H}_1^{\mathrm{T}} \\ -\lambda_{212}\mathbf{H}_2^{\mathrm{T}} - \lambda_{213}\mathbf{H}_1^{\mathrm{T}})\end{array} & \lambda_{211}g_1 - \lambda_{212}g_2 - \lambda_{213}g_1 \end{bmatrix} < 0$$

System in subspace 2, observer in subspace 3 ($i = 2$, $j = 3$).

$$\begin{bmatrix} \begin{array}{c}(\mathbf{A}_3 - \mathbf{L}_3\mathbf{C})^{\mathrm{T}}\mathbf{P} \\ +\mathbf{P}(\mathbf{A}_3 - \mathbf{L}_3\mathbf{C}) + \mu_{23}\mathbf{I}\end{array} & \mathbf{P}(\mathbf{A}_2 - \mathbf{A}_3) & \begin{array}{c}\mathbf{P}(\mathbf{a}_2 - \mathbf{a}_3) \\ -0.5\lambda_{233}\mathbf{H}_1\end{array} \\ (\mathbf{A}_2 - \mathbf{A}_3)^{\mathrm{T}}\mathbf{P} & -\mu_{23}\varepsilon^2\mathbf{I} & \begin{array}{c}0.5(\lambda_{231}\mathbf{H}_1 \\ -\lambda_{232}\mathbf{H}_2 + \lambda_{213}\mathbf{H}_1)\end{array} \\ \begin{array}{c}(\mathbf{a}_2 - \mathbf{a}_3)^{\mathrm{T}}\mathbf{P} \\ -0.5\lambda_{323}\mathbf{H}_1^{\mathrm{T}}\end{array} & \begin{array}{c}0.5(\lambda_{231}\mathbf{H}_1^{\mathrm{T}} \\ -\lambda_{232}\mathbf{H}_2^{\mathrm{T}} + \lambda_{233}\mathbf{H}_1^{\mathrm{T}})\end{array} & \lambda_{231}g_1 - \lambda_{232}g_2 + \lambda_{233}g_2 \end{bmatrix} < 0$$

System in subspace 3, observer in subspace 2 ($i = 3$, $j = 2$).

$$\begin{bmatrix} \begin{array}{c}(\mathbf{A}_2 - \mathbf{L}_2\mathbf{C})^{\mathrm{T}}\mathbf{P} \\ +\mathbf{P}(\mathbf{A}_2 - \mathbf{L}_2\mathbf{C}) + \mu_{32}\mathbf{I}\end{array} & \mathbf{P}(\mathbf{A}_3 - \mathbf{A}_2) & \begin{array}{c}\mathbf{P}(\mathbf{a}_3 - \mathbf{a}_2) \\ +0.5(-\lambda_{322}\mathbf{H}_1 + \lambda_{323}\mathbf{H}_2)\end{array} \\ (\mathbf{A}_3 - \mathbf{A}_2)^{\mathrm{T}}\mathbf{P} & -\mu_{32}\varepsilon^2\mathbf{I} & \begin{array}{c}0.5(\lambda_{321}\mathbf{H}_2 \\ +\lambda_{322}\mathbf{H}_1 - \lambda_{323}\mathbf{H}_2)\end{array} \\ \begin{array}{c}(\mathbf{a}_3 - \mathbf{a}_2)^{\mathrm{T}}\mathbf{P} \\ +0.5(-\lambda_{322}\mathbf{H}_1^{\mathrm{T}} + \lambda_{323}\mathbf{H}_2^{\mathrm{T}})\end{array} & \begin{array}{c}0.5(\lambda_{321}\mathbf{H}_2^{\mathrm{T}} \\ +\lambda_{322}\mathbf{H}_1^{\mathrm{T}} - \lambda_{323}\mathbf{H}_2^{\mathrm{T}})\end{array} & \lambda_{321}g_2 + \lambda_{322}g_1 - \lambda_{323}g_2 \end{bmatrix} < 0$$

System in subspace 1, observer in subspace 3 ($i = 1$, $j = 3$).

$$\begin{bmatrix} \begin{array}{c} (\mathbf{A}_3 - \mathbf{L}_3\mathbf{C})^{\mathrm{T}}\mathbf{P} \\ +\mathbf{P}(\mathbf{A}_3 - \mathbf{L}_3\mathbf{C}) + \mu_{13}\mathbf{I} \end{array} & \mathbf{P}(\mathbf{A}_1 - \mathbf{A}_3) & \mathbf{P}(\mathbf{a}_1 - \mathbf{a}_3) - 0.5\lambda_{132}\mathbf{H}_2 \\ (\mathbf{A}_1 - \mathbf{A}_3)^{\mathrm{T}}\mathbf{P} & -\mu_{13}\varepsilon^2\mathbf{I} & 0.5(-\lambda_{131}\mathbf{H}_1 + \lambda_{132}\mathbf{H}_2) \\ (\mathbf{a}_1 - \mathbf{a}_3)^{\mathrm{T}}\mathbf{P} - 0.5\lambda_{132}\mathbf{H}_2^{\mathrm{T}} & 0.5(-\lambda_{131}\mathbf{H}_1^{\mathrm{T}} + \lambda_{132}\mathbf{H}_2^{\mathrm{T}}) & -\lambda_{131}g_1 + \lambda_{132}g_2 \end{bmatrix} < 0$$

System in subspace 3, observer in subspace 1 ($i = 3$, $j = 1$).

$$\begin{bmatrix} \begin{array}{c} (\mathbf{A}_1 - \mathbf{L}_1\mathbf{C})^{\mathrm{T}}\mathbf{P} \\ +\mathbf{P}(\mathbf{A}_1 - \mathbf{L}_1\mathbf{C}) + \mu_{31}\mathbf{I} \end{array} & \mathbf{P}(\mathbf{A}_3 - \mathbf{A}_1) & \mathbf{P}(\mathbf{a}_3 - \mathbf{a}_1) + 0.5\lambda_{132}\mathbf{H}_1 \\ (\mathbf{A}_3 - \mathbf{A}_1)^{\mathrm{T}}\mathbf{P} & -\mu_{31}\varepsilon^2\mathbf{I} & 0.5(\lambda_{131}\mathbf{H}_2 - \lambda_{132}\mathbf{H}_1) \\ (\mathbf{a}_3 - \mathbf{a}_1)^{\mathrm{T}}\mathbf{P} + 0.5\lambda_{132}\mathbf{H}_1^{\mathrm{T}} & 0.5(\lambda_{131}\mathbf{H}_2^{\mathrm{T}} - \lambda_{132}\mathbf{H}_1^{\mathrm{T}}) & \lambda_{131}g_2 + \lambda_{132}g_1 \end{bmatrix} < 0$$

Appendix E

The $\mathcal{S}$-procedure

Consider the quadratic forms $\mathbf{W}(\mathbf{x}) = \mathbf{x}^{\mathrm{T}}\mathbf{Q}\mathbf{x}$ and $\mathbf{G}_i(\mathbf{x}) = \mathbf{x}^{\mathrm{T}}\mathbf{R}_i\mathbf{x}$, $i = 1, \ldots, k$.

Suppose condition E.1 has to be satisfied:

$$\mathbf{W}(\mathbf{x}) < 0 \quad \text{if } G_1(\mathbf{x}) \leq 0,\, G_2(\mathbf{x}) \leq 0, \ldots,\, G_k(\mathbf{x}) \leq 0,\, \mathbf{x} \neq \mathbf{0} \tag{E.1}$$

Let

$$\mathbf{S}(\mathbf{x}) = \sum_{i=1}^{k} \lambda_i \mathbf{G}_i(\mathbf{x}), \quad \lambda_i \geq 0$$

If the λ_i's can be found such that condition (E.2) holds, then condition (E.2) implies condition (E.1).

$$W(\mathbf{x}) - S(\mathbf{x}) < 0 \quad \text{if } \mathbf{x} \neq \mathbf{0} \tag{E.2}$$

Changing problem (E.1) into (E.2) is called the *$\mathcal{S}$-procedure.* In general, the $\mathcal{S}$-procedure is conservative. For $k = 1$ however, conditions (E.1) and (E.2) are equivalent and the $\mathcal{S}$-procedure is called *lossless.*

Appendix F

Observer gains

Observer gains for $\varepsilon = 0.65$:

$$\mathbf{L}_1 = \begin{bmatrix} -0.0003 \\ -0.0167 \\ -0.2984 \\ -3.7764 \\ 0.2984 \\ 3.7764 \\ 0.0003 \\ 0.0168 \end{bmatrix} \cdot 10^5, \quad \mathbf{L}_2 = \begin{bmatrix} -0.0003 \\ -0.0168 \\ -0.2988 \\ -3.8255 \\ 0.2988 \\ 3.8255 \\ 0.0003 \\ 0.0168 \end{bmatrix} \cdot 10^5, \quad \mathbf{L}_3 = \begin{bmatrix} -0.0003 \\ -0.0167 \\ -0.2975 \\ -3.8045 \\ 0.2975 \\ 3.8045 \\ 0.0003 \\ 0.0168 \end{bmatrix} \cdot 10^5$$

Observer gains for $\varepsilon = 9.5$:

$$\mathbf{L}_1 = \begin{bmatrix} -0.0267 \\ -0.3268 \\ -2.2433 \\ -1.6906 \\ 2.2331 \\ 1.6965 \\ 0.0746 \\ 0.3049 \end{bmatrix} \cdot 10^6, \quad \mathbf{L}_2 = \begin{bmatrix} -0.0277 \\ -0.3358 \\ -2.2998 \\ -1.7170 \\ 2.2893 \\ 1.7232 \\ 0.0772 \\ 0.3129 \end{bmatrix} \cdot 10^6, \quad \mathbf{L}_3 = \begin{bmatrix} -0.0274 \\ -0.3335 \\ -2.2869 \\ -1.6847 \\ 2.2765 \\ 1.6908 \\ 0.0764 \\ 0.3110 \end{bmatrix} \cdot 10^6$$

Appendix G

ASME paper

Proceedings of IDETC/CIE 2007
ASME 2007 International Design Engineering Technical Conferences &
Computers and Information in Engineering Conference
September 4-7, 2007, Las Vegas, USA

IDETC2007-DRAFT

CLASSIFICATION OF PERIODIC SOLUTIONS IN A SINGLE DEGREE-OF-FREEDOM SYSTEM WITH BACKLASH

Bart Besselink[1], **Amit Shukla**[2*], **Rob Fey**[1] **and Henk Nijmeijer**[1]

1) Department of Mechanical Engineering
Eindhoven University of Technology
P.O. Box 513, 5600 MB Eindhoven
The Netherlands

2) Department of Mechanical and Manufacturing Engineering
School of Engineering and Applied Science
Miami University
Oxford, Ohio, 45056

ABSTRACT

In this paper a single degree-of-freedom system with backlash is studied for its periodic response. This system is modeled as a piecewise linear system with discontinuity in the net restoring force, caused by additional damping in the contact-zone. The periodic orbits are classified by their number of subspace boundary crossings and Floquet multipliers. For this classification, the known analytical solutions in the different subspaces are used in the multiple shooting algorithm and a continuation method. Some observations are also presented about the qualitative features (such as symmetry, rigid body solutions) exhibited by this class of systems.

1 INTRODUCTION

Clearance, dead zone or backlash is a common feature of many mechanical systems and can undermine the performance of the system. Backlash can be due to intended clearance necessary for assembly and operation. It can further be a result of operational wear and tear. The specific instances of appearance of backlash and its influence on the dynamics and control of systems includes power transmissions, robotics, measurement systems, manufacturing processes and structures. Backlash can lead to rattle and chaotic motion in gears in power trains which can lead to damage and noisy operation. Systems with backlash characteristics form a subclass of discontinuous mechanical systems. Backlash can be modeled as a discontinuity of the net restoring force (neglecting impact) with piecewise linear characteristics. Several researchers have investigated the effect of backlash on the dynamics which includes evaluation of bifurcations and chaos in gear systems subject to harmonic excitation [1], analysis of subharmonic resonances of an offshore structure as a bilinear oscillator model via simulation [2], evaluation of the rattling in torsional gear train models using harmonic balance methods [3], response analysis for such systems with parametric excitation [4], experimental and computational investigation of the global stability of the periodic response of single degree-of-freedom models with elastic stops [5], periodically forced piecewise linear oscillator [6], strongly nonlinear behavior of the oscillator in clearance [7], dynamics of the bi-linear oscillator [8] and oscillator with motion-limiting constraints [9].

In this paper a single degree-of-freedom system with backlash (neglecting impact) is analyzed for the effect of excitation parameters on the dynamics of the periodic response using the multiple shooting method [10]. Specifically, this paper presents new insights on the qualitative dynamics for a system which has infinite stiffness ratio between the stopper stiffness and the stiffness in the backlash region. This results in a classification of periodic orbits by their number of subspace boundary crossings and Floquet multipliers. A piecewise-linear stiffness and damping model is used which leads to a discontinuous jump in the net restoring force.

This paper is organized as follows: first, a model will be presented, which is followed by the analytical approach for computing the response (flow) and its integration into the multiple shooting method. Using this some results about the classification of the periodic orbits by their number of subspace boundary

---

[*] Address all correspondence to this author

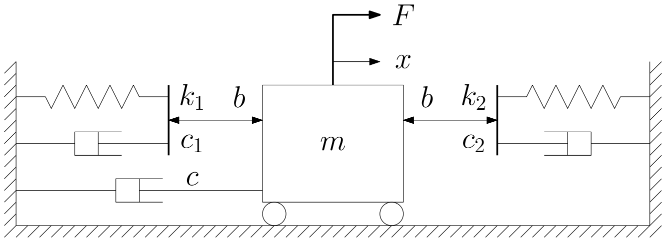

Figure 1: SYSTEM WITH BACKLASH

crossings will be presented. Finally, conclusions and recommendations will be given.

2 MODELING OF SYSTEM DYNAMICS

The single degree-of-freedom system with backlash is presented schematically in Fig. 1 and consists of a mass which can move freely between two stoppers. The dynamics of the stoppers is assumed to be fast enough to ensure that they return to their original position between successive contacts and are therefore at rest when a contact occurs. This assumption is only valid when the damping force is small in comparison to the spring force. This is verified for the system under consideration, so the dynamics of the stoppers do not have to be modeled and the equation of motion is given as:

$$m\ddot{x} + C(\mathbf{x}) + K(\mathbf{x}) = F \tag{1}$$

Here, m is the mass of the system, F denotes the external forcing and $\mathbf{x} = [x,\ \dot{x}]^{\mathrm{T}}$ is the state vector. The restoring force $K(\mathbf{x})$ and the damping force $C(\mathbf{x})$ are given by:

$$K(\mathbf{x}) = \begin{cases} 0 & ,\mathbf{x} \in V \\ k_1(x+b) & ,\mathbf{x} \in V_1 \\ k_2(x-b) & ,\mathbf{x} \in V_2 \end{cases} \tag{2}$$

$$C(\mathbf{x}) = \begin{cases} c\dot{x} & ,\mathbf{x} \in V \\ (c+c_1)\dot{x} & ,\mathbf{x} \in V_1 \\ (c+c_2)\dot{x} & ,\mathbf{x} \in V_2 \end{cases} \tag{3}$$

The state space is divided into three subspaces V, V_1 and V_2 as is depicted in Fig. 2, based on contact or no-contact with the stoppers. As can be seen in Fig. 2, each boundary consists of two parts. When the mass moves towards a stopper ($x\dot{x} > 0$) it will hit it when $|x| = b$, which explains the vertical parts of the boundary. However, the mass does not loose contact to the stopper when $|x| = b$ again, but when the contact force becomes zero. Therefore the slope of the non-vertical parts are prescribed by the ratio of the spring and damper constant of the stopper.

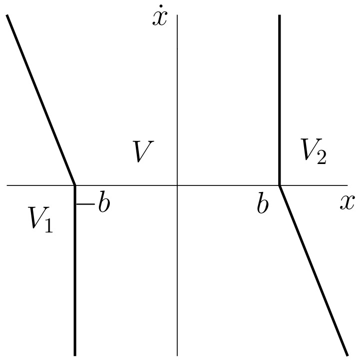

Figure 2: SUBSPACES IN PHASE PLANE OF THE SYSTEM WITH BACKLASH

This can mathematically be described as:

$$V_1 = \left\{ \mathbf{x} \in \mathbb{R}^2 \,|\, x < -b \wedge k_1(x+b) + c_1\dot{x} \leq 0 \right\} \tag{4}$$

$$V_2 = \left\{ \mathbf{x} \in \mathbb{R}^2 \,|\, x > b \wedge k_2(x-b) + c_2\dot{x} \geq 0 \right\} \tag{5}$$

These equations give the conditions for contact with a stopper. If the mass is in contact with the left stopper the state is in subspace V_1 whereas V_2 denotes contact with the right stopper.

When the mass is not in contact with a stopper the state is in subspace V:

$$V = \left\{ \mathbf{x} \in \mathbb{R}^2 \,|\, \mathbf{x} \notin (V_1 \cup V_2) \right\} \tag{6}$$

In the backlash region no restoring force acts on the mass, only some damping force is present. The steady state forced response or periodic orbits of these systems is of interest as it dictates the long term dynamics and possible loss of stability for rotating machines such as geared systems. Often such systems operate at constant frequency where the forcing is given by:

$$F = A\sin(\omega t) \tag{7}$$

Using this forcing, the total equation can be written in first-order form as:

$$\dot{\mathbf{x}} = \mathbf{f}(t,\mathbf{x}) = \begin{bmatrix} \dot{x} \\ -\frac{1}{m}\left(K(\mathbf{x}) + C(\mathbf{x})\right) + \frac{1}{m}A\sin(\omega t) \end{bmatrix} \tag{8}$$

The nominal parameters are chosen to be $m = 1$ kg, $c = 0.05$ Ns/m, $b = 1$ m, $k_1 = k_2 = 4$ N/m, $c_1 = c_2 = 0.5$ Ns/m and $A = 1$ N.

3 ANALYSIS METHODOLOGY

3.1 Periodic orbits and stability - a review

In this work, periodic orbits and their stability are analyzed for different forcing parameters (frequency and amplitude). The flow of the nonautonomous system after a time lapse t_d starting at t_0 is denoted by $\varphi_{t_d}(t_0, \mathbf{x}_0) \equiv \varphi(t_0 + t_d, t_0, \mathbf{x}_0)$. A periodic solution, $\varphi^p(t, t_0, \mathbf{x}_0)$, where $T > 0$ is the minimal period time, is defined as follows:

$$\varphi^p(t + T, t_0, \mathbf{x}_0) = \varphi^p(t, t_0, \mathbf{x}_0)\ \forall t \tag{9}$$

In this paper, only period-one periodic orbits are considered, so $T = 2\pi/\omega$. The stability of a periodic orbit can be determined by considering the evolution in time of small perturbations on that orbit. The *fundamental solution matrix* $\Phi_{\Delta t}$ [11] describes how a perturbation $\Delta\mathbf{x}(t_0)$ is mapped to the perturbation $\Delta\mathbf{x}(t_0 + \Delta t)$:

$$\Delta\mathbf{x}(t_0 + \Delta t) = \Phi_{\Delta t}(t_0, \mathbf{x}(t_0))\Delta\mathbf{x}(t_0) \tag{10}$$

The *monodromy matrix* Φ_T [11] is the fundamental solution matrix for $\Delta t = T$ along a periodic orbit. For smooth systems, the stability of this periodic orbit can then be determined by calculating the eigenvalues of the monodromy matrix, which are called *Floquet multipliers*.

Since system (1) is discontinuous, the monodromy matrix is discontinuous as well and exhibits jumps whenever the state changes subspace. This effect of this jump on the perturbation can be described by a *saltation matrix* $\mathbf{S}$ [11]:

$$\mathbf{S} = \mathbf{I} + \frac{(\mathbf{f}_{p_+} - \mathbf{f}_{p_-})\mathbf{n}^{\mathrm{T}}}{\mathbf{n}^{\mathrm{T}}\mathbf{f}_{p_-}} \tag{11}$$

In this equation, $\mathbf{f}_{p_-}$ is the direction of the vectorfield along the solution just before the subspace boundary crossing, $\mathbf{f}_{p_+}$ is the similar direction just after the crossing. The normal of the subspace boundary, at which the flow crosses, is denoted by $\mathbf{n}$.

3.2 Simulation

The solution of the forced system can be obtained by integrating Eqn. (8). However, to get an accurate solution near a subspace boundary the solution tolerance must be low, causing a long simulation time. This simulation time can be reduced by utilizing an analytical solution as discussed next. Since the system model is piecewise-linear, an analytical solution can be calculated in each subspace. The standard description of a linear system is considered:

$$\dot{\mathbf{x}} = \mathbf{A}_v\mathbf{x} + \mathbf{B}u(t) \tag{12}$$

Here, $\mathbf{A}_v$ is the system matrix in subspace v, $\mathbf{B}$ is the input matrix and $u(t)$ the input. For ease of notation, the subscript v indicating the subspace will be omitted from now onwards. Using the spectral decomposition $\mathbf{A} = \mathbf{M}\Lambda\mathbf{M}^{-1}$ and generalized coordinates $\mathbf{p} = \mathbf{M}^{-1}\mathbf{x}$, the solution for $\mathbf{p}$ is given by:

$$\mathbf{p} = e^{\Lambda t}\mathbf{p}_0 + \int_0^t e^{\Lambda(t-\tau)}\mathbf{M}^{-1}\mathbf{B}u(\tau)d\tau \tag{13}$$

Simplifying notation (with $\hat{\mathbf{B}} = \mathbf{M}^{-1}\mathbf{B}$) yields:

$$\mathbf{p} = e^{\Lambda t}\left(\mathbf{p}_0 + \mathbf{d}\right), \quad \mathbf{d} = \int_0^t e^{-\Lambda\tau}\hat{\mathbf{B}}u(\tau)d\tau \tag{14}$$

It is assumed that the eigenvalues are distinct, so $e^{\Lambda(t-\tau)}$ is diagonal, which yields n decoupled equations. If the complex notation for the input $u(\tau) = A\sin(\omega\tau + \phi)$ is used, the k-th entry in $\mathbf{d}$ ($\mathbf{d}_k$) is given as:

$$\mathbf{d}_k = \frac{A\hat{\mathbf{B}}_k}{2i}\int_0^t \left(e^{-(\lambda_k - i\omega)\tau}e^{i\phi} - e^{-(\lambda_k + i\omega)\tau}e^{-i\phi}\right)d\tau \tag{15}$$

Here, $\hat{\mathbf{B}}_k$ is the k-th entry in the vector $\hat{\mathbf{B}}$, λ_k is the k-th eigenvalue. The solution of (15) is:

$$\mathbf{d}_k = \frac{A\hat{\mathbf{B}}_k}{2i}\left(-\frac{(e^{-(\lambda_k - i\omega)t} - 1)e^{i\phi}}{\lambda_k - i\omega} + \frac{(e^{-(\lambda_k + i\omega)t} - 1)e^{-i\phi}}{\lambda_k + i\omega}\right) \tag{16}$$

The solution for $\mathbf{x}$ can then be obtained by $\mathbf{x} = \mathbf{M}\mathbf{p}$. The algorithm calculating the solution of the piecewise-linear system, of which the flowchart is given in Fig. 3, starts by creating a time vector t. Next, the subspace in which the initial condition x_0 is located is determined using Eqns. (4) to (6). Using this subspace v_0, the corresponding system matrices are selected and the solution for the entire time vector is calculated, without changing the matrices. For this data, the subspaces v_k at each t_k are calculated. When all v_k are equal, the solution does not leave the initial subspace and the total solution is found.

In general, solutions will exist on all three subspaces and hence not all v_k will be equal. In those cases, if v_{l+1} is the first point that differs from v_0, the change of subspace is known to occur between corresponding locations in the time vector, t_l and t_{l+1}. The switching time t_s can then be found at any arbitrary accuracy by calculating additional states and corresponding subspaces for $t_l < t < t_{l+1}$.

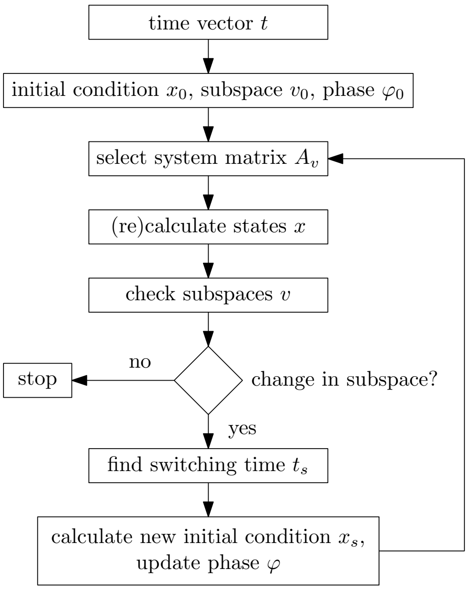

Figure 3: FLOWCHART OF THE SIMULATION ALGORITHM

When the switching time t_s is found, the new solution for $v_k, k = l+1, l+2, \ldots$ can be calculated using the new system matrices and x_s as initial condition. The phase angle of the forcing is adapted to ensure a smooth forcing function. This procedure is repeated until the correct states are calculated for all times in the time vector t.

It should to be noticed that the time step, $\delta t = t_{k+1} - t_k$, has to be chosen small enough to ensure that subspaces are not crossed without calculating any data point in it. When this happens, the change in subspace will not be noticed, resulting in an incorrect solution. Since an analytical solution can be calculated for a large number of points instantaneously, choosing a sufficiently small δt does not lead to an excessive increase in calculation time.

An advantage of this method is that it calculates the subspace boundary crossing times for a periodic orbit. This information can be used to analytically calculate the overall fundamental solution matrix $\Phi_{\Delta t}$ by multiplication of individual fundamental solution matrices in the different subspaces and the appropriate saltation matrices $\mathbf{S}$ to describe the subspace boundary crossing. This reduces the computation time for the multiple shooting algorithm, which is presented next.

3.3 Multiple shooting

To estimate periodic orbits, the multiple shooting method is used. This method is preferred to the single shooting method because it uses a number of initial points along the periodic solution instead of only one as shown in Fig. 4. The multiple shooting method is therefore more robust. The N shooting points are equally spaced in time with constant time step $h = T/N$, so $t_k = t_0 + kh$, and are stored in the vector $\mathbf{X} = [\mathbf{x}_1, \ldots \mathbf{x}_k, \ldots \mathbf{x}_N]^{\mathrm{T}}$. The segment connecting point $\mathbf{x}_{k-1}$ to the next point $\mathbf{x}_k$ is given by:

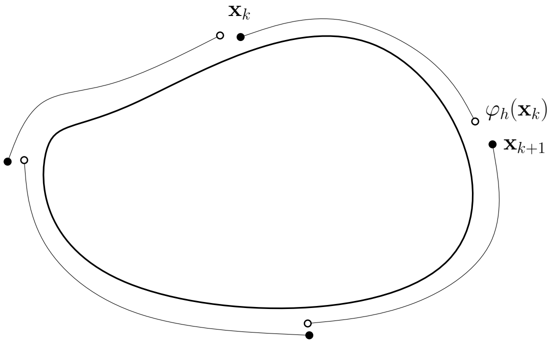

Figure 4: THE MULTIPLE SHOOTING METHOD

$$\mathbf{x}_k = \varphi_h(t_{k-1}, \mathbf{x}_{k-1}) \tag{17}$$

Here, $\varphi_h(t_{k-1}, \mathbf{x}_{k-1})$ denotes the solution of $\dot{\mathbf{x}}(t) = \mathbf{f}(t, \mathbf{x}(t))$ at time t_k starting at initial condition $\mathbf{x}_{k-1}$ (at t_{k-1}). This solution is evaluated using the analytical procedure described above. It can be seen in Fig. 4 that a periodic solution is found if all segments connect, so when Eqn. (17) holds for $k = 2, \ldots, N$ and $\mathbf{x}_1 = \varphi_h(t_N, \mathbf{x}_N)$. Therefore, a zero of the following function has to be calculated:

$$\mathbf{H}(\mathbf{X}) = \begin{bmatrix} -\mathbf{x}_1 + \varphi_h(t_N, \mathbf{x}_N) \\ \vdots \\ -\mathbf{x}_k + \varphi_h(t_{k-1}, \mathbf{x}_{k-1}) \\ \vdots \\ -\mathbf{x}_N + \varphi_h(t_{N-1}, \mathbf{x}_{N-1}) \end{bmatrix} \tag{18}$$

The Newton-Raphson algorithm is used iteratively to obtain an updated estimate of the periodic solution:

$$\frac{\partial \mathbf{H}}{\partial \mathbf{X}} \Delta \mathbf{X} = -\mathbf{H}(\mathbf{X}) \tag{19}$$

Here, the Jacobian is given as:

$$\frac{\partial \mathbf{H}}{\partial \mathbf{X}} = \begin{bmatrix} -I & 0 \ \ldots & 0 & \Phi_h(t_N, \mathbf{x}_N) \\ \Phi_h(t_1, \mathbf{x}_1) & -I \ \ldots & 0 & 0 \\ \vdots & \vdots & \vdots & \vdots \\ 0 & 0 \ \ldots & \Phi_h(t_{N-1}, \mathbf{x}_{N-1}) & -I \end{bmatrix} \tag{20}$$

Here, $\Phi_h(t_k, \mathbf{x}_k)$ denotes the fundamental solution matrix at time $t_k + h$ for a solution with initial condition x_k at t_k. When the set of equations (19) is solved, the next iterate can be calculated by $\mathbf{X}^{(i+1)} = \mathbf{X}^{(i)} + \Delta\mathbf{X}^{(i)}$.

When the multiple shooting method is applied to the system with backlash in Fig. 1 (and described by Eqn. (8)), a problem arises for periodic solutions that are entirely in the backlash gap (and do not hit the stoppers). Because of the absence of stiffness in this region, a small perturbation in the position $\delta x(t_0)$ of the mass will neither grow or decay. The entire periodic orbit will just be shifted in position. The velocity will not be affected. This knowledge gives some insight in the monodromy matrix for this situation. Therefore, the perturbation $\Delta\mathbf{x}(t_a) = [\delta x(t_a)\ 0]^{\mathrm{T}}$ is considered. The monodromy matrix maps this perturbation $\Delta\mathbf{x}(t_a)$ to $\Delta\mathbf{x}(t_a + T)$, which is equal to the initial perturbation.

$$\begin{bmatrix} \delta x(t_a+T) \\ 0 \end{bmatrix} = \Phi_T \begin{bmatrix} \delta x(t_a) \\ 0 \end{bmatrix} \tag{21}$$

By inspecting this equation, it can be seen that the first column of the monodromy matrix is $e_1 = [1\ 0]^{\mathrm{T}}$. This holds for all t_a. As an example, this column is substituted into Eqn. (20) for a multiple shooting algorithm using three points ($N = 3$). Then, columns 1, 3 and 5 of $\partial\mathbf{H}/\partial\mathbf{X}$ are respectively:

$$\begin{bmatrix} -1\ 0\ 1\ 0\ 0\ 0 \end{bmatrix}^{\mathrm{T}}, \quad \begin{bmatrix} 0\ 0\ -1\ 0\ 1\ 0 \end{bmatrix}^{\mathrm{T}}, \quad \begin{bmatrix} 1\ 0\ 0\ 0\ 1\ 0 \end{bmatrix}^{\mathrm{T}} \tag{22}$$

It is clear that these columns are not linearly independent, so $\partial\mathbf{H}/\partial\mathbf{X}$ will not have full rank and Eqn. (19) can not be solved. This is a result of the rigid body motion possible in the backlash region. Thus, a rigid body constraint can be added to make the above matrix, $\partial\mathbf{H}/\partial\mathbf{X}$, full rank. For $N = 3$, this equation is:

$$\begin{bmatrix} 1\ 0\ 1\ 0\ 1\ 0 \end{bmatrix} \Delta\mathbf{X}^{(i)} = -\left(\mathbf{X}_1^{(i)} + \mathbf{X}_3^{(i)} + \mathbf{X}_5^{(i)}\right)/3 \tag{23}$$

Here, $\mathbf{X}_1$ denotes the first entry in the vector $\mathbf{X}$, which is the position coordinate of the first shooting point. Similarly, $\mathbf{X}_3$ and $\mathbf{X}_5$ denote the position coordinates of the other shooting points. This equation basically ensures that the periodic solution is (roughly) located in the center between the two stoppers and does not influence the periodic solution itself. By adding this rigid body constraint, the total number of equations is one larger than the number of variables and thus a least squares solution can be calculated.

Since this extra equation is not needed when the periodic solution comes in contact with the stoppers, it is only used when the condition number of $\partial\mathbf{H}/\partial\mathbf{X}$ is very high.

Table 1: FLOQUET MULTIPLIERS FOR THE LABELED PERIODIC ORBITS IN FIG. 5

Label	Floquet multipliers	
A	1.0000	0.7990
B	1.4210	0.1482
C	0.6086	0.3085
D	-0.2249 - 0.2261i	-0.2249 + 0.2261i
E	-0.0986 - 0.0120i	-0.0986 + 0.0120i
F	0.0001	0.0

4 RESULTS

The dynamics of the system (Fig. 1) as described by Eqn. (8) is characterized by the response diagram in Fig. 5. This figure shows the amplitude of the periodic solution for a range of forcing frequencies ω for nominal excitation amplitude, $A = 1$ N. Stable branches are indicated by solid lines, while unstable branches are shown by dashed lines. The amplitude of the periodic solution (*amp*) is defined as half the difference between the maximum and minimum position during one period. The branches are calculated using the multiple shooting algorithm as described in this paper in combination with continuation. It is clear that multiple solutions exist near the primary peak. The bending to the right of the primary peak in Fig. 5 is characteristic for a hardening oscillator.

4.1 Periodic response

Next, some periodic orbits on the response curve in Fig. 5 are highlighted to discuss the characteristics of periodic orbits exhibited by this system. For frequencies $\omega > 1$ rad/s, for some initial conditions, the mass can move in the region between the stoppers without hitting them. Examples of such an orbit are given in Fig. 7. Since the subspace boundaries are not crossed by these periodic solutions, the dynamics are purely linear. In this subspace, no restoring force is present. The periodic orbit is therefore not unique; it can be shifted in position. This however does not affect the nature of the periodic solution and the amplitude will not change by shifting the solution. Because of the absence of a restoring force, one Floquet multiplier is equal to one, as is shown in Tab. 1. The Floquet multipliers are not affected by a shift of the periodic solution in the backlash region.

The distance between the stoppers is $2b$, so this linear solution will exist for amplitudes up to one, which is around $\omega = 1$ rad/s. However, in the frequency range of (1, 1.42) rad/s, the backlash system has multiple solutions for the same excitation frequency, of which orbits A, B and C are an example. For $\omega = 1.4$ rad/s, the solution at C is shown in Fig. 8. In this case

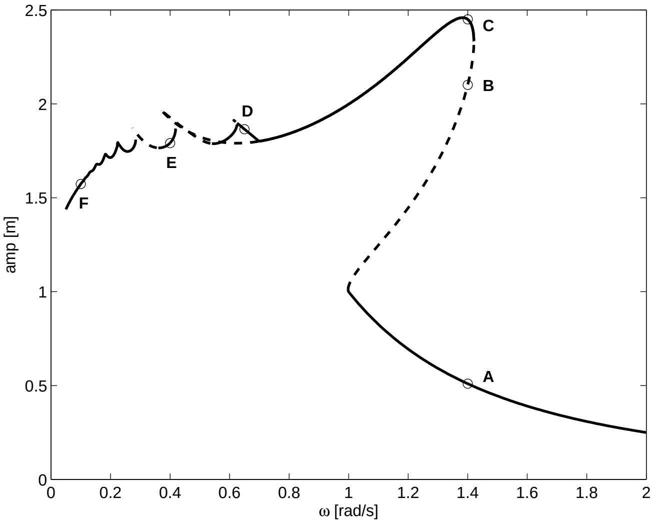

Figure 5: RESPONSE DIAGRAM OF SYSTEM (1) FOR $A = 1$

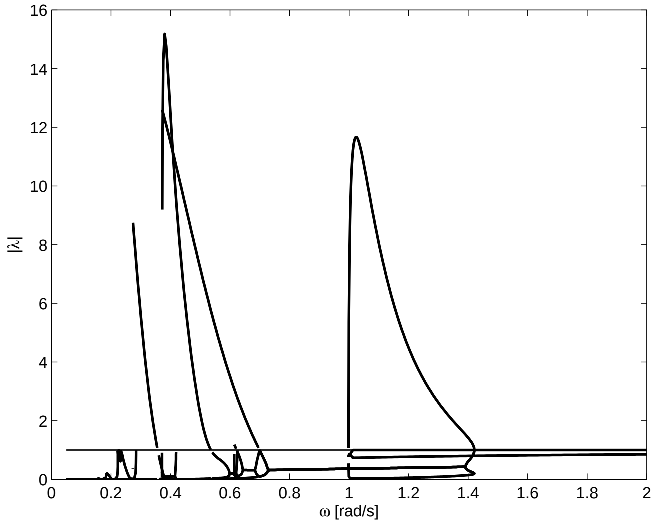

Figure 6: FLOQUET MULTIPLIERS FOR THE PERIODIC ORBITS IN FIG. 5

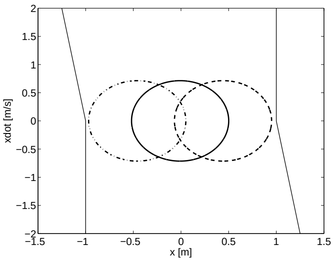

Figure 7: PERIODIC ORBITS AT POINT A IN FIG. 5 ($\omega = 1.4$ rad/s)

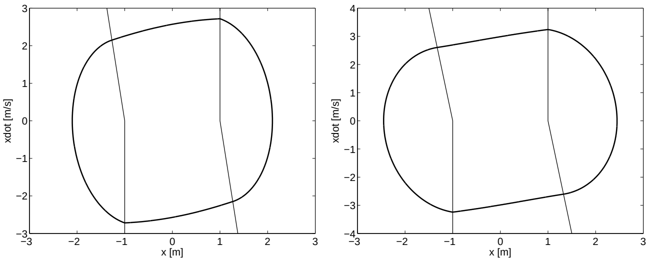

Figure 8: PERIODIC ORBITS AT POINTS B (LEFT) AND C (RIGHT) IN FIG. 5 ($\omega = 1.4$ rad/s)

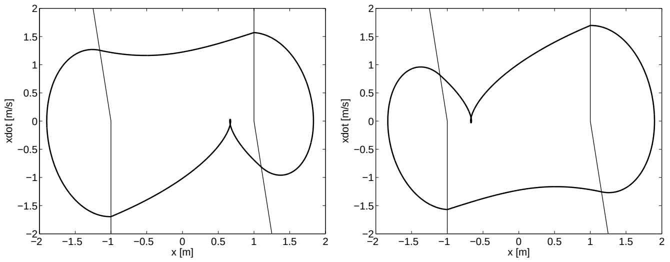

Figure 9: PERIODIC ORBITS AT POINT D IN FIG. 5 ($\omega = 0.65$ rad/s)

the stoppers are engaged and the solution visits all subspaces. The two stable branches containing A and C are connected by an unstable branch. Orbit B in Fig. 8 is an example of an unstable periodic orbit on this branch. This unstable orbit also visits all subspaces.

When the top branch is tracked for decreasing excitation frequency, it loses stability at $\omega = 0.7$ rad/s. However, a branch of asymmetrical periodic orbits originates at the same point. The asymmetrical periodic orbit at point D is depicted in Fig. 9. Since $\mathbf{f}(t,\mathbf{x}) = -\mathbf{f}(t,-\mathbf{x})$, at point D a version of the orbit mirrored in the origin can also be found.

For decreasing excitation frequency, the number of boundary crossings increases and hence can be used to classify the periodic orbits. Figure 10 shows examples of multiple boundary crossings. Each time the number of boundary crossings changes a *corner collision* bifurcation [12] takes place. In corner collision bifurcations the periodic solution just touches the subspace boundary at the discontinuity in the boundary prior to crossing the boundary for some change in parameter. In this system this is exhibited in the parameter space of excitation amplitude and frequency. It should be noted that the response diagram may be incomplete for this low-frequency region, but the focus of this paper is on the main branch.

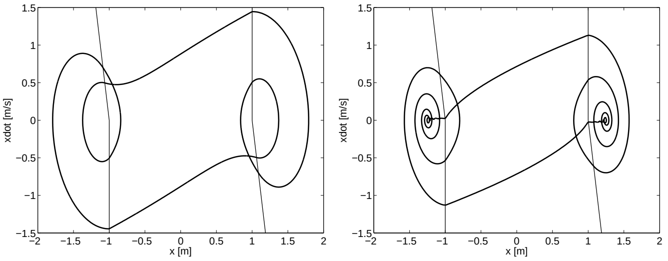

Figure 10: PERIODIC ORBITS AT POINTS E (LEFT, $\omega = 0.4$ rad/s) AND F (RIGHT, $\omega = 0.1$ rad/s) IN FIG. 5

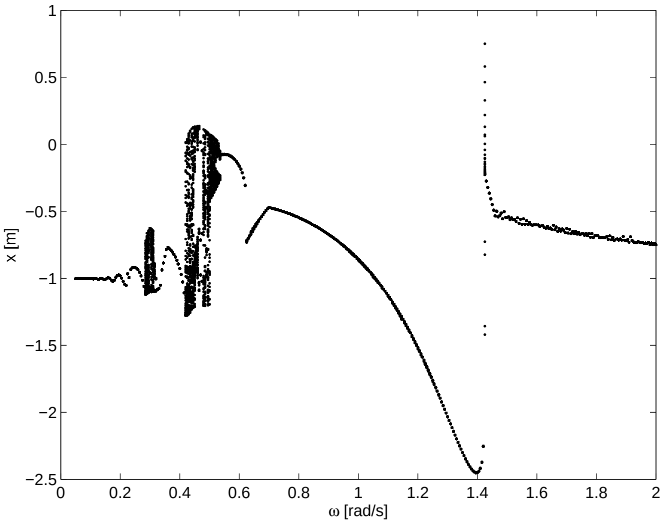

Figure 11: BIFURCATION DIAGRAM OF SYSTEM 1 FOR $A = 1$ N

Figure 6 shows the magnitude of the Floquet multipliers corresponding to the response diagram in Fig. 5. The branch where the response amplitude is smaller than one shows a Floquet multiplier equal to one, which is caused by the absence of a restoring force. At the point where this branch crosses the boundary to become an unstable orbit a *discontinuous fold bifurcation* [13] occurs. Characteristic for this bifurcation is the jump of Floquet multipliers through the unit circle as can be observed in Fig. 6 near $\omega = 1$ rad/s. The point near $\omega = 0.7$ rad/s where the stable symmetrical branch splits into an unstable symmetrical and stable asymmetrical branch can be clearly recognized. It has to be noted that for a range of frequencies between 0.42 and 0.54 rad/s no stable period one solutions exist. This can also be concluded from Fig. 11, which shows a bifurcation diagram for a forcing amplitude $A = 1$ N. This figure suggests chaotic or quasi-periodic behavior in this frequency range.

4.2 Boundary Classification

The dynamics of the system can be characterized by counting the number of boundary crossings of a periodic orbit. A boundary crossing is counted every time the periodic solution changes subspace. This is done for different forcing frequencies and amplitudes, yielding Figs. 12 and 15. The periodic solutions are found by using the multiple shooting algorithm. For Fig. 12, the initial condition for the simulation is calculated using the linear system description in subspace V to ensure that the solution stays in the center between the stoppers when possible. This will result in solutions on the lower branch of Fig. 5. On the contrary, the initial condition (for the simulation) for Fig. 15 is chosen to be in a region where there is contact with a stopper, therefore increasing the probability of finding the solutions on the top branch of Fig. 5.

Based on the linear equations in subspace V, the dashed line, (see Figs. 12 and 15), where the amplitude of the periodic response is equal to one can be calculated analytically. In this case the periodic solution just touches (but does not cross) the boundary. This is referred to as a *corner collision boundary* [12].

The basic trend in Fig. 12 is that the number of crossings increases for decreasing frequency. For low frequencies, the direction of the force stays the same for a longer time span. Here, the dynamics of the system in contact with the stoppers is faster than the change in external forcing direction. The graph also shows that the numerically calculated boundary, that indicates the conditions where the mass first hits the stoppers, matches the analytically calculated boundary very well. The small discrepancy is likely to be caused by the simulated solution not to be exactly in the center between the stoppers.

The non-periodic region, with excitation frequencies between 0.42 and 0.54 rad/s for $A = 1$ N, that was shown in Fig. 11 can also be observed in Fig. 12. No stable solutions exist in this region labeled d in the figure.

For all periodic orbits that are classified by their number of boundary crossings the Floquet multipliers are calculated. The Floquet multiplier with the maximum absolute value is depicted in Figs. 13 and 16. Black and white denote an absolute value of zero and one respectively. All (unstable) Floquet multipliers with an absolute value higher than one are set to one for clarity. This figure also clearly shows the boundaries. This can be explained by considering the monodromy matrices. Each time a switching boundary, in the phase plane, is crossed the monodromy matrix exhibits a discontinuity or jump. This jump (which is described by a saltation matrix) also affects the Floquet multipliers, so a change in number of boundary crossings will also cause a sudden change in Floquet multipliers.

This number of boundary crossing is not the only qualitative difference in the periodic solutions. Fig. 13, when compared to Fig. 12 shows an extra boundary between labels A and B. This suggests a change in the characteristics of the periodic orbit,

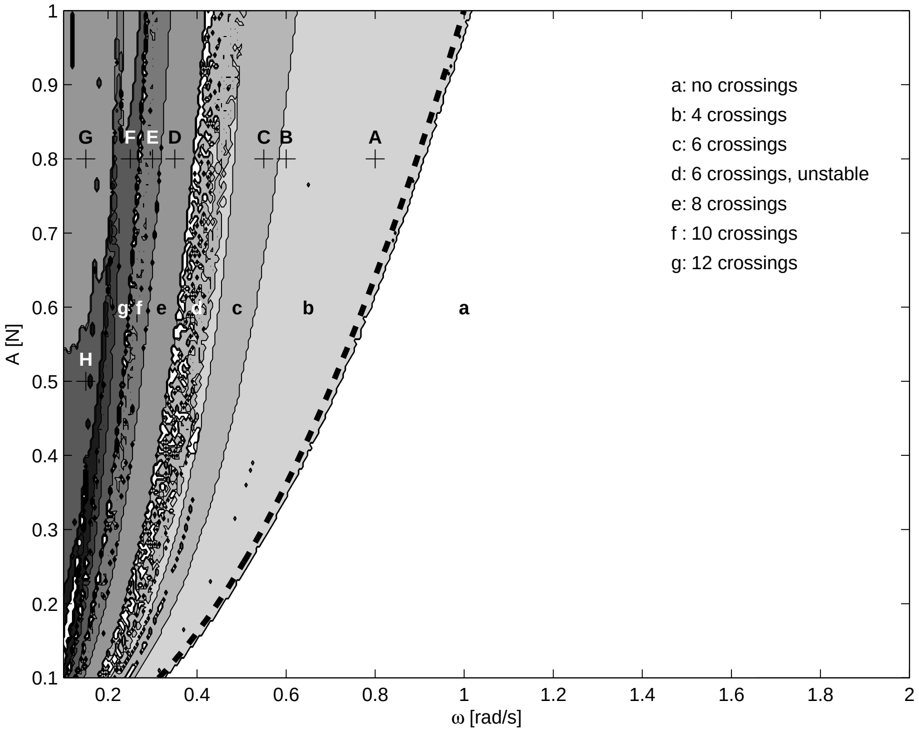

Figure 12: CLASSIFICATION OF PERIODIC ORBITS IN $(A,\,\omega)$ SPACE: BOUNDARY CROSSINGS

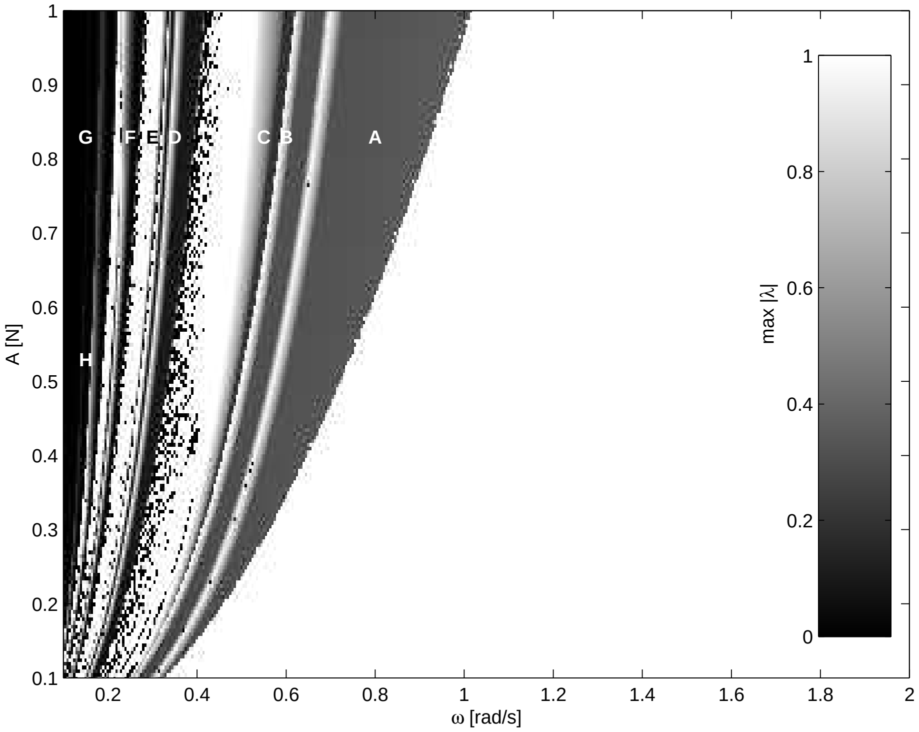

Figure 13: CLASSIFICATION OF PERIODIC ORBITS IN $(A,\,\omega)$ SPACE: FLOQUET MULTIPLIER WITH LARGEST MODULUS

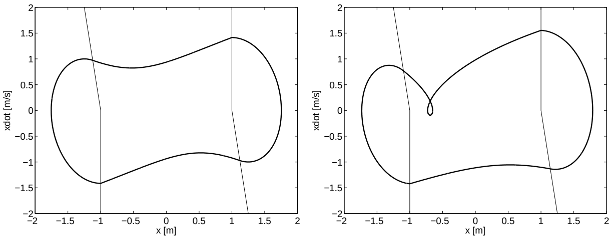

(a) Orbit A at $\omega = 0.8$ rad/s (b) Orbit B at $\omega = 0.6$ rad/s

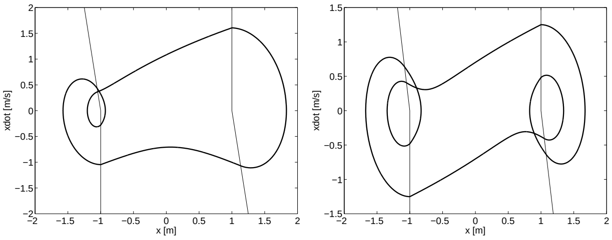

(c) Orbit C at $\omega = 0.55$ rad/s (d) Orbit D at $\omega = 0.35$ rad/s

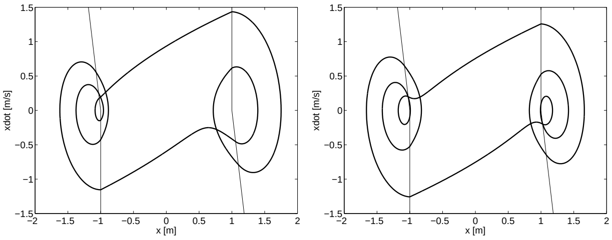

(e) Orbit E at $\omega = 0.3$ rad/s (f) Orbit F at $\omega = 0.25$ rad/s

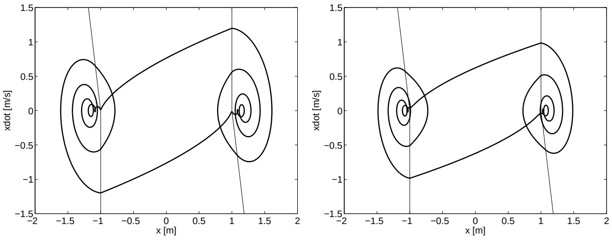

(g) Orbit G at $A = 0.8$ N (h) Orbit H at $A = 0.5$ N

Figure 14: PERIODIC ORBITS AT THE LABELS IN FIG. 12

although the number of crossings does not change. This idea is verified in Fig. 14 (a) to (c), which shows the periodic orbits at labels A, B and C. The periodic orbit changes via a symmetry breaking bifurcation from being symmetric at A to asymmetric at B, without a change in number of boundary crossings. Both the symmetric and asymmetric periodic orbits were already shown in Figs. 8 and 9, when the response diagram was discussed. The asymmetrical periodic orbit at point C does show extra boundary crossings. This change can be noticed in both Fig. 12 and 13.

Figure 14 (d) to (f) show the periodic orbits at points D, E and F, which show an increase in the number of crossings as the forcing frequency decreases. The periodic orbit at point E is again asymmetric. This could also have been concluded from the number of crossings. The number of boundary crossings for this periodic orbit is ten, which means the stoppers are hit five times in a period. Since five is odd, the periodic orbit has to be asymmetrical. It has to be noticed that a number of boundary crossings which is a multiple of four does not mean that the periodic orbit is symmetrical, as can be observed by considering the periodic orbit at point B in Fig. 14 (b).

For low excitation frequency ($\omega < 0.2$ rad/s), the amplitude of the forcing appears to have a larger influence on the number of crossings than the frequency. Figure 14 (g) and (h) shows this influence for $\omega = 0.15$ rad/s. The periodic orbit at G shows higher harmonics that are entirely in subspace V_1 or V_2, so contact with a stopper is not lost. For a lower forcing amplitude, the force is too small to maintain this and contact with the stopper will be lost, causing an increase in the number of boundary crossings. Periodic orbit H in Fig. 14 (h) is an example.

Since Figs. 12 and 13 are created using initial conditions to force the periodic orbit to be in the center between the stoppers when possible, a part of the top branch which overlaps the linear branch of the response diagram (Fig. 5) is not found. Figures 12 and 13 are therefore recreated using a different initial condition ($\mathbf{x}_0 = [3\ 0]^\mathrm{T}$) to enforce the possibility of finding periodic orbits on that part of the top branch of the response diagram. The result is depicted in Figs. 15 and 16, where the latter again shows the maximum absolute value of the Floquet multipliers.

The analytically calculated corner collision boundary does not depend on the initial conditions. Further, the solutions and their characteristics in Figs. 15 and 16 are almost identical to Figs. 12 and 13 when the response exhibits more than four boundary crossings. The diagrams are different at the right side of the corner collision boundary. The region where the periodic solutions cross the boundaries four times is increased. A fractal-like boundary can be seen where this region ends. At the right side of that boundary two situations occur: first, there are periodic orbits in V that do not cross any boundary, as was observed earlier and second, periodic orbits with two boundary crossings are found. This means that only one stopper is touched; Fig. 16 indicates that these periodic orbits are stable. Depending on the initial condition of the multiple shooting algorithm, either this solution or the non-touching solution is found.

5 CONCLUSIONS AND FUTURE WORK

In this paper, preliminary results are presented on the classification of the periodic orbits associated with a single degree-of-freedom system with backlash. The periodic orbits are evaluated using a simulation based method that uses the analytical solution in the different subspaces. Since it also calculates boundary crossing times, the monodromy matrix can be analytically calculated as well. For this, fundamental solution and saltation

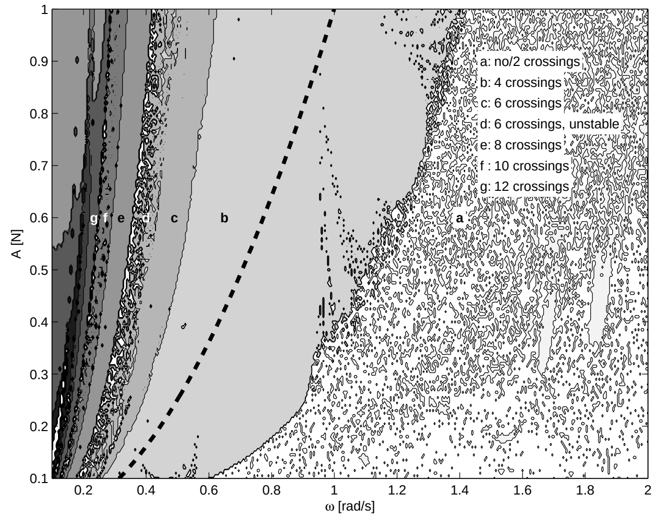

Figure 15: CLASSIFICATION OF PERIODIC ORBITS IN A, ω SPACE: BOUNDARY CROSSINGS - $x_0 = [3\ 0]^T$

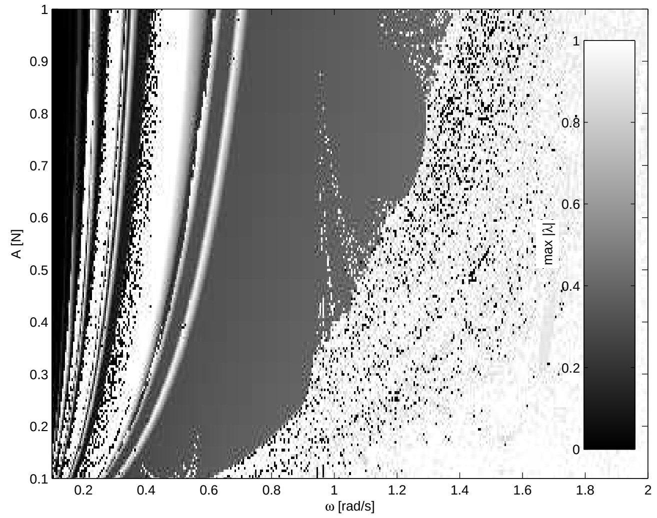

Figure 16: CLASSIFICATION OF PERIODIC ORBITS IN A, ω SPACE: FLOQUET MULTIPLIER WITH LARGEST MODULUS - $x_0 = [3\ 0]^T$

matrices are used. This is then integrated into the multiple shooting method. It is shown that the Floquet multipliers undergo a sudden change when the number of crossings of a periodic orbit changes. Floquet multipliers thus give the same classification as the number of subspace boundary crossings. Next, Floquet multipliers give some additional information on symmetry. Specifically, the parameter space of excitation frequency and amplitude is classified via the boundary collision bifurcations and symmetry breaking bifurcations.

This classification of periodic orbits will be extended for a more realistic, multiple degree-of-freedom system model with backlash as part of the future work related to this research.

REFERENCES

[1] Litak, G., and Friswell, M. I., 2003. "Vibration in gear systems". *Chaos, Solitons and Fractals,* **16**, pp. 795–800.

[2] Thompson, J. M. T., 1983. "Complex dynamics of compliant off-shore structures". *Proceedings of the Royal Society of London. Series A, Mathematical and Physical Sciences,* **387**(1793), pp. 407–427.

[3] Kim, T. C., Rook, T. E., and Singh, R., 2005. "Super- and sub-harmonic response calculations for a torsional system with clearance non-linearity using harmonic balance method". *Journal of Sound and Vibration,* **281**(2–3), pp. 965–993.

[4] Blankenship, G. W., and Kahraman, A., 1995. "Steady state forced response of a mechanical oscillator with combined parametric excitation and clearance type non-linearity". *Journal of Sound and Vibration,* **185**(5), pp. 743–765.

[5] van de Vorst, E. L. B., van Campen, D. H., Fey, R. H. B., and de Kraker, A., 1996. "Determination of global stability of steady-state solutions of a beam system with discontinuous support using manifolds". *Chaos, Solitons and Fractals,* **7**(1), pp. 61–75.

[6] Shaw, S. W., and Holmes, P. J., 1983. "A periodically forced piecewise linear oscillator". *Journal of Sound and Vibration,* **90**(1), pp. 129–155.

[7] Fidlin, A., 2005. "On the strongly nonlinear behavior of an oscillator in a clearance". In Proceedings of ENOC, pp. 389–397.

[8] Natsiavas, S., 1990. "On the dynamics of oscillators with bi-linear damping and stiffness". *International Journal of Non-Linear Mechanics,* **25**(5), pp. 535–554.

[9] Natsiavas, S., 1990. "Stability and bifurcation analysis for oscillators with motion limiting constraints". *Journal of Sound and Vibration,* **141**(1), pp. 97–102.

[10] Guckenheimer, J., 2002. *Numerical analysis of dynamical systems, Handbook of Dynamical Systems*, Vol. 2. Elsevier.

[11] Leine, R. I., and Nijmeijer, H., 2004. *Dynamics and bifurcations of non-smooth mechanical systems*, Vol. 18 of *Lecture Notes in Applied and Computational Mechanics*. Springer.

[12] di Bernardo, M., Budd, C. J., and Champneys, A. R., 2001. "Grazing and border-collision in piecewise-smooth systems: a unified analytical framework". *Physical Review Letters,* **86**(12).

[13] Leine, R. I., and van Campen, D. H., 2002. "Discontinuous bifurcation of periodic solutions". *Mathematical and computer modelling,* **36**, pp. 259–273.